Proceedings of the

9th International Symposium on Vibrations of Continuous Systems

Courmayeur, Italy
21-26 July 2013

Preface

The International Symposium on Vibrations of Continuous Systems is a forum for leading researchers from across the globe to meet with their colleagues and present both old and new ideas in the field. Each participant has been encouraged to either present results of recent research or to reflect on some aspect of the vibration of continuous systems which is particularly interesting, unexpected or unusual. This type of presentation is meant to encourage participants to draw on understanding obtained through many years of research in the field.

The 9th ISVCS takes place 22-26 July 2013 in Hotel Villa Novecento, in Courmayeur, Italy on the Italian side of Mont Blanc (Monte Bianco), the highest mountain in the Alps. It focuses on the vibrations of the fundamental structural elements such as strings, rods, beams, membranes, plates, shells and other solid bodies. Structures composed of assemblies of structural elements are also of interest, if such structures display interesting or unusual response. Typical days at the Symposium will consist of morning technical presentations, with afternoon hikes or excursions, and in the evening further technical discussions. The various outings and social gatherings provide important opportunities for relaxed and informal discussion of technical topics surrounded by the natural beauty of the European Alps.

This volume of Proceedings contains 27 short summaries of the presentations to be made at the Symposium as well as short biographical sketches of the participants.

General Chairman
Yoshihiro Narita

Editorial Chairman
David Kennedy

Registration Chairman
Mark Ewing

Local Chairman
Erasmo Carrera

Honorary Chairman
Arthur Leissa

Past Symposia

The First International Symposium:
The Stanley Hotel, Estes Park, Colorado, USA
August 11-15, 1997

The Second International Symposium:
The Sunstar Hotel, Grindelwald, Switzerland
July 12-16, 1999

The Third International Symposium:
Jackson Lake Lodge, Grand Teton National Park, Wyoming, USA
July 23-27, 2001

The Fourth International Symposium:
Keswick, Lake District, England
July 7-11, 2003

The Fifth International Symposium:
Berchtesgaden at Lake Königssee, Germany
July 25-29, 2005

The Sixth International Symposium:
PlumpJack Squaw Valley Inn, Olympic Valley California
July 23-27, 2007

The Seventh International Symposium:
Zakopane, Poland
July 20-24, 2009

The Eighth International Symposium:
Whistler, British Columbia, Canada
July 18-22, 2011

Table of Contents

Free Vibrations of Beams accounting for Refined Theories and Radial Basis Functions

E. Carrera[1]*, A. J. M. Ferreira[2], A. Pagani[1], M. Petrolo[1]

[1]Department of Mechanical and Aerospace Engineering, Politecnico di Torino,
Corso Duca degli Abruzzi 24, 10129 Torino, Italy.

[2] Department of Mechanical Engineering, Universidade do Porto,
Rua Dr Roberto Frias 4200-465, Porto, Portugal.

The free vibration response analysis of beams with arbitrary cross-sections and geometrical boundary conditions consists of one of the most classical problem of dynamics of continuum systems. Depending on the beam length as well as on the geometrical characteristics of the cross-section, classical beam theories neglecting (Euler-Bernoulli) and accounting (Timoshenko) for transverse shear deformation can lead to inaccurate results, especially in those cases in which vibration modes involving significant cross-section deformations are of interest. The use of refined theories, which are able to accurately detect in-plane deformations and warping, is therefore mandatory in many practical problems related to the high-frequency response analysis and thin-walled beams. In this work, one-dimensional refined theories are developed on the basis of the Unified Formulation (UF), which was recently introduced by the authors [1].

Closed-form exact solutions of governing equations related to free vibration analysis are available only for a few cases of boundary conditions. Therefore, to obtain the solutions for a wide range of problems, adequate approximated/numerical methods have to be developed, see [2]. Numerical methods can be classified as meshless and mesh-based methods. Among the latter, the finite element method (FEM) is probably the most popular. FEM, as well as any other method introducing a finite discretization of the problem domain, reveals by definition deficiencies in the evaluation of the high-frequency response, which plays a fundamental role in many practical problems such as wave propagation and vibro-acoustics. The use of meshless methods is mandatory in these cases. Among the many available meshless methods, the radial basis functions (RBF) method is considered in this work to investigate the free vibration characteristics of beams by accounting for refined theories developed on the basis of UF. In the recent past, authors applied RBF and UF to plate and shell problems and encouraging results were obtained [3]. A few details on the technique adopted are outlined below.

Beam governing equations based on UF. Within the framework of the UF, the displacement field of a *N-order* beam theory can be expressed as

$$\mathbf{u}(x,y,z;t) = F_\tau(x,z)\mathbf{u}_\tau(y;t), \qquad \tau = 1,2,....,M \tag{1}$$

where $\mathbf{u}$ is the displacement vector, xyz is a rectangular coordinate system with y lying along the beam axis, and F_τ are the functions of the coordinates x and z on the cross-section plane of the beam, which is denoted as Ω. $\mathbf{u}_\tau$ is the vector of the *generalized* displacements, M stands for the number of terms used in the expansion, and the repeated subscript, τ,

*Corresponding author: erasmo.carrera@polito.it

indicates summation. The principle of virtual displacements is used to derive the equations of motion.

$$\delta L_{\rm int} + \delta L_{\rm ine} = 0, \qquad \text{with } \delta L_{\rm int} = \int_V \delta\boldsymbol{\epsilon}^T \boldsymbol{\sigma}\, {\rm d}V \tag{2}$$

where L_{int} stands for the strain energy and δL_{ine} is the work done by the inertial loadings. δ stands for the usual virtual variation operator and V is the volume of the beam. $\boldsymbol{\epsilon}$ and $\boldsymbol{\sigma}$ are the strain and stress vectors respectively. The virtual variation of the strain energy is rewritten using strain - displacement relations, constitutive laws, and Eq. (1). After integrations by part, Eq. (2) becomes

$$\delta L_{\rm int} = \int_L \delta\mathbf{u}_\tau^T \mathbf{K}^{\tau s} \mathbf{u}_s \, {\rm d}y + \Big[\delta\mathbf{u}_\tau^T \mathbf{\Pi}^{\tau s} \mathbf{u}_s\Big]_{y=0}^{y=L} \tag{3}$$

where $\mathbf{K}^{\tau s}$ is the differential linear stiffness matrix and $\mathbf{\Pi}^{\tau s}$ is the matrix of the natural boundary conditions in the form of 3×3 fundamental nuclei. The virtual variation of the inertial work is given by $\delta L_{\rm ine} = \int_V \delta\mathbf{u}\rho\ddot{\mathbf{u}}\, {\rm d}V$. The explicit form of the governing equations was obtained in a recent work [4]. In the following, the component along the x-axis of the equations of motion of the refined beam in free vibration is reported

$$\begin{aligned}
\delta u_{x\tau}: \quad & -E^{66}_{\tau s} u_{xs,yy} + \big(E^{26}_{\tau,x s} - E^{26}_{\tau s,x}\big) u_{xs,y} + \big(E^{22}_{\tau,x s,x} + E^{44}_{\tau,z s,z}\big) u_{xs} \\
& -E^{36}_{\tau s} u_{ys,yy} + \big(E^{23}_{\tau,x s} - E^{66}_{\tau s,x}\big) u_{ys,y} + \big(E^{26}_{\tau,x s,x} + E^{45}_{\tau,z s,z}\big) u_{ys} \\
& +\big(E^{45}_{\tau,z s} - E^{16}_{\tau s,z}\big) u_{zs,y} + \big(E^{44}_{\tau,z s,x} + E^{12}_{\tau,x s,z}\big) u_{zs} = -E^{\rho}_{\tau s} \ddot{u}_{xs}
\end{aligned} \tag{4}$$

where the generic term $E^{\alpha\beta}_{\tau,\theta s,\zeta} = \int_\Omega \tilde{C}_{\alpha\beta} F_{\tau,\theta} F_{s,\zeta}\, {\rm d}\Omega$ is a cross-sectional moment parameter. Double over dots stand as second derivative with respect to time (t). Letting $\mathbf{P}_\tau = \left\{ \begin{array}{ccc} P_{x\tau} & P_{y\tau} & P_{z\tau} \end{array} \right\}^T$ to be the vector of the generalized forces, the component along the x-axis of natural boundary conditions is

$$\delta u_{x\tau}: \quad P_{xs} = E^{66}_{\tau s} u_{xs,y} + E^{26}_{\tau s,x} u_{xs} + E^{36}_{\tau s} u_{ys,y} + E^{66}_{\tau s,x} u_{ys} + E^{16}_{\tau s,z} u_{zs} \tag{5}$$

The complete form of governing equations and natural boundary conditions, as well as the components of the fundamental nuclei can be found in [4].

Radial basis functions for one-dimensional refined theories. The solution is assumed to be harmonic, $\mathbf{u}_\tau(y;t) = \mathbf{U}_\tau(y) e^{i\omega t}$. The radial basis function (ϕ) approximation of the generalised displacement field can be defined as

$$\mathbf{U}_\tau(y) = \sum_{i=1}^{N_c} \alpha_i \phi(\|y - y_i\|_2), \qquad 0 \le y \le L \tag{6}$$

where y_i, $i = 1, ..., N_c$ is a finite set of distinct points (centers) on the beam axis whose length is referred to as L. The coefficients α_i are chosen so that $\mathbf{u}_\tau$ satisfies some variationally-consistent boundary conditions. Some examples of RBFs are given below

$$\begin{array}{ll}
\phi(r) = r^3, & cubic \\
\phi(r) = e^{-cr^2}, & Gaussian \\
\phi(r) = \sqrt{c^2 + r^2}, & multiquadrics
\end{array} \tag{7}$$

By substituting Eq. (6) into the governing equations and by appliying the boundary conditions at the collocations points that lie at the beam ends, the following eigenproblem can be formulated

$$[\mathcal{L} - \omega^2 \mathcal{G}]\, \mathbf{X} = \mathbf{0} \tag{8}$$

with $\mathcal{L}$ collecting stiffness terms and $\mathcal{G}$ collecting inertial terms. In Eq. (8), $\mathbf{X}$ are the modal shapes associated with the natural frequencies which are referred to as ω.

Preliminary results Several results concerning free vibration analysis of beam-like structures, obtained through the combination of UF and FEM, are available in the literature. Among those examples, the free vibration characteristics of a thin-walled cylinder are described in this section. As shown in [1], lower-order beam models are able to detect 'global' modes such as bending and torsional ones. However, it was shown that higher-order beam theories are necessary when local *shell-like* modes involving the presence of lobes along the circumferential direction of the cylinder have to be characterized. Figures 1a and 1b show a two- and three-lobe mode of the cylinder, respectively. The frequency values of the first three-lobe mode are given in Table 1 for both classical and refined beam theories and the results are compared to shell and solid FEM solutions. In Table 1, N is the expansion-order of the refined beam model. More insight on the capability of the present higher-order beam models of dealing with shell- and solid-like solutions will be given during the presentation.

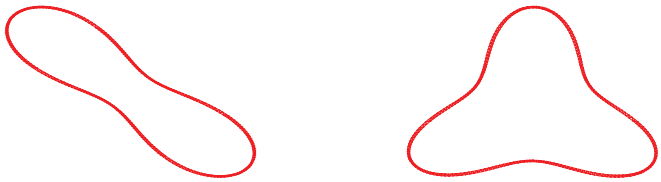

(a) Two lobes. (b) Three lobes.

Figure 1: Circumferential natural modes, 2D view, [1].

Theory	DOFs	f [Hz]
Euler-Bernoulli	93	–
Timoshenko	155	–
N = 2	558	–
N = 4	1395	75.690
N = 6	2604	52.386
N = 8	4185	40.102
Shell	49500	40.427
Solid	174000	46.444

Table 1: First three-lobe frequency [1].

The use of RBF method as opposed to FEM, in conjunction with UF, represents a powerful tool for the high-frequency response analysis of both solid and thin-walled structures and the results will be disclosed during the 9^{th} International Symposium on Vibrations of Continuous Systems.

References

[1] E. Carrera, G. Giunta, M. Petrolo, Beam Structures: Classical and Advanced Theories, John Wiley & Sons, 2011.

[2] A. W. Leissa, Vibration of Plates, NASA-SP-160, Washington DC, 1969.

[3] A. J. M. Ferreira, C. M. C. Roque, E. Carrera, M. Cinefra, (2011) Analysis of Thick Isotropic and Cross-Ply Laminated Plates by Radial Basis Functions and Unified Formulation, Journal of Sound and Vibration 330 (2011) 771–787

[4] A. Pagani, M. Boscolo, J. R. Banerjee, E. Carrera, Exact Dynamic Stiffness Elements based on One-Dimensional Higher-Order Theories for Free Vibration Analysis of Solid and Thin-Walled Structures. Submitted (2013).

Steady-State Response of Forced Cantilever with Tip Magnets

Li-Qun Chen[1,2,3], Guo-Ce Zhang[2] and Hu Ding[2]
[1] Department of Mechanics, Shanghai University, Shanghai 200444, China.
[2] Shanghai Institute of Applied Mathematics and Mechanics, Shanghai University, Shanghai 200072, China.
[3] Shanghai Key Laboratory of Mechanics in Energy Engineering, Shanghai 200072, China.

Vibration-based energy harvesting is a novel technique for powering wireless sensors [1-5]. In many cases, it is necessary to attach a proof mass to the tip of the cantilever in order to improve its dynamic flexibility. The magnetic force technique [6-10] could be used to produce nonlinearity or alter the overall stiffness of the energy harvesting device. In this paper, a vibration energy harvester will be designed and modeled as a continuous mechanical system [9, 10]. Mainly based on Challa's model [8], a straight cantilever was intended to employ on the host structure of the piezoelectric energy harvester. In addition to a variable proof mass, two permanent magnets are used: one magnet is connected to the free end of the uniform cantilever, while the other magnet is fixed to the enclosure of the device at the bottom, vertically aligned with the magnet on the beam. As a tunable harvesting device, the distance between two magnets can be controlled to alter the magnetic force.

The present investigation predicts the relative motion of a cantilever with a tip-mass and magnets. The Kelvin viscoelastic model is used to account for the damping in the cantilever. The magnetic force at the tip will be modeled as a fractional function with respect to magnetic spacing in the nonlinear boundary condition. Under the sinusoidal base excitation, both the method of multiple scales and the finite difference method are employed to determine the steady-state response of forced vibration. In the primary resonance without internal resonance, it is analytically demonstrated that the modes uninvolved in the resonance actually have no effects on the steady-state response. The results show the switch from the hardening-type behavior to the softening-type versus the augmenting magnetic force. The results can be potentially employed to enhance the amplitude of the steady-state response and broaden the frequency bandwidth of vibration-based energy harvesters.

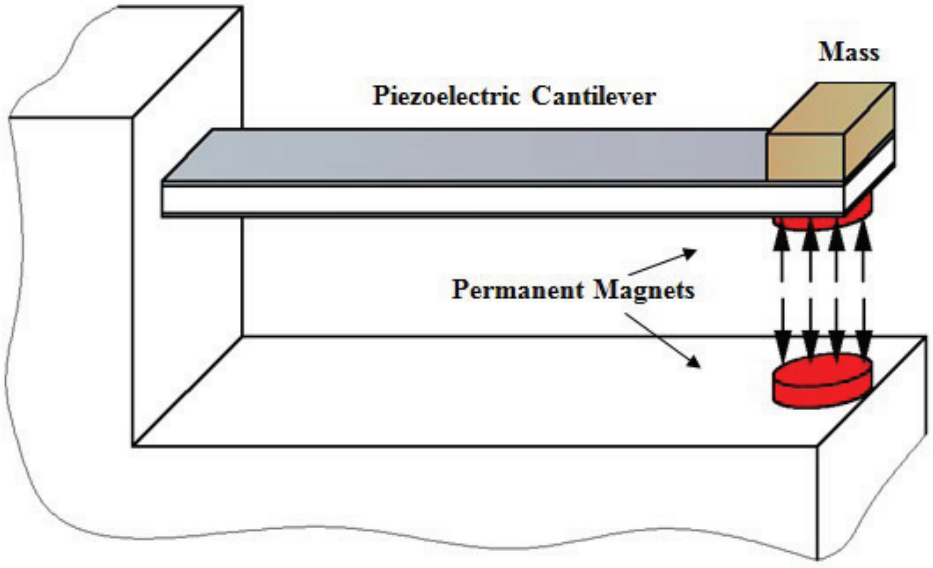

Fig. 1 Layout of cantilevered piezoelectric energy harvester with tip magnets

It is assumed that the applying cantilever is a rectangular Euler–Bernoulli beam. The base excitation is assumed to be a sinusoidal translation to simplify the problem. b and ω are the amplitude and the frequency of the external transverse load subjected to the beam, respectively. The dimensionless equation of relative motion can be obtained as

$$\begin{aligned} &z_{,tt}+z_{,xxxx}+\alpha z_{,xxxxt}=\omega^2 b\sin(\omega t);\quad z(0,t)=0;\ z_{,x}(0,t)=0;\ z_{,xx}(1,t)+\alpha z_{,xxt}(1,t)=0;\\ &z_{,xxx}(1,t)+\alpha z_{,xxxt}(1,t)+\eta\left[z_{,xxxx}(1,t)+\alpha z_{,xxxxt}(1,t)\right]+F\left(d_0+A_e+z(1,t)\right)-3A_e=0 \end{aligned} \tag{1}$$

where a comma preceding x or t denotes the partial differentiation with respect to spatial or time coordinate, and

$$F(d)=C_m\left[d^{-2}+(d+2l)^{-2}-2(d+l)^{-2}\right] \tag{2}$$

C_m is coefficient of magnetic force, A_e represents the static displacement $z(1,0)$ computed from $F(d_0+A_e)=3A_e$, η is the ratio of the tip mass to the beam mass, α is the viscoelastic coefficient, and d_0 is the distance separating two magnets.

Three time scales with a bookkeeping device ε was introduced, $T_0=t$, $T_1=\varepsilon t$, $T_2=\varepsilon^2 t$. A detuning parameter σ is also introduced to quantitatively the deviation of exciting frequency to the nth natural frequency by $\omega=\omega_n+\varepsilon^2\sigma$. A second-order uniform approximation is sought in the form of

$$z(x,t;\varepsilon)=\varepsilon Z_0(x,T_0,T_2)+\varepsilon^2 Z_1(x,T_0,T_2)+\varepsilon^3 Z_2(x,T_0,T_2)+O(\varepsilon^4) \tag{3}$$

Substituting replacements $\alpha\leftrightarrow\varepsilon^2\alpha$ and $b\leftrightarrow\varepsilon^3 b$ into the governing equation and equating the coefficients of like powers in ε will yield first three equations. In order to study the effect of adjacent modes on the nth primary resonance, the solution to the first-order equation is supposed to have relations with the mth mode and can be expressed as

$$Z_0(x,T_0,T_2)=\phi_n(x)Y_n(T_2)\mathrm{e}^{\mathrm{i}\omega_n T_0}+\phi_m(x)Y_m(T_2)\mathrm{e}^{\mathrm{i}\omega_m T_0}+cc \tag{4}$$

where cc represents the complex conjugate of all preceding terms on the right-hand side of an equation, and the frequencies can be obtained from the following equation.

$$\left(\eta\omega_k^2+F_1\right)\left(\cos\sqrt{\omega_k}\sinh\sqrt{\omega_k}-\sin\sqrt{\omega_k}\cosh\sqrt{\omega_k}\right)+\sqrt{\omega_k^3}\left(1+\cos\sqrt{\omega_k}\cosh\sqrt{\omega_k}\right)=0 \tag{5}$$

The solution to the second-order equation can be written as

$$Z_1(x,T_0,T_2)=\frac{3x^2-x^3}{6-2F_1}\left(Y_n\bar{Y}_n+Y_m\bar{Y}_m\right)F_2-F_2\left[\varphi_n Y_n^2\mathrm{e}^{2\mathrm{i}\omega_n T_0}+\varphi_m Y_m^2\mathrm{e}^{2\mathrm{i}\omega_m T_0}\right]-2F_2\left[\varphi_{nm}^{+}Y_nY_m\mathrm{e}^{\mathrm{i}(\omega_n+\omega_m)T_0}+\varphi_{nm}^{-}\bar{Y}_nY_m\mathrm{e}^{\mathrm{i}(\omega_m-\omega_n)T_0}\right]+cc \tag{6}$$

where the second-order modal functions can be computed easily.

In order to further deduce solvability conditions, the solution to the third-order equation without internal resonance is considered to be in the form of

$$Z_2(x,T_0,T_2)=Z_{2n}(x,T_2)\mathrm{e}^{\mathrm{i}\omega_n T_0}+Z_{2m}(x,T_2)\mathrm{e}^{\mathrm{i}\omega_m T_0}+cc+\mathrm{NST} \tag{7}$$

where NST is the abbreviation for non-secular terms that will not cause an unbounded solution. Substituting Eq. (7) into the third-order equation, multiplying the resulting equation by the corresponding modal function, and integrating the equation with respect to x over the interval [0, 1] will yield the solvability conditions. Combining with the boundary conditions, the repeated application of integration by parts to the resulting solvability condition will yield

$$(a)\ \mathrm{i}\lambda_n\dot{Y}_n+\mathrm{i}\alpha\mu_nY_n-\kappa_nY_n^2\bar{Y}_n-\kappa_{nm}Y_nY_m\bar{Y}_m+\frac{1}{2}\mathrm{i}\omega^2 b\chi_n\mathrm{e}^{\mathrm{i}\sigma T_2}=0;\ \ (b)\ \mathrm{i}\lambda_m\dot{Y}_m+\mathrm{i}\alpha\mu_mY_m-\kappa_mY_m^2\bar{Y}_m-\kappa_{nm}Y_n\bar{Y}_nY_m=0 \tag{8}$$

where the dot denotes derivation with respect to T_2, and the new variables are all real.

Substituting the solution to solvability condition in the polar form of $Y_k(T_2)=0.5a_k(T_2)\mathrm{e}^{\mathrm{i}\gamma_k(T_2)}$ $(k=m,n)$ into the solvability condition (8b) and then separating real and imaginary parts will yield $\lambda_m\dot{a}_m=-\alpha\mu_m a_m$. For a steady-state motion, the response amplitude from the mth mode will decay exponentially within a finite time horizon and it has little effect on the steady-state response close to the nth mode. For a steady-state motion near the nth mode, both amplitude and phase can be considered to be constant so that a_n is the solution of the following frequency-response equation.

$$\left(\alpha\mu_n a_n\right)^2+\left(\lambda_n a_n\sigma+0.25\kappa_n a_n^3\right)^2=\omega^4 b^2\chi_n^{\,2} \tag{9}$$

So far, the second-order approximation to the deflection at the free end of the cantilever is expressed as

$$z(1,t)=\varepsilon a_n\cos\left(\omega t-\theta_n\right)+\frac{F_2}{2}\left[\frac{1}{6-2F_1}-\varphi_n(1)\cos2\left(\omega t-\theta_n\right)\right]\varepsilon^2a_n^2+\cdots \tag{10}$$

Then εa_n is the approximate amplitude A_n of the steady-state response at the free end of the cantilever. Due to Lyapunov stability theory and Routh-Hurwitz criterion, the steady-state response is stable if the following condition is satisfied.

$$\left(4\alpha\mu_n\right)^2+\left(4\sigma\lambda_n+\kappa_n a_n^2\right)\left(4\sigma\lambda_n+3\kappa_n a_n^2\right)>0 \tag{11}$$

Considered dimensionless parameters are given as C_m=0.5084, l=0.004167, α=0.001, b=0.0001, d_0=0.15, and η=0.02. Fig. 2 shows the comparison on the steady-state response between the multi-scale method and the finite difference method. The theoretical analysis exhibits very good qualitative agreement with the numerical simulations. For larger amplitude, it is obvious that upward frequency sweeps are preferable to downward sweeps in the hard spring.

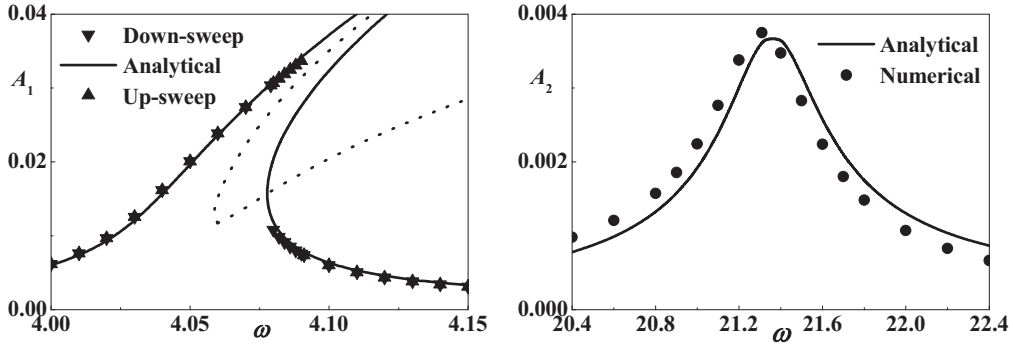

(a) the first resonance (b) the second resonance

Fig. 2 The analytical steady-state responses with numerical validation

The effects of the varying ratio on the frequency-response curve are illustrated in Fig. 3 with d_0=0.15. It is clear that the peak values for different tip masses are considerably different. Erturk and Inman presented an experiment to

obtain the response functions without magnets [10]. They also found that both the tip motion and the power output are strongly attenuated at the higher vibration modes by increasing tip mass.

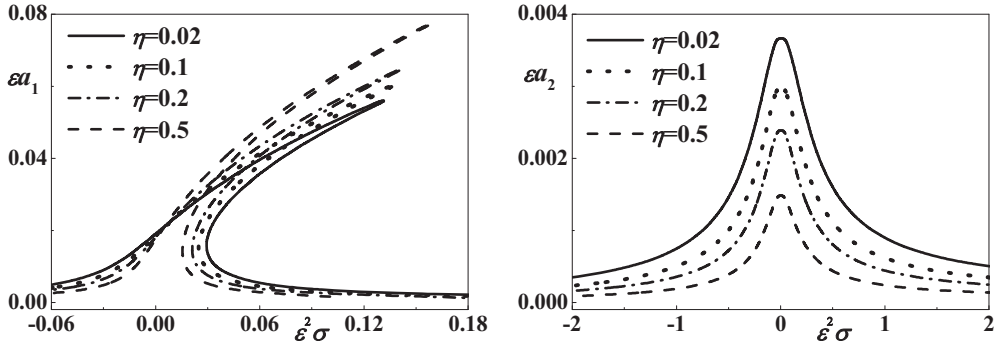

(a) the first resonance (b) the second resonance

Fig. 3 Effects of the tip mass on the frequency-response curve

For the second resonance, the separation distance between two permanent magnets almost has no effect on the response curves. For the first resonance, the peak value increases versus descending distance between two magnets as shown in Fig. 4 (a). From Fig. 4(b), evolution of jumping phenomena is a result of significant interest. Fig. 4(b) shows the displacement frequency response curves for a certain range of the magnetic spacing. The extended range of large amplitude responses is provided by engaging the nonlinearity of the magnetic interactions. The biggish magnetic force results in the softening stiffness effect, which is the opposite of the hardening stiffness effect obtained for the lesser magnetic force. For a sinusoidal excitation, the hardening-type springs increase the bandwidth for frequency up-sweeps whereas the softening-type springs enhance the bandwidth for frequency down-sweeps.

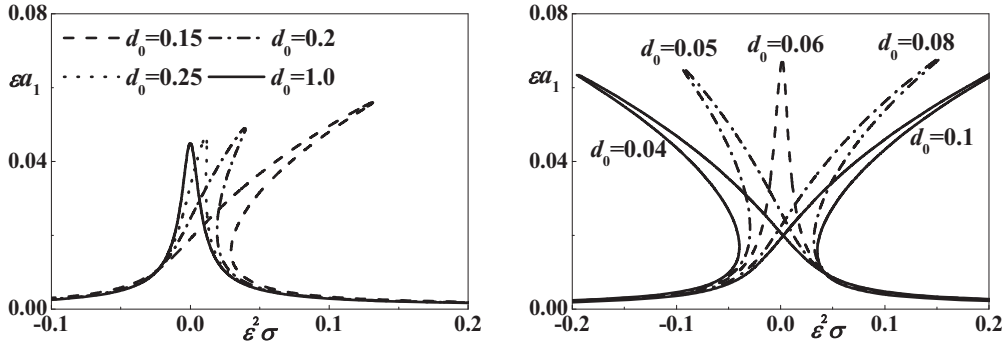

(*a*) for large spacing (*b*) for small spacing

Fig. 4 Effects of magnetic spacing on the first resonance curve

It is illustrated that the possibility of improving the effectiveness of energy harvesting via magnetic interactions. The investigation yields the following main conclusions. (1) The attachment of a tip permanent magnet can switch the frequency response curves between the hardening-type and the softening-type by adjusting the distance from the permanent magnet on the base, which potentially makes for the possible application of nonlinear vibration-based harvesters in micro-electromechanical systems. (2) The tip mass increases the response amplitude in the first mode and decreases the response amplitude in the higher order modes. (3) Any mode uninvolved in the resonance has no effect on the steady-state response of the tip-massed cantilever with the magnetic interaction in the primary resonance without internal resonances.

[1]. Williams, CB, and Yates, RB, (1996). *Sens. Actuators A*, 52(1-3): 8-11.
[2]. Zhu, DB, Tudor, M. J., and Beeby, SP, (2010). *Meas. Sci. Technol.*, 21(2): 022001.
[3]. Erturk, A, and Inman, DJ, (2008). *J. Intell. Mater. Syst. Struct.*, 19(11): 1311–1325.
[4]. Kim, JE, and Kim, YY, (2011). *J. Vibr. Acoust.*, 133(4): 041010.
[5]. Mak, KH, Popov, AA, and McWilliam, S., (2012). *J. Sound Vib.*, 331(11): 2602-2623.
[6]. Moon, FC, and Pao, YH, (1969). *J. Appl. Mech.*, 36(1):1-9.
[7]. Moon, FC, and Holmes, PJ, (1979). *J. Sound Vib.*, 65(2): 275-296.
[8]. Challa, VR, Prasad, M., Shi, Y, and Fisher, FT, (2008). *Smart Mater. Struct.*, 17(1): 015035.
[9]. Pratiher, B, and Dwivedy, SK, (2009). *J. Vibr. Acoust.*, 131(2): 021011.
[10]. Erturk, A, and Inman, DJ, (2011). *J. Sound Vib.*, 330(10): 2339-2353.

The project is supported by the State Key Program of National Natural Science of China (Grant No. 11232009).

SOME ADVANCES IN THE DEFINITION OF EXACT AND DISTORTED SIMILITUDES

S. De Rosa and F. Franco

PASTA-Lab
Department of Industrial Engineering - Aerospace Section
Universita' degli Studi di Napoli "Federico II"
Via Claudio 21, 80125, Napoli - Italy
sergio.derosa@unina.it, francesco.franco@unina.it

One of the most intriguing points of the engineering applications is the definition of prototypes (parent or similitude models) which are able, in some extent, to reproduce the response of a full-scale model. This concerns the computational field and even experimental activities but for these latter they are particularly desired. In fact the assembly of similitude models has always represented a fundamental step for a deep understanding of given phenomena at different scales; aeroelastic instabilities are one of the best examples. A well-known general view of the problems of similitudes and analogies are in the text by Szucs, [1].

The present goal is thus to get a general procedure for defining exact and distorted similitudes in order to build prototype models for linear structural and structural-acoustic responses. Previous experiences have been reported for simplified thin plates and shells, [2], [3]: the actual step is to discuss some advances for a thin stiffened cylinder. The complete procedure is named SAMSARA, *Similitude and Asymptotic Models for Structural-Acoustic Research and Application*.

The procedure is based on the Energy Distribution Approach (EDA), [4] which allows the exact derivation of input power and energy content in each of the subsystems. All the energy parameters are expressed in terms of modal coordinates and EDA allows the definition of the main similitude laws: these are derived by imposing that the responses in the original and parent models are the same. EDA computes the distribution of energy in each subsystem; thus, the whole system can be thought as an assembly of NS subsystems in which NM modes are resonating at each excitation frequency. The energy influence coefficient matrix:

$$A_{rq}^{EIC}(\omega) = \frac{\sum_j \sum_k \Gamma_{jk}(\omega)\, \psi_{jk}^{(q)} \psi_{jk}^{(r)}}{\sum_j \eta_j \omega_j \Gamma_{jj}(\omega)\, \psi_{jj}^{(q)}} \quad \text{with} \quad \begin{matrix} r, q \in \{1, \dots NS\} \\ j, k \in \{1, \dots NM\} \end{matrix} ; \tag{1}$$

the spatial coupling parameter for the generic rth subsystem is the following:

$$\psi_{jk}^{(r)} = \int_{\mathbf{x} \in r} \rho(\mathbf{x}) \phi_j(\mathbf{x}) \phi_k(\mathbf{x}) d\mathbf{x}; \tag{2}$$

the frequency dependent members are here recalled:

$$\Gamma_{jk}(\Omega) = \frac{1}{\Omega} \int_{\omega \in \Omega} \omega^2 Re \left[\frac{1}{\omega_j^2 - \omega^2 + iu\, \eta_j \omega_j^2} \frac{1}{\omega_k^2 - \omega^2 + iu\, \eta_k \omega_k^2} \right] d\omega; \tag{3}$$

the term Ω represents a generic frequency interval in which the system response is analysed for a given excitation; iu is the imaginary unit; ϕ_j is the jth global mode; ω_j is the jth circular natural frequency; η_j is the modal damping loss factor; ρ is a density function; $\mathbf{x}$ is the vector of the coordinate. The analysis of the cross terms is rather complicated and two further approximations can be used that allow separating the cross terms in large and small terms: $\Gamma_{jk}^{(large)}(\Omega)$ and $\Gamma_{jk}^{(small)}(\Omega)$, [4]. The original damping values are such that the system response can be obtained using the real eigensolutions: more complicated models based on the complex mode shapes do not add further contributions to the present developments but remain to be investigated.

Some choices are required to restrict the field of investigation: it is assumed to not change the material properties and the boundary conditions. Thus the sizes of the model and the damping can

be reduced. As a consequence any similitude model can be well represented by the variations of the damping and natural frequencies. It can be shown that the necessary condition for getting an exact similitude is that the damping ratio is kept: $r_\eta = \bar{\eta}_j/\eta_j = 1$, (the overbar denotes the items in similitude). Being $r_\omega = \bar{\omega}_j/\omega_j$ the given similitude ratio for the natural frequencies, one gets :

$$\bar{\Gamma}_{jj} = \frac{1}{r_\omega^2}\Gamma_{jj};\ \ \bar{\Gamma}_{jk}^{(large)} = \frac{1}{r_\omega^2}\Gamma_{jk}^{(large)}\ \ ;\bar{\Gamma}_{jk}^{(small)} = \frac{1}{r_\omega^2}\Gamma_{jk}^{(small)} \tag{4}$$

To proceed with the thin stiffened cylinder, the reference analytical model is well-known, [5]. The field of investigation is restricted to the analysis of the values of radius, R, thickness, h, lenght, L; the longitudinal and circumferential stiffeners are left unaltered in these simulations. Thus, these are the similitude parameters: $\alpha\alpha = \bar{L}/L$, $\beta\beta = \bar{R}/R$, $\gamma\gamma = \bar{h}/h$:

replica	exact similitude	$\alpha\alpha = \beta\beta = \gamma\gamma$
avatar	distorted similitude	$\alpha\alpha \neq \beta\beta$, $\beta\beta \neq \gamma\gamma$,$\alpha\alpha \neq \gamma\gamma$

It has to be noted that the r_ω in the cylinder can assume different laws depending on the nature of the involved modes: in the avatars it is a frequency dependent function.

Two simple results are shown in Figures 1 and 2 for an aluminium cylinder (NCL and NCR are the number of longitudinal and circumferential stiffeners, and NMX and NMY are the number of assumed modes). In both the figures, the distribution of natural frequencies is reported together with a forced response. This last is a radial component of the structural velocity as result of a mechanical point excitation. The knowledge of r_ω allows defining the remodulation of the frequency axis, so that the original model and the avatar (or replica) can be directly compared, by remodulating the response axis too.
The replica, Fig. 1, perfectly replicates the original response even using a reduction of thickness, length and radius: $\alpha\alpha = \beta\beta = \gamma\gamma = 0.5$. The avatar is a very good approximation too, Fig. 2, $\alpha\alpha = \beta\beta = 0.2; \gamma\gamma = 0.5$.

The analyses here summarised are at their preliminary stages ; here it has been also assumed to keep the original stiffeners. Nevertheless, the promising results allow thinking that the goal of having useful avatars can be pursued even if only an experimental campaign will give more information about the real possibilities.

REFERENCES

[1] E. Szucs. Similitude and Modelling. Elsevier Science Ltd, ISBN:0444997806, 1980.

[2] S. De Rosa, F. Franco and T. Polito. Structural similitude for the dynamic response of plates and assemblies of plates. Mechanical Systems and Signal Processing, 25(3), 969-980, 2011.

[3] S. De Rosa, F. Franco, T. Polito. SAMSARA for thin cylindrical shells. Proceed. of the NOVEM2012 Conference, Noise and Vibration: Emerging Methods, April 2012, Sorrento, Italy, ISBN:9788890648403, no.48

[4] B. R. Mace. Statistical energy analysis, energy distribution models and system modes. Journal of Sound and Vibration, 264, 391-409, 2003.

[5] Martin M. Mikulas, Jr., and John A. McElman. On free vibrations of eccentrically stiffened cylindrical shells and flat plates. NASA TN D-3010, 1967

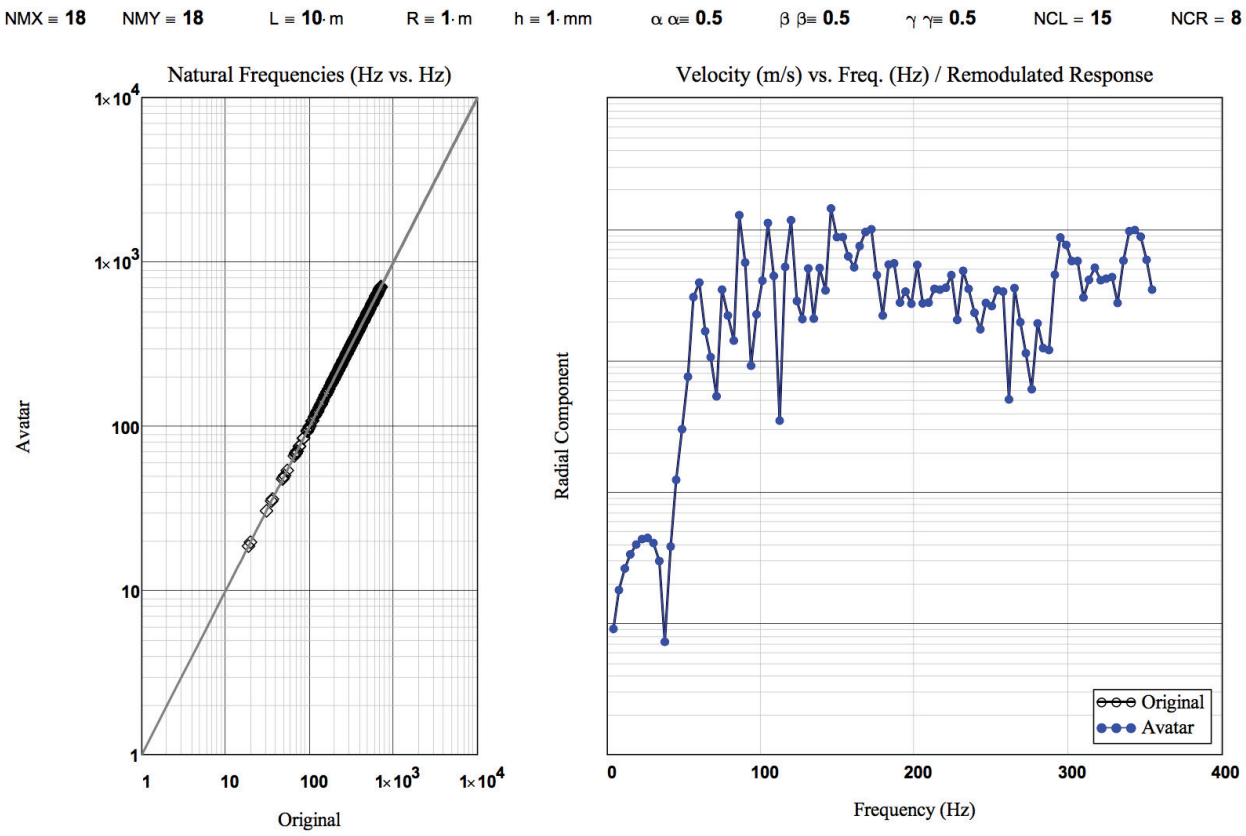

Figure 1. Exact similitude: *replica* natural frequencies and response

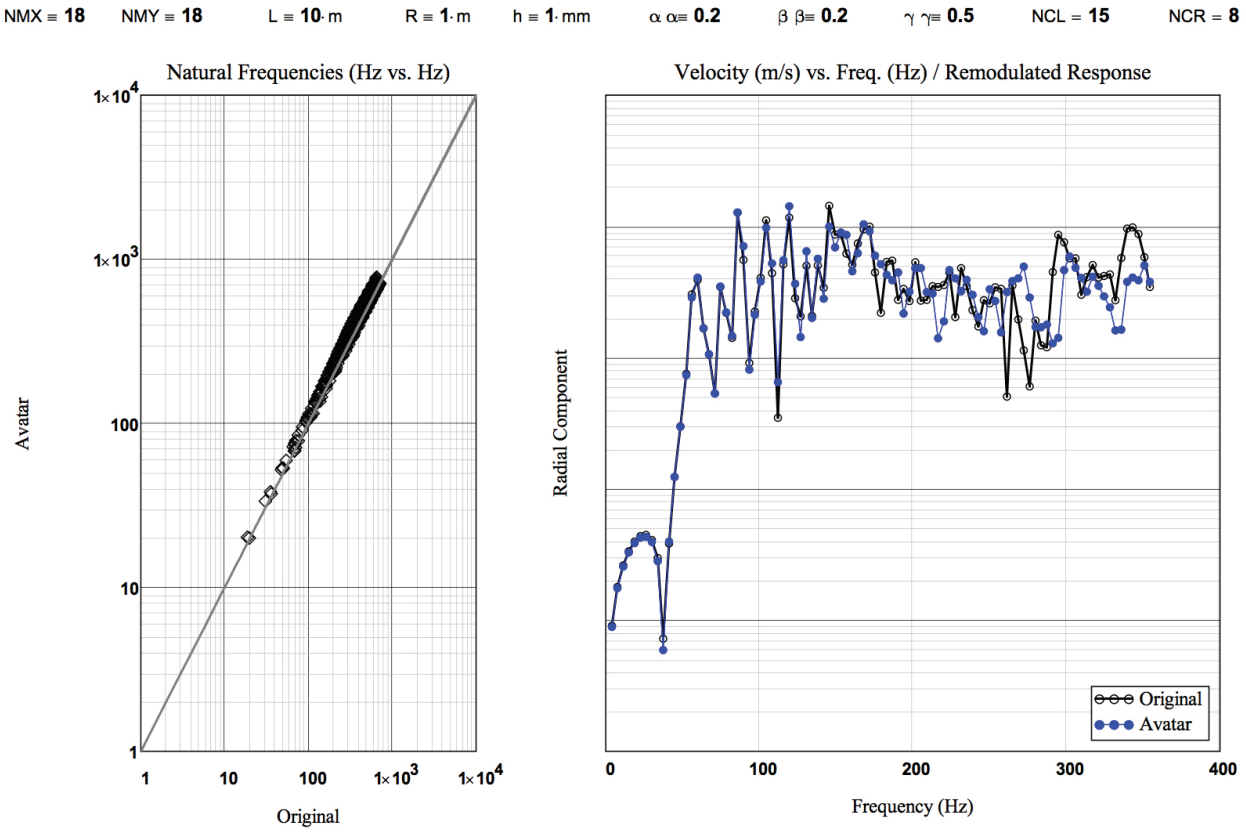

Figure 2. Distorted similitude: *avatar* natural frequencies and response

Transmission and Reflection of Mechanical Waves at an Interface

S.B. Dong

Civil and Environmental Engineering Department
University of California
Los Angeles, California, 90095-1593, USA

We are concerned with two dissimilar prismatic bars joined at an interface whose unit normal lies parallel to the axes of these members. Each bar may have its own cross-sectional shape and its own general (anisotropic) properties. Locate the origin of coordinates somewhere within this interface. In the prismatic member occupying the positive portion of the z-axis, assume a steady-state mechanical wave of frequency ω is traveling in the negative z-direction. When this signal impinges upon the interface between the two bars, systems of transmitted and reflected waves are generated, the nature of which depends upon ω and all of the geometrical and mechanical properties of both members. Herein, a method of analysis for characterizing the nature of the transmitted and reflective wave fields on a three-dimensional basis is presented.

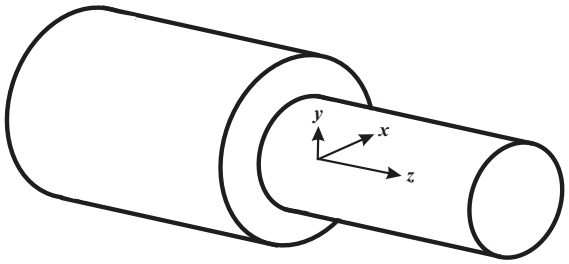

The spectral data characterizing the reflected and transmitted waves are obtained from semi-analytical finite element models of the two beams. In this method, the behavior dependent on the cross-sectional coordinates is represented by interpolation polynomials and that along the beam's axis z and time t is kept analytical. For each beam, a system of partial differential equations of the following form in z and t is obtained.

$$\mathbf{K_1 U_{,zz} - K_2 U_{,z} - K_3 U + M\ddot{U} = 0} \tag{1}$$

Spectral decomposition of Eq. (1) using solution form $\mathbf{U}(z,t) = \mathbf{U_o} e^{i(kz-\omega t)}$ of both members gives the data used to synthesize the behavior of the reflected and transmitted waves. For each member, the spectral decomposition takes the form of a complex quadratic algebraic eigenproblem where k acts as the eigenvalue parameter.

$$k^2\mathbf{U}_o + ik\mathbf{K}_1^{-1}\mathbf{K}_2\mathbf{U}_0 + \mathbf{K}_1^{-1}\big(\mathbf{K}_3 - \omega^2\mathbf{M}\big)\mathbf{U}_0 = 0 \tag{2}$$

By introducing $\mathbf{U}_1 = k\mathbf{U}_0$ into algebraic eigensystem (2), it is possible to reduce the algebraic eigenproblem to 1st order canonical form.

$$\begin{bmatrix} \cdot & \mathbf{I} \\ -\mathbf{K}_1^{-1}\big(\mathbf{K}_3 - \omega^2\mathbf{M}\big) & -i\mathbf{K}_1^{-1}\mathbf{K}_2 \end{bmatrix} \begin{Bmatrix} \mathbf{U}_o \\ \mathbf{U}_1 \end{Bmatrix} = k \begin{Bmatrix} \mathbf{U}_o \\ \mathbf{U}_1 \end{Bmatrix} \tag{2}$$

Real eigendata extracted from Eq. (2) are associated with propagating modes, while complex eigenvalues describe *end modes*. A complex conjugate pair, $k_R \pm ik_I$, describe standing vibrations with amplitudes regressing from the free end of a semi-infinitely long cylinder exponentially into its interior, one toward the positive z-direction and the other in the opposite direction. Purely imaginary eigenvalues describe monotonic exponential decay, while complex eigenvalues represent sinusoidal decay. For each eigenvalue k_m, there are right-handed and left-handed eigenvectors, $\boldsymbol{\phi}_m$ and $\boldsymbol{\psi}_m$, respectively, that satisfy Eq. (2) and its adjoint. Moreover, the eigenvectors satisfy the bi-orthogonality relations

$$\boldsymbol{\Psi}^T\boldsymbol{\Phi} \;=\; diag(B_n) \quad ; \quad \boldsymbol{\Psi}^T\mathbf{A}\boldsymbol{\Phi} \;=\; diag(B_n\, i\, k_n) \tag{3}$$

Analysis Procedure

We are concerned with steady-state behavior and more pertinently, the reflection-transmission phenomenon at the interface $z = 0$. Thus, the axial and time dependence, given by $e^{-i(kz-\omega t)}$, for $z = 0$, reduces to $e^{-i\omega t}$. Since this factor occurs throughout, it may be suppressed without confusion.

Let $\mathbf{U_{INC}}$ and $\mathbf{S_{INC}}$ denote the nodal displacements and cross-sectional surface tractions at the Guassian integration points of the incoming wave, which at the interface $z = 0$ have the form

$$\mathbf{U_{INC}} = A_{INC}\mathbf{U_0} \qquad ; \qquad \mathbf{S_{INC}} = A_{INC}\mathbf{S_0} \tag{4}$$

If this bar contains a region not continuous with the transmitted portion of the system of bars, then the incident wave displacement and traction components must be subdivided into two portions,

$$\mathbf{U_{INC}} = A_{INC}\mathbf{U_0^1} + A_{INC}\mathbf{U_0^2} \quad ; \quad \mathbf{S_{INC}} = A_{INC}\mathbf{S_0^1} + A_{INC}\mathbf{S_0^2} \tag{5}$$

where superscripts 1 and 2 denote the continuous portion and traction-free portion, respectively.

Let subscripts m and n be indices identifying the modes comprising the reflected and transmitted wave forms. Thus, the reflected and transmitted waves, which travel in the positive adn negative z-directions, respectively, at $z = 0$ can be stated as

$$\mathbf{U_{ref}} = \sum_{m=1}^{N} \mathbf{a_{ref-m}}\, \boldsymbol{\phi_m} \qquad ; \qquad \mathbf{S_{ref}} = \sum_{m=1}^{N} \mathbf{a_{ref-m}}\, \mathbf{s_m} \tag{6}$$

$$\mathbf{U_{tr}} = \sum_{n=1}^{N} \mathbf{b_{tr-n}}\ \boldsymbol{\phi_n} \qquad ; \qquad \mathbf{S_{tr}} = \sum_{n=1}^{N} \mathbf{b_{tr-n}}\ \mathbf{s_n} \tag{7}$$

Similarly, if a portion of a given bar is not continuous with its counterpart on either side of the inteface, then its displacement and traction components appear as

$$\mathbf{U_{ref}} = \sum_{m=1}^{N} \mathbf{a_{ref-m}}\ \boldsymbol{\phi}^1_{\mathbf{m}} + \sum_{m=1}^{N} \mathbf{a_{ref-m}}\ \boldsymbol{\phi}^2_{\mathbf{m}} \ ; \ \mathbf{S_{ref}} = \sum_{m=1}^{N} \mathbf{a_{ref-m}}\ \mathbf{s}^{\mathbf{2}}_{\mathbf{m}} + \sum_{m=1}^{N} \mathbf{a_{ref-m}}\ \mathbf{s}^{\mathbf{2}}_{\mathbf{m}} \tag{8}$$

or

$$\mathbf{U_{tr}} = \sum_{n=1}^{N} \mathbf{b_{tr-n}}\ \boldsymbol{\phi}^1_{\mathbf{n}} + \sum_{n=1}^{N} \mathbf{b_{tr-n}}\ \boldsymbol{\phi}^2_{\mathbf{n}} \ ; \ \mathbf{S_{tr}} = \sum_{n=1}^{N} \mathbf{b_{tr-n}}\ \mathbf{s}^{\mathbf{1}}_{\mathbf{n}} + \sum_{n=1}^{N} \mathbf{b_{tr-n}}\ \mathbf{s}^{\mathbf{2}}_{\mathbf{n}} \tag{9}$$

where the superscripts 1 and 2 denote the continuous portion and traction-free portion, respectively.

Suppose the incident portion of the system contains a portion on the interface that is traction-free, then Eqs. (5),(7), and (8) are applicable. Enforcing interface continuity of displacement and surface traction as well as traction-free conditions on the exposed (free) portion of the cross-section yield the following set of matrix equations

$$\begin{bmatrix} \boldsymbol{\Phi}^1_{\mathbf{m}} & -\boldsymbol{\Phi}_{\mathbf{n}} \\ \mathbf{S}^{\mathbf{1}}_{\mathbf{m}} & \mathbf{S_n} \\ \mathbf{S}^{\mathbf{2}}_{\mathbf{m}} & . \end{bmatrix} \begin{Bmatrix} \mathbf{A}_{ref} \\ \mathbf{B}_{tr} \end{Bmatrix} = -A_{INC} \begin{Bmatrix} \mathbf{U}^{\mathbf{1}}_{\mathbf{0}} \\ \mathbf{S}^{\mathbf{1}}_{\mathbf{0}} \\ \mathbf{S}^{\mathbf{2}}_{\mathbf{0}} \end{Bmatrix} \qquad \rightarrow \quad \boldsymbol{P}_1 \boldsymbol{V} = -A_{INC} \boldsymbol{F}_1 \tag{10}$$

If, on the other hand, the transmitted portion contains a portion of the interface that is traction-free, then Eqs. (4), (6) and (9) apply, which result in

$$\begin{bmatrix} \boldsymbol{\Phi}_{\mathbf{m}} & -\boldsymbol{\Phi}^1_{\mathbf{n}} \\ \mathbf{S_m} & \mathbf{S}^{\mathbf{1}}_{\mathbf{n}} \\ . & \mathbf{S}^{\mathbf{2}}_{\mathbf{n}} \end{bmatrix} \begin{Bmatrix} \mathbf{A}_{ref} \\ \mathbf{B}_{tr} \end{Bmatrix} = -A_{INC} \begin{Bmatrix} \mathbf{U_0} \\ \mathbf{S_0} \\ \mathbf{0} \end{Bmatrix} \qquad \rightarrow \quad \boldsymbol{P}_2 \boldsymbol{V} = -A_{INC} \boldsymbol{F}_2 \tag{11}$$

The solution for $\boldsymbol{V} = [\mathbf{A}_{ref} \quad \mathbf{B}_{tr}]^T$ in Eq. (10) or (11), which are the coefficients of the reflected and transmitted modes, can be obtained on a least-squares basis by pre-multiplying each equation by its hermitian transpose, i.e., by $\boldsymbol{P}_1^H$ or $\boldsymbol{P}_2^H$, respectively, and then by inversion.

$$\boldsymbol{V} = -A_{INC} \Big[\boldsymbol{P}_i^H \boldsymbol{P}_i \Big]^{-1} \Big[\boldsymbol{P}_i^H \boldsymbol{F}_i \Big] \qquad (i = 1, 2) \tag{12}$$

Some interesting cases will be presented at the Symposium.

References

1. Taweel, H., Dong, S.B. and Kazic, M., (2000), Wave Reflection from the Free End of a Cylinder with an Arbitrary Cross-Section, *Int. J. Solids Structures*, **37**, 1701-1726.

Levy-type vibration solutions of cross-ply laminated plates based on refined variable-kinematic theories

Lorenzo Dozio
Department of Aerospace Science and Technology, Politecnico di Milano, Italy

Introduction. Exact solutions for free vibration of structural elements can serve as a quick tool for understanding the dynamic response, a reference for verification of computational methods or a basis for development of advanced modelling techniques such as the dynamic stiffness method. It is well known that analytical solutions can be developed for rectangular laminated plates with certain lamination schemes and boundary conditions. In particular, the Levy method can be adopted when one pair of opposite edges are simply supported and the remaining two edges having any possible combination of free, simple support or fixed conditions. However, the mathematical effort needed to derive the exact solutions can be considerable, especially when the plate is modelled according to higher-order equivalent single-layer (ESL) or layer wise (LW) kinematic theories. Furthermore, the solving equations must be re-derived when the plate theory has changed. The novel procedure introduced here overcomes the above shortcomings. It can be considered as an application to the Levy method of the unified formulation developed by Carrera [1]. Using the present approach, Levy-type vibration solutions based on refined variable-kinematic theories can be obtained for laminated plates in an efficient and automatic way.

Preliminaries. Consider a cross-ply laminated rectangular plate of length a, width b and thickness h. The plate consists of N_ℓ layers, which are assumed to be homogeneous and made of orthotropic material of mass density ρ^k. The k-th layer has thickness h_k and is located between interfaces $z = z_k$ and $z = z_{k+1}$ in the thickness direction. The constitutive equations of a generic layer k are written as $\boldsymbol{\sigma}^k_{\mathrm{p}} = \tilde{\mathbf{C}}^k_{\mathrm{pp}}\boldsymbol{\epsilon}^k_{\mathrm{p}} + \tilde{\mathbf{C}}^k_{\mathrm{pn}}\boldsymbol{\epsilon}^k_{\mathrm{n}}$ and $\boldsymbol{\sigma}^k_{\mathrm{n}} = \tilde{\mathbf{C}}^k_{\mathrm{np}}\boldsymbol{\epsilon}^k_{\mathrm{p}} + \tilde{\mathbf{C}}^k_{\mathrm{nn}}\boldsymbol{\epsilon}^k_{\mathrm{n}}$, where $\boldsymbol{\sigma}$ and $\boldsymbol{\epsilon}$ are the stresses and strains, split into in-plane (p) and out-of-plane (n) components, and matrices $\tilde{\mathbf{C}}$ contain the elastic coefficients in the plate reference system. Refined 2-D kinematic theories are employed by expressing the displacement vector for the k-th lamina through an indicial notation over τ as follows:

$$\mathbf{u}^k(x, y, \zeta_k, t) = F_\tau(\zeta_k)\mathbf{u}^k_\tau(x, y, t) \tag{1}$$

where $\mathbf{u}^k_\tau = \left\{ \begin{array}{ccc} u^k_\tau & v^k_\tau & w^k_\tau \end{array} \right\}$ is the vector of kinematic variables, $\tau = t, r, b$, $r = 2, \ldots, N-1$, ζ_k is the local dimensionless layer coordinate ($-1 \leq \zeta_k \leq 1$), N is the order of the theory, and $F_\tau(\zeta_k)$ are assumed thickness functions. In case of LW theories, they are taken as a combination of Legendre polynomials in order to satisfy the interlaminar continuity of the displacements. If an ESL theory is adopted, global thickness functions $F_\tau(z)$ are assumed as terms of a Taylor z expansion. Note that in Eq. (1) the summation convention for repeated indices is implied. Using Eq. (1), strains are linearly related to displacements as $\boldsymbol{\epsilon}^k_{\mathrm{p}} = F_\tau \boldsymbol{\mathcal{D}}_{\mathrm{p}}\mathbf{u}^k_\tau$ and $\boldsymbol{\epsilon}^k_{\mathrm{n}} = F_\tau \boldsymbol{\mathcal{D}}_{\mathrm{n}}\mathbf{u}^k_\tau + F_{\tau_z}\mathbf{u}^k_\tau$, where $\boldsymbol{\mathcal{D}}_{\mathrm{p}}$ and $\boldsymbol{\mathcal{D}}_{\mathrm{n}}$ are matrices of differential operators and $F_{\tau_z} = \mathrm{d}F_\tau/\mathrm{d}z$.

Governing equations at layer level. Substituting the constitutive equations and the strain-displacement relations into the principle of virtual displacements, integrating by parts and imposing the definition of virtual variations for the unknown displacements yield the following set of equations

of motion over the plate domain $\Omega = [0, a] \times [0, b]$ for the k-th layer

$$\boldsymbol{\mathcal{L}}^{k\tau s}\mathbf{u}_s^k = \rho^k J_{\tau s}^k \ddot{\mathbf{u}}_s^k \qquad (\tau, s = t, r, b) \tag{2}$$

where $\boldsymbol{\mathcal{L}}^{k\tau s}$ is a 3×3 nucleus matrix of differential operators given by

$$\begin{aligned}\boldsymbol{\mathcal{L}}^{k\tau s} = {} & \boldsymbol{\mathcal{D}}_{\mathrm{p}}^{\mathrm{T}}\tilde{\mathbf{C}}_{\mathrm{pp}}^k J_{\tau s}^k \boldsymbol{\mathcal{D}}_{\mathrm{p}} + \boldsymbol{\mathcal{D}}_{\mathrm{p}}^{\mathrm{T}}\tilde{\mathbf{C}}_{\mathrm{pn}}^k J_{\tau s}^k \boldsymbol{\mathcal{D}}_{\mathrm{n}} + \boldsymbol{\mathcal{D}}_{\mathrm{p}}^{\mathrm{T}}\tilde{\mathbf{C}}_{\mathrm{pn}}^k J_{\tau s_z}^k \\ & + \boldsymbol{\mathcal{D}}_{\mathrm{n}}^{\mathrm{T}}\tilde{\mathbf{C}}_{\mathrm{np}}^k J_{\tau s}^k \boldsymbol{\mathcal{D}}_{\mathrm{p}} + \boldsymbol{\mathcal{D}}_{\mathrm{n}}^{\mathrm{T}}\tilde{\mathbf{C}}_{\mathrm{nn}}^k J_{\tau s}^k \boldsymbol{\mathcal{D}}_{\mathrm{n}} + \boldsymbol{\mathcal{D}}_{\mathrm{n}}^{\mathrm{T}}\tilde{\mathbf{C}}_{\mathrm{nn}}^k J_{\tau s_z}^k \\ & - \tilde{\mathbf{C}}_{\mathrm{np}}^k J_{\tau_z s}^k \boldsymbol{\mathcal{D}}_{\mathrm{p}} - \tilde{\mathbf{C}}_{\mathrm{nn}}^k J_{\tau_z s}^k \boldsymbol{\mathcal{D}}_{\mathrm{n}} - \tilde{\mathbf{C}}_{\mathrm{nn}}^k J_{\tau_z s_z}^k\end{aligned} \tag{3}$$

and $J_{\tau s}^k = \int_{z_k}^{z_{k+1}} F_\tau F_s \mathrm{d}z$, $J_{\tau s_z}^k = \int_{z_k}^{z_{k+1}} F_\tau F_{s_z} \mathrm{d}z$, $J_{\tau_z s}^k = \int_{z_k}^{z_{k+1}} F_{\tau_z} F_s \mathrm{d}z$, and $J_{\tau_z s_z}^k = \int_{z_k}^{z_{k+1}} F_{\tau_z} F_{s_z} \mathrm{d}z$. Accordingly, the boundary conditions along the plate boundary Γ can be compactly expressed as

$$\boldsymbol{\mathcal{B}}^{k\tau s}\mathbf{u}_s^k = \mathbf{0} \qquad (\tau, s = t, r, b) \tag{4}$$

where the 3×3 boundary-related nucleus matrix $\boldsymbol{\mathcal{B}}^{k\tau s}$ is given by

$$\begin{aligned}\boldsymbol{\mathcal{B}}^{k\tau s} &= \mathbf{I} \qquad \text{(geometrical)} \\ \boldsymbol{\mathcal{B}}^{k\tau s} &= \boldsymbol{\mathcal{N}}_{\mathrm{p}}^{\mathrm{T}}\tilde{\mathbf{C}}_{\mathrm{pp}}^k J_{\tau s}^k \boldsymbol{\mathcal{D}}_{\mathrm{p}} + \boldsymbol{\mathcal{N}}_{\mathrm{p}}^{\mathrm{T}}\tilde{\mathbf{C}}_{\mathrm{pn}}^k J_{\tau s}^k \boldsymbol{\mathcal{D}}_{\mathrm{n}} + \boldsymbol{\mathcal{N}}_{\mathrm{p}}^{\mathrm{T}}\tilde{\mathbf{C}}_{\mathrm{pn}}^k J_{\tau s_z}^k \\ &\quad + \boldsymbol{\mathcal{N}}_{\mathrm{n}}^{\mathrm{T}}\tilde{\mathbf{C}}_{\mathrm{np}}^k J_{\tau s}^k \boldsymbol{\mathcal{D}}_{\mathrm{p}} + \boldsymbol{\mathcal{N}}_{\mathrm{n}}^{\mathrm{T}}\tilde{\mathbf{C}}_{\mathrm{nn}}^k J_{\tau s}^k \boldsymbol{\mathcal{D}}_{\mathrm{n}} + \boldsymbol{\mathcal{N}}_{\mathrm{n}}^{\mathrm{T}}\tilde{\mathbf{C}}_{\mathrm{nn}}^k J_{\tau s_z}^k \qquad \text{(natural)}\end{aligned} \tag{5}$$

and $\boldsymbol{\mathcal{N}}_{\mathrm{p}}$ and $\boldsymbol{\mathcal{N}}_{\mathrm{n}}$ are matrices containing the components n_x and n_y of the outward normal.

The solution procedure. A Levy-type solution satisfying the simply-supported boundary conditions at edges $y = 0, b$ is sought as follows

$$\mathbf{u}_s^k = \left\{ \begin{array}{c} U_{sm}^k(x) \sin(\beta_m y) \\ V_{sm}^k(x) \cos(\beta_m y) \\ W_{sm}^k(x) \sin(\beta_m y) \end{array} \right\} e^{j\omega_m t} \tag{6}$$

where ω_m denotes the unknown eigenfrequency associated with the m-th eigenmode and $\beta_m = m\pi/b$. Substituting of solution (6) into Eqs. (2) yields, for each $m = 1, 2, \ldots$, the following system of ordinary differential equations for the k-th layer

$$\mathbf{L}_2^{k\tau s}\frac{\mathrm{d}^2\mathbf{U}_s^k}{\mathrm{d}x^2} - \mathbf{L}_1^{k\tau s}\frac{\mathrm{d}\mathbf{U}_s^k}{\mathrm{d}x} - \mathbf{L}_0^{k\tau s}\mathbf{U}_s^k = \mathbf{0} \qquad (\tau, s = t, r, b) \tag{7}$$

where $\mathbf{U}_s^k(x) = \left\{ U_{sm}^k(x) \quad V_{sm}^k(x) \quad W_{sm}^k(x) \right\}^{\mathrm{T}}$ and

$$\mathbf{L}_0^{k\tau s} = \begin{bmatrix} l_{11} & 0 & 0 \\ 0 & l_{22} & l_{23} \\ 0 & l_{23} & l_{33} \end{bmatrix} \qquad \begin{aligned} l_{11} &= \beta_m^2 \tilde{C}_{66}^k J_{\tau s}^k + \tilde{C}_{55}^k J_{\tau_z s_z}^k - \rho^k J_{\tau s}^k \omega_m^2 \\ l_{22} &= \beta_m^2 \tilde{C}_{22}^k J_{\tau s}^k + \tilde{C}_{44}^k J_{\tau_z s_z}^k - \rho^k J_{\tau s}^k \omega_m^2 \\ l_{33} &= \beta_m^2 \tilde{C}_{44}^k J_{\tau s}^k + \tilde{C}_{33}^k J_{\tau_z s_z}^k - \rho^k J_{\tau s}^k \omega_m^2 \\ l_{23} &= \beta_m (\tilde{C}_{44}^k J_{\tau_z s}^k - \tilde{C}_{23}^k J_{\tau s_z}^k) \end{aligned}$$

$$\mathbf{L}_1^{k\tau s} = \begin{bmatrix} 0 & l_{12} & l_{13} \\ -l_{12} & 0 & 0 \\ -l_{13} & 0 & 0 \end{bmatrix} \qquad \begin{aligned} l_{12} &= \beta_m (\tilde{C}_{12}^k + \tilde{C}_{66}^k) J_{\tau s}^k \\ l_{13} &= \tilde{C}_{55}^k J_{\tau_z s}^k - \tilde{C}_{13}^k J_{\tau s_z}^k \end{aligned} \qquad \mathbf{L}_2^{k\tau s} = J_{\tau s}^k \begin{bmatrix} \tilde{C}_{11}^k & 0 & 0 \\ 0 & \tilde{C}_{66}^k & 0 \\ 0 & 0 & \tilde{C}_{55}^k \end{bmatrix}$$

Note that $\mathbf{L}_0^{k\tau s} = \mathbf{L}_0^{k\tau s}(\omega_m)$. By varying the theory-related indices τ and s over the defined ranges, the 3×3 nuclei $\mathbf{L}_i^{k\tau s}$ $(i = 0, 1, 2)$ are expanded so that a new system of equations can be obtained as follows

$$\mathbf{L}_2^k \frac{\mathrm{d}^2\mathbf{U}^k}{\mathrm{d}x^2} - \mathbf{L}_1^k \frac{\mathrm{d}\mathbf{U}^k}{\mathrm{d}x} - \mathbf{L}_0^k \mathbf{U}^k = \mathbf{0} \tag{8}$$

where

$$\mathbf{L}_i^k = \begin{bmatrix} \mathbf{L}_i^{ktt} & \mathbf{L}_i^{ktr} & \mathbf{L}_i^{ktb} \\ \mathbf{L}_i^{krt} & \mathbf{L}_i^{krr} & \mathbf{L}_i^{krb} \\ \mathbf{L}_i^{kbt} & \mathbf{L}_i^{kbr} & \mathbf{L}_i^{kbb} \end{bmatrix} \qquad \begin{matrix} (i=0,1,2) \\ (r=2,\ldots,N) \end{matrix} \qquad \mathbf{U}^k(x) = \begin{Bmatrix} \mathbf{U}_t^k(x) \\ \mathbf{U}_r^k(x) \\ \mathbf{U}_b^k(x) \end{Bmatrix} \tag{9}$$

The final set of equations for the multilayer plate is written as

$$\mathbf{L}_2 \frac{\mathrm{d}^2\mathbf{U}}{\mathrm{d}x^2} - \mathbf{L}_1 \frac{\mathrm{d}\mathbf{U}}{\mathrm{d}x} - \mathbf{L}_0\mathbf{U} = \mathbf{0} \qquad (\text{in } \Omega) \tag{10}$$

where $\mathbf{U}(x)$ is the vector containing all the independent kinematic variables $\mathbf{U}^k(x)$ $(k=1,\ldots,N_\ell)$, and the resulting matrices $\mathbf{L}_i$ are simply summed layer-by-layer in case of ESL theories or assembled by enforcing the interlaminar continuity condition in case of LW theories. A similar expansion and assembly procedure is applied to obtain the system of boundary conditions at edges $x=0,a$

$$\mathbf{B}_1 \frac{\mathrm{d}\mathbf{U}}{\mathrm{d}x} + \mathbf{B}_0\mathbf{U} = \mathbf{0} \qquad (x=0,a) \tag{11}$$

starting from the boundary-related nuclei $\mathbf{B}_i^{k\tau s}$ $(i=0,1)$. For example, when one edge is assumed to be free, the corresponding nuclei are given by

$$\mathbf{B}_1^{k\tau s} = J_{\tau s}^k \begin{bmatrix} \tilde{C}_{11}^k & 0 & 0 \\ 0 & \tilde{C}_{66}^k & 0 \\ 0 & 0 & \tilde{C}_{55}^k \end{bmatrix} \qquad \mathbf{B}_0^{k\tau s} = \begin{bmatrix} 0 & -\beta_m \tilde{C}_{12}^k J_{\tau s}^k & \tilde{C}_{13}^k J_{\tau s_z}^k \\ \beta_m \tilde{C}_{66}^k J_{\tau s}^k & 0 & 0 \\ \tilde{C}_{55}^k J_{\tau s_z}^k & 0 & 0 \end{bmatrix} \tag{12}$$

A state space approach is used to solve the free vibration problem by converting Eqs. (10) and (11) into a first-order form as follows

$$\frac{\mathrm{d}\mathbf{Z}}{\mathrm{d}x} = \mathbf{A}\mathbf{Z} \qquad \mathbf{A} = \begin{bmatrix} \mathbf{L}_2 & \mathbf{0} \\ \mathbf{0} & \mathbf{I} \end{bmatrix}^{-1} \begin{bmatrix} \mathbf{L}_1 & \mathbf{L}_0 \\ \mathbf{I} & \mathbf{0} \end{bmatrix} \qquad \mathbf{Z}(x) = \begin{Bmatrix} \mathrm{d}\mathbf{U}/\mathrm{d}x \\ \mathbf{U} \end{Bmatrix}$$

$$\mathbf{B}\mathbf{Z} = \mathbf{0} \qquad (x=0,a) \qquad \mathbf{B} = \begin{bmatrix} \mathbf{B}_1 & \mathbf{B}_0 \end{bmatrix}$$

A general solution can be expressed as

$$\mathbf{Z}(x) = e^{\mathbf{A}x}\mathbf{c} = \mathbf{V}\mathrm{Diag}\left(e^{\lambda_i x}\right)\mathbf{V}^{-1}\mathbf{c} = \mathbf{H}\mathbf{c} \tag{13}$$

where $\mathbf{c}$ is a vector of constants connected to boundary conditions, $\mathbf{V}$ is the matrix of eigenvectors of $\mathbf{A}$ and λ_i are the corresponding eigenvalues. Replacement of solution (13) into the system of boundary equations yield a homogeneous system

$$\mathbf{B}\mathbf{H}\mathbf{c} = \mathbf{K}\mathbf{c} = \mathbf{0} \qquad (x=0,a) \tag{14}$$

The natural frequencies associated with the m-th mode and the assumed boundary conditions at edges $x=0,a$ are determined by setting $|\mathbf{K}|=0$. Note that, since $\mathbf{K}=\mathbf{K}(\omega_m)$, an iterative numerical procedure has been employed to derive the frequency parameters.

Numerical results. Considerably different vibration results have been obtained for cross-ply plates of various thickness-to-length ratios, degree of orthotropy and boundary conditions at edges $x=0,a$. Comparisons with other exact solutions and appropriate conclusions concerning the accuracy of various theories will be presented at the symposium.

References

[1] E. Carrera, Theories and finite elements for multilayered, anisotropic, composite plates and shells, *Archives of Computational Methods in Engineering*, 9 (2002), 87-140.

Dynamic Stiffness Analysis of Clamped Plates – New Analytic Formulation

Moshe Eisenberger and Aharon Deutsch

Faculty of Civil and Environmental Engineering

Technion – Israel Institute of Technology

Technion City, Haifa, Israel

e-mail: cvrmosh@technion.ac.il

The vibration analysis of plates is a widely researched area. A complete assembly of the subject was compiled by Leissa in 1973[1]. Since, hundreds of papers were published on the topic. The problem can be divided into two groups: the first group includes cases for which an analytical solution is known (Navier and Levy solutions). These are cases with at least two opposite edges simply supported. The second group includes cases with clamped edges, free edges, and simply supported edges not included in the first group. For the second group semi analytical and numerical solutions are in use. Benchmark solutions for the cases in the second group are highly desired for comparison of existing and future methods.

In this work a new method is presented for the analysis of clamped plates. The solutions for the natural frequencies of the plates are found using static analysis. Starting from the equations of motion of a thin isotropic rectangular plate, using the classical plate theory, supported on Winkler elastic foundation with stiffness *k*,

$$D\nabla^4 w + \rho h \frac{\partial^2 w}{\partial t^2} + kw = q(x,t) \tag{1}$$

where D is the bending stiffness of the plate, h is the thickness, ρ is the mass density, and $q(x,y)$ is the distributed loading, and assuming free harmonic vibrations we have

$$D\nabla^4 w - \omega^2 \rho h w + kw = 0 \tag{2}$$

Now we rewrite this equation using two variants:

$$D\nabla^4 w - \bar{\omega}^2 w = 0 \tag{3}$$

or as

$$D\nabla^4 w + \bar{k} w = 0 \tag{4}$$

with $\bar{\omega}^2 = (\omega^2 \rho h - k)$ and $\bar{k} = (k - \omega^2 \rho h)$. The second representation resembles the static analysis of a plate on elastic foundation. The value of the generalized elastic parameter $\bar{k}$ can be positive or negative. In either case, one can solve the displacements of such a plate under a given concentrated load. This deflection will be infinite if the plate losses its stiffness, or in other words, the generalized foundation is causing the plate to be unstable.

Then, the solution for the vibration frequencies of the plate is equivalent to finding the values of the negative elastic foundation that will yield infinite deflection under a point load on the plate.

The solution for a clamped plate is decomposed to the sum of three cases of plates resting on elastic foundation as shown in Figure 1: solution for simply supported plate with a concentrated load, and two cases of distributed moments along opposite edges. Solution for simply supported plates with elastic foundation can be found using Navier's method. For clamped plates we use the superposition of three cases, and require that the slopes along the four edges will be zero.

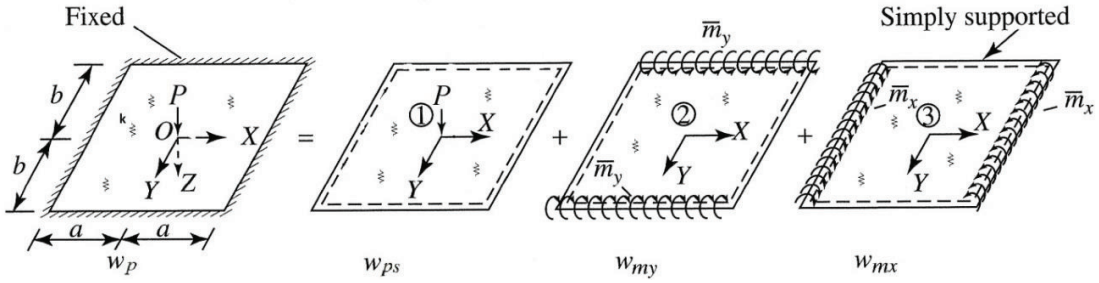

Figure 1: superposition of 3 cases

We plot the force P that will generate infinite deflection of the plate as a function of the value of ω. The vibration frequencies are found up to the desired accuracy by careful calculations at the neighborhood of the roots. In Table 1 the non-dimensional natural frequencies ($\bar{\omega} = \omega a^2 \left(\rho h / D\right)^{1/2}$) for three cases of square plates with clamped edges are given. The values are accurate up to the number of figures that is given.

Table 1: Non-dimensional natural frequencies for square plates

Mode	CCCC	CCCS	CSCS
1st	35.985160	31.826171	27.029892
2nd	73.393610	63.330661	60.481079
3rd	108.215486	71.076181	60.517721
4th	131.580768	100.791635	92.102184
5th	132.202316	130.350652	114.556338
6th	164.995778	151.891321	114.703554
7th	210.519508	159.474336	142.141247
8th	220.016524	189.765965	187.645084

For these frequencies we can draw the shapes of the vibration modes. These are given below in Figure 2 for the CCCC case.

Figure 2: Modes and frequencies for CCCC square plates

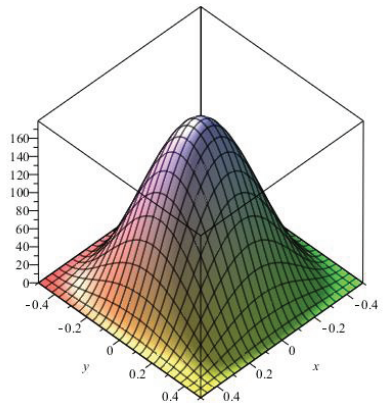		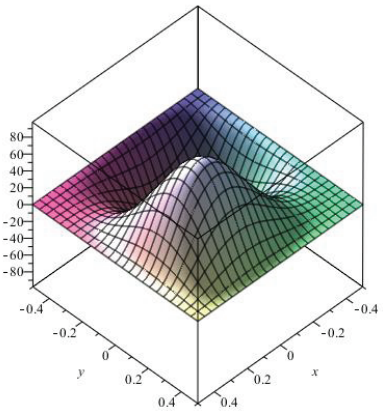	
Mode 1	$\omega_1 = 35.985160$	Mode 2	$\omega_2 = 73.393610$
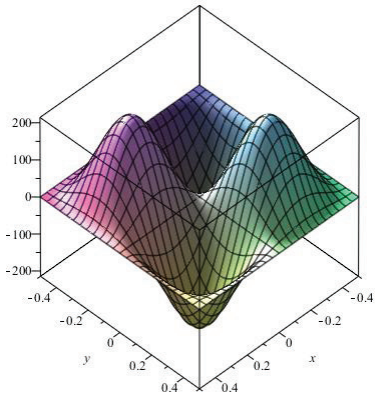		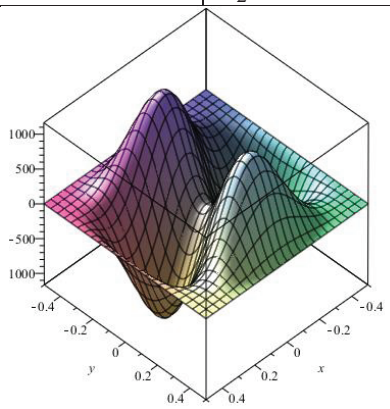	
Mode 3	$\omega_3 = 108.215486$	Mode 4	$\omega_4 = 131.580768$
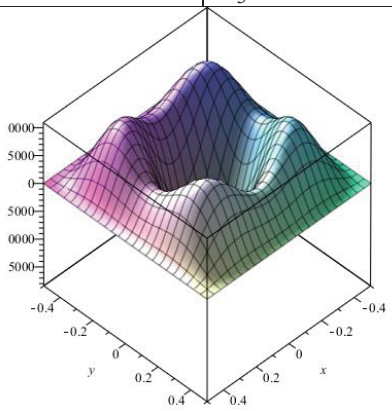		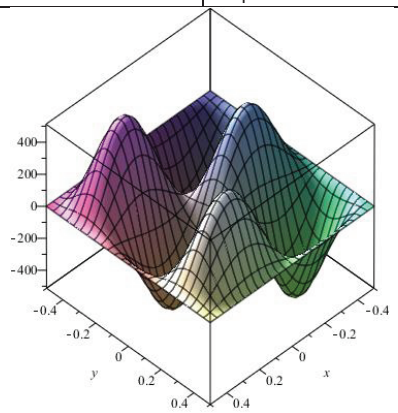	
Mode 5	$\omega_5 = 132.202316$	Mode 6	$\omega_6 = 164.995778$

References

1. A. Leissa, Vibration of Plates, Acoustical Society of America, 1993.

On the Accurate Estimation of Damping in Structural Elements

Mark Ewing, Aerospace Engineering, University of Kansas, Lawrence, KS
Himanshu Dande, ESI, Farmington Hills, MI

Knowledge of damping in structural elements is essential to an analyst attempting to predict response levels, whether amplitudes, maximum stresses or noise radiated. In the case of excitation at a fixed frequency, the task of estimating damping is rather easy, as one need only measure the amplitude of response at the locations of interest. But, to estimate damping over a wide frequency range, for instance for noise radiation, the job is more difficult.

Many have proposed techniques such as the Power Input Method [1], the Impulse Response Decay Method [1] and the Random Decrement Technique [2]. The authors have used PIM, IRDM and RDT to compare the damping estimations of a suite of flat, free-hanging panels with a range of 4 damping levels and for 3 different plate sizes. Both physical experiments and finite element analyses were used. The intent was to span the range of damping and panel sizes likely to be of interest in transportation vehicle construction. Damping was incorporated in the NASTRAN models as a frequency-independent damping matrix, proportional to the stiffness matrix. Damping loss factors of 0.01 and 0.1 were modeled and were, therefore, the "target" values of loss factor for the loss factor estimation schemes. For the plates tested physically, available constrained layer damping materials (viscoelastic films and thin aluminum cover sheets) were used to outfit two 48-inch by 34-inch aluminum plates, which were subsequently cut to provide smaller plates of the same aspect ratio. Estimates of the loss factors expected for these plates were based on the Ross-Kerwin-Ungar analysis [3] over the range of 500 to 4000 Hz as 0.048-0.077 and 0.09-0.127.

For all plates, the excitation was narrow-band random mechanical excitation at a point. For both experimental and analytical cases, the location of the excitation point was varied to determine the importance of this location to the estimation. Further, the effect of measurement location on the damping estimations was also studied. Exploration of the hypothesis that measurements "too close" to the excitation point would result in underestimations of damping level, as put forward by the authors [4], was the guiding concept for this study.

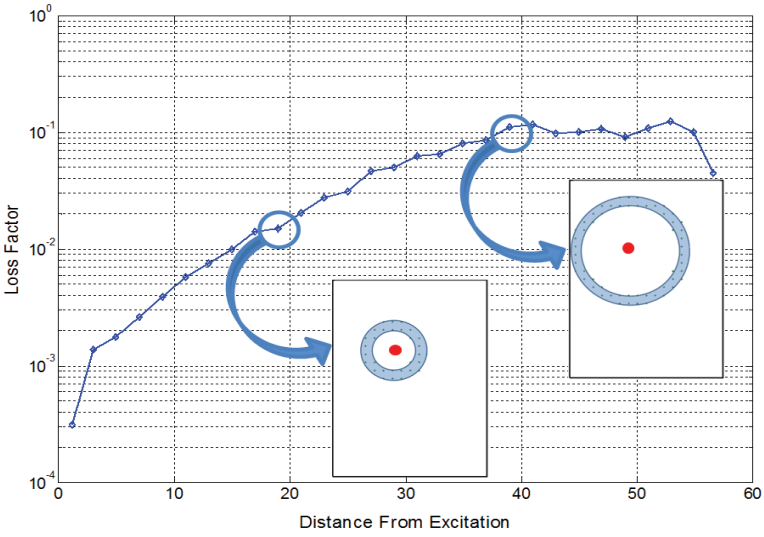

Figure 1. Loss factor estimates as a function of distance from the excitation point for measurements in a series of annular rings.

Response levels at many points (up to 6693) were considered. The damping estimation was then carried out considering the response from each point, individually. Then the ***average*** estimation from points lying within annular rings centered on the excitation point, as shown in Figure 1, were used to compute the loss factor as a function of distance from the excitation point. As expected, estimations near the excitation point were always an ***under***estimation in the finite element simulations. The same phenomenon

was also apparent in the experimental studies. That is, all estimations near the excitation point *did* produce a significantly lower loss factors than estimates further away.

One way of thinking about the "nearness" of response locations is to consider the "near field" and "far field" with respect to excitation at a point. The modal theory of vibration response is based on a reverberant field being established—far field. Lyon and DeJong [5] used an energy balance at steady state to define the radius of the direct field for a "very large" plate, r_D, as the distance from an excitation at which the kinetic energy density of the direct field equals that of the far field—inside the near field the energy density will be greater:

$$r_D = \frac{\omega \eta A_p}{2\pi \rho_s c_g}$$

Here, ω is the radial frequency, η is the damping loss factor, A_p is the plate area, ρ_s is the surface density and c_g is the group velocity. The variation of loss factor estimates with regard to the size of the direct field predicted by the "very large" plate assumption has been studied extensively and has shed light on the importance of the size of the direct field. The results of the computational studies showed that:

- PIM consistently underestimates, as expected
- IRDM underestimates for high damping, as expected, but is quite accurate for low damping
- RDT estimates bound the accurate solution
  ➔ one averaging scheme slightly underestimates, another slightly overestimates

The results of the experimental studies are given in Figure 2 on the following page. The results show that (compared with the average of RDT estimates):

- PIM overestimates at low frequencies—not expected—especially for lower damping levels
- IRDM underestimates consistently, as expected
- RDT estimates seem to bound the actual damping level

An overall observation, based on the computational studies, is that the average of the RDT estimates probably bound the actual loss factor. The fact that one averaging scheme overestimates and the other underestimates—using the same data—has been explained in terms of the processing scheme. Thus, the hypothesis that IRDM, being an input-output-based estimator, would always tend to underestimate appears to have been born out. But, this does not appear to be correct for PIM at the lower frequencies and damping levels, where overestimation occurs.

By definition, the loss factor is the ratio of the input energy to the total energy per cycle. For the many modes in a frequency band of excitation in which the excitation point is on or near a node line, any input force will result in a good bit of rigid body motion and little vibratory response, which is resonant or "magnified" response. As such, the recorded force will not result in much kinetic energy for the energy input, and the loss factor will be overestimated *systematically*. By further systematic studies, the hope is to reduce the estimation errors from +/1 one order of magnitude—the accepted standard in the industry a decade ago—to less than a factor of 2, which is where we are today.

References

1. Bloss, B. C. and Rao, M. D., *Estimation of Frequency–Averaged Loss Factors by the Power Injection and the Impulse Response Decay Methods*, JASA, Vol. 117(1), pp. 240–249, 2005.
2. Vandiver, J. K., Dunwoody, A. B., Campbell, R. B. and Cook, M. F., *A Mathematical Basis for the Random Decrement Vibration Signature Analysis Technique*, Journal of Mechanical Design, Vol. 144, pp. 307–313, 1982.

3. Ross, D., Ungar E. E., and Kerwin Jr., E. M., *Damping of Plate Flexural Vibrations by Means of Viscoelastic Laminae, in Structural Damping*, ed. By J. E. Ruzicka, ASME, NY, 1959, pp. 49-88.
4. Ewing, M. S., and Dande, H. A., *Effect of High Damping Levels on Loss Factor Estimation*, 8th International Symposium on Vibration of Continuous Systems, Whistler, BC, Canada, July 2011.
5. Lyon, R. H. and Dejong, R. G., *Theory and Application of Statistical Energy Analysis*, 2nd edition, RH Lyon Corp 1998.
6. Liu, W. B. and Ewing, M. S., *Experimental and Analytical Estimation of Loss Factors by the Power Input Method*, AIAA Journal, Vol. 45(2), pp. 477–484, 2007.

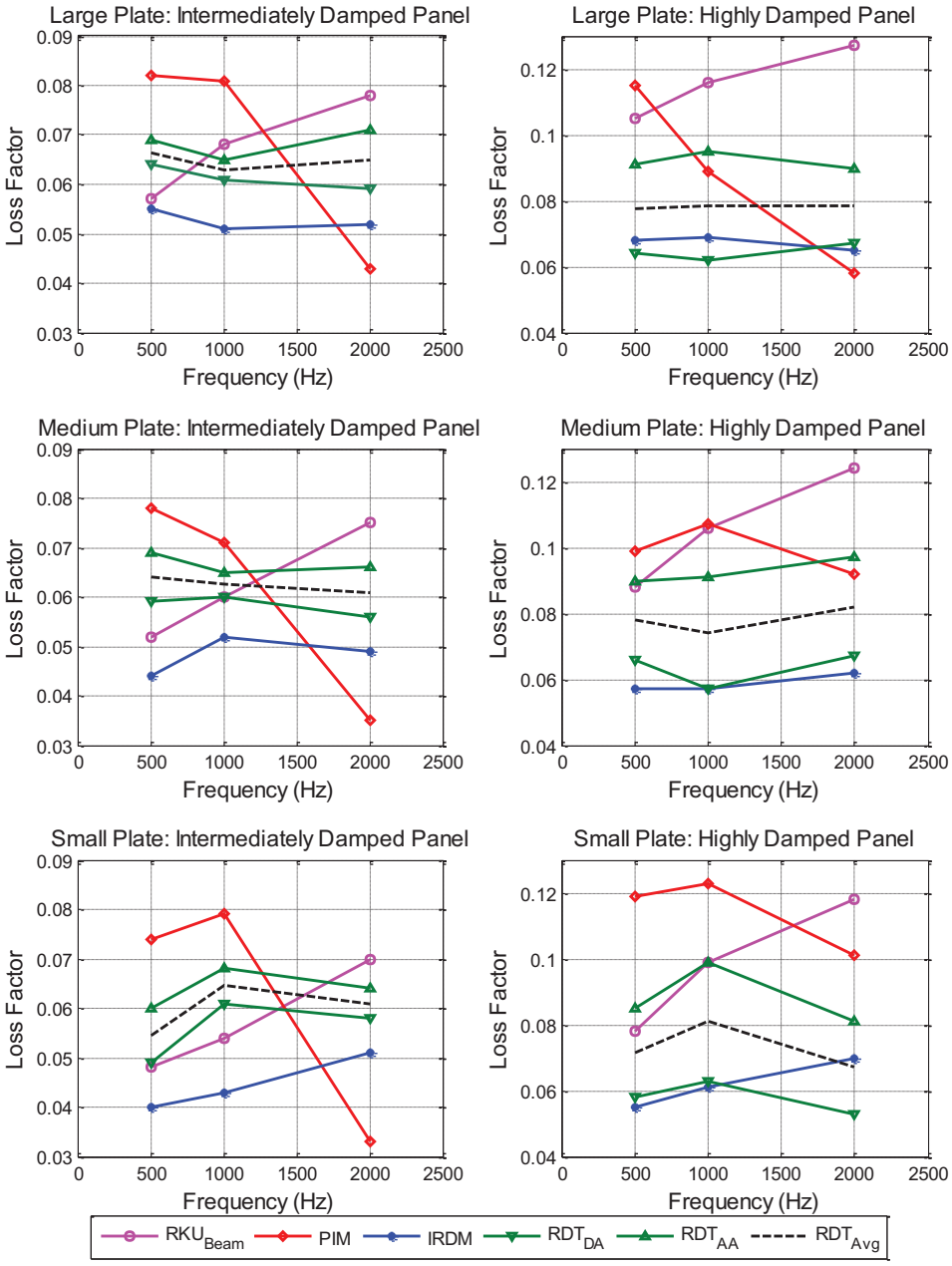

Figure 2. Average loss factors from experimental studies.

A Dynamic Stiffness Formulation for Free Vibration Analysis of Doubly-Curved Composite Shells Based on Higher Order Shear Deformation Theory

F. A. Fazzolari and J. R. Banerjee

City University London, Northampton square, London, EC1V 0HB, United Kingdom

1 Introduction

Thin-walled shell structures are widely exploited in aerospace applications and an accurate evaluation of their static, dynamic and aeroelastic behavior is essential to provide reliable data to design engineers. Doubly-curved laminated composite shells have been researched for many years because of the advantages to be gained from their high stiffness-to-weight and strength-to-weight ratios. Many theories have been developed and used to analyze doubly-curved shells such as those provided by Donnell [1], Mushtari [2], Love [3], Timoshenko [4] and Sanders [5] amongst others (see Leissa [6] for a comprehensive coverage). From the huge literature available on this subject only few attempts appear to have been made to solve the governing differential equations in an exact way in the scarcely available literature. By using the Donnell and Flügge assumptions Forsberg [7] solved free vibration of orthotropic circular cylindrical shells for simply supported (shear diaphragms) boundary condition. Although most of these attempts make use of considerable simplifications, these efforts are nevertheless necessary to compare and contrast with exact solution. The present work represents a significant contribution to the field by providing an exact solution procedure leading to the development of dynamic stiffness method (DSM), for free vibration analysis of laminated composite doubly-curved shells. The DSM researched by Banerjee for beam structures [8–10], is extended here, for the first time, to shell structures using a higher order shear deformation theory (HSDT). The global DS matrix of doubly-curved shell structures is developed as a major advancement of a recent work on composite plates [11]. Hamilton's principle is used to obtained the governing differential equations (GDEs) and boundary conditions (BCs). The GDEs are solved in an exact sense using symbolic computation and by exploiting the use of MATHEMATICA. The solution is implemented in a MATLAB® code. The Wittrick-Williams algorithm [12] has been used to compute the eigenvalues of the DS matrix. Inclusion of HSDT in the DSM framework will enable free vibration analysis of composite shells with moderate to high thickness to width ratio, in an accurate and computationally efficient manner. The usefulness of HSDT becomes apparent when analysing composite structures, particularly of thicker dimensions, because fiber reinforced composites have generally very low shear modulii. Extensive results which include validation and assessment of the effects of significant parameters such as the thickness-to-width (or length) ratio, radius-to-width ratio, number of layers, stacking sequence and boundary conditions, have been computed and discussed. The paper finishes with some concluding remarks.

2 Theoretical Formulation

In the derivation that follows, the hypotheses of straightness and normality of a transverse normal after deformation are assumed to be no longer valid for the displacement field which is now considered to be a cubic function in the thickness coordinate; and hence the use of higher

order shear deformation theory (HSDT). The laminate is assumed to be composed of N_l layers so that the theory is sufficiently general. The integer k is used as a superscript denoting the layer number where the numbering starts from the bottom. After imposing the transverse shear stress homogeneous conditions [13,14] at the top/bottom surface of the shell, the displacements field is given below in the usual form:

$$\begin{aligned} u(\alpha,\beta,z,t) &= \left(1+\frac{z}{R_\alpha}\right) u_0(\alpha,\beta,t) + z\,\phi_\alpha(\alpha,\beta,t) - z^3\,\frac{4}{3\,h^2}\left(\phi_\alpha(\alpha,\beta,t) + \frac{1}{\xi_1}\frac{\partial w_0(\alpha,\beta,t)}{\partial\alpha}\right) \\ v(\alpha,\beta,z,t) &= \left(1+\frac{z}{R_\beta}\right) v_0(\alpha,\beta,t) + z\,\phi_\beta(\alpha,\beta,t) - z^3\,\frac{4}{3\,h^2}\left(\phi_\beta(\alpha,\beta,t) + \frac{1}{\xi_2}\frac{\partial w_0(\alpha,\beta,t)}{\partial\beta}\right) \\ w(\alpha,\beta,z,t) &= w_0(\alpha,\beta,t) \end{aligned} \tag{1}$$

where u, v, w are general displacements within the shell in the α, β, and z directions, respectively, whereas u_0, v_0, w_0 are the corresponding displacements of the reference surface (mid-plane Ω), ϕ_α, ϕ_β are the rotations of the normals to the α, β, respectively, ξ_1, ξ_2 are the surface metrics and R_α and R_β are the radii of curvature in the α and β directions. A general procedure for the dynamic stiffness formulation of a structural element can be summarized as follows:

1. Obtain the differential equations of motion and the natural boundary conditions for the problem by applying Hamilton's principle.
2. Solve the differential equations in closed analytical form.
3. Apply general boundary condition for forces and displacements at the chosen nodes.
4. Eliminate the integration constants to relate the amplitudes of harmonically varying forces to the corresponding displacements.

The solution of the GDEs is sought in the following form:

$$\begin{aligned} u^0(\alpha,\beta,t) &= \sum_{m=1}^{\infty} U_m(\alpha)\,\mathrm{e}^{i\omega t}\sin(\hat{\theta}\,\beta), \qquad v^0(\alpha,\beta,t) = \sum_{m=1}^{\infty} V_m(\alpha)\,\mathrm{e}^{i\omega t}\cos(\hat{\theta}\,\beta), \\ w^0(\alpha,\beta,t) &= \sum_{m=1}^{\infty} W_m(\alpha)\,\mathrm{e}^{i\omega t}\sin(\hat{\theta}\,\beta), \qquad \phi_\alpha(\alpha,\beta,t) = \sum_{m=1}^{\infty} \Phi_{\alpha_m}(\alpha)\,\mathrm{e}^{i\omega t}\sin(\hat{\theta}\,\beta), \\ \phi_\beta(\alpha,\beta,t) &= \sum_{m=1}^{\infty} \Phi_{\beta_m}(\alpha)\,\mathrm{e}^{i\omega t}\cos(\hat{\theta}\,\beta) \end{aligned} \tag{2}$$

where ω is the unknown circular frequency, $\hat{\theta} = \frac{m\,\pi}{L}$ and $m = 1, 2, \ldots, \infty$. This is the so-called Lèvy's solution which assumes that two the opposite sides of the shell are simply supported (S-S), i.e. $w = \phi_\alpha = 0$ at $\beta = 0$ and $\beta = L$. Substituting Eq. (2) in the GDEs a set of ordinary differential equations (ODEs) is obtained which can be written in matrix forms as follows:

$$\begin{bmatrix} \mathcal{L}_{11} & \mathcal{L}_{12} & \mathcal{L}_{13} & \mathcal{L}_{14} & \mathcal{L}_{15} \\ \mathcal{L}_{21} & \mathcal{L}_{22} & \mathcal{L}_{23} & \mathcal{L}_{24} & \mathcal{L}_{25} \\ \mathcal{L}_{31} & \mathcal{L}_{32} & \mathcal{L}_{33} & \mathcal{L}_{34} & \mathcal{L}_{35} \\ \mathcal{L}_{41} & \mathcal{L}_{42} & \mathcal{L}_{43} & \mathcal{L}_{44} & \mathcal{L}_{45} \\ \mathcal{L}_{51} & \mathcal{L}_{52} & \mathcal{L}_{53} & \mathcal{L}_{54} & \mathcal{L}_{55} \end{bmatrix} \begin{bmatrix} U_m \\ V_m \\ W_m \\ \Phi_x \\ \Phi_y \end{bmatrix} = \begin{bmatrix} 0 \\ 0 \\ 0 \\ 0 \\ 0 \end{bmatrix} \tag{3}$$

where $\mathcal{L}_{ij}$ $(i,j=1,2,3,4,5)$ are differential operators [11]. The solution of the ODEs can thus be written as:

$$\begin{aligned} U_m(\alpha) &= \sum_{i=1}^{\mathcal{N}} A_i \ \mathrm{e}^{\mu_i \alpha} \qquad V_m(\alpha) = \sum_{i=1}^{\mathcal{N}} B_i \ \mathrm{e}^{\mu_i \alpha} \qquad W_m(\alpha) = \sum_{i=1}^{\mathcal{N}} C_i \ \mathrm{e}^{\mu_i \alpha} \\ \Phi_x(\alpha) &= \sum_{i=1}^{\mathcal{N}} D_i \ \mathrm{e}^{\mu_i \alpha} \qquad \Phi_y(\alpha) = \sum_{i=1}^{\mathcal{N}} E_i \ \mathrm{e}^{\mu_i \alpha} \end{aligned} \tag{4}$$

where A_i, B_i, C_i, D_i and E_i are integration constants and $\mathcal{N}$ is the degree of the auxiliary equation. The impositions of the boundary conditions to displacements and forces lead to the dynamic stiffness matrix, which can be finally written as:

$$\boldsymbol{F} = \boldsymbol{K}\,\boldsymbol{\delta} \tag{5}$$

where $\boldsymbol{F}$ is the forces amplitude vector, $\boldsymbol{K}$ is the DS matrix and $\boldsymbol{\delta}$ is the displacements amplitude vector. The assembly procedure in DSM is similar to that of the FEM. Once the global DS matrix of the structure is formed, the best way to solve the eigen-value problem to yield natural frequencies, is to apply the Wittrick and Williams algorithm [12]. The mode shapes are then routinely computed by using the global DS matrix. The investigation is currently underway. The results, discussions and conclusions will be reported in the full length paper

References

[1] L. H. Donnell. Stability of thin walled tubes under torsion. Technical Report 479, NACA, 1933.

[2] K. M. Mushtari. On the stability of cylindrical shells subjected to torsion, (in Russian). *Trudy Kazanskego aviatsionnugo inatituta, Vol. 2, 1938.*

[3] A. E. H. Love. *A treatise on the mathematical theory of elasticity.* Dover Pub., New York, 4^{th} edition, 1944.

[4] S. P. Timoshenko. *Theory of Plates and Shells.* McGraw Hill, New York, 1959.

[5] J. L. Sanders. An improved first approximation theory of thin shells. Technical Report R24, NASA, 1959.

[6] W. A. Leissa. Vibration of shells. Technical Report SP-288 (Scientific and technical information Office, Washington, DC), NASA, 1973.

[7] K. Folsberg. Influence of boundary conditions on the modal characteristics of thin cylindrical shells. *AIAA Journal*, 2(12):2150–2157, 1964.

[8] J. R. Banerjee. Coupled bending-torsional dynamic stiffness matrix for beam elements. *International Journal of Numerical Methods in Engineering*, 28:1283–1298, 1989.

[9] J. R. Banerjee. Dynamic stiffness formulation for structural elements: A general approach. *Computers & Structures*, 63(1):101–103, 1997.

[10] J. R. Banerjee. Free vibration analysis of a twisted beam using the dynamic stiffness method. *International Journal of Solids and Structures*, 38(38-39):6703–6722, 2001.

[11] F. A. Fazzolari, M. Boscolo, and J. R. Banerjee. An exact dynamic stiffness element using a higher order shear deformation theory for free vibration analysis of composite plate assemblies. *Composite Structures*, 96:262–278, 2013.

[12] W. H. Wittrick and F. W. Williams. A general algorithm for computing natural frequencies of elastic structures. *Quarterly Journal of Mechanics and Applied Mathematics*, 24(3):263–284, 1970.

[13] E. Carrera. On the use of transverse shear stress homogeneous and non-homogeneous conditions in third-order orthotropic plate theory. *Composite Structures*, 77:341–352, 2007.

[14] J. N. Reddy. *Mechanics of laminated composite plates and shells. Theory and Analysis.* CRC Press, 2^{nd} edition, 2004.

Forced Wave Dynamics of Laminate Anisotropic Composite Structures: an Analytically-Based Approach

Evgeny Glushkov and Natalia Glushkova
Institute for Mathematics, Mechanics and Informatics, Kuban State University
350040 Krasnodar, Russia, evg@math.kubsu.ru

Structural elements produced from laminate anisotropic composites possess more complicated mechanical properties than components manufactured from isotropic materials. Therefore, computer simulation of their elastodynamic response is a much more challenging task. In contemporary engineering practice, numerical methods based on spatial mesh discretization (FEM, finite differences, spectral elements, etc.) are considered as universal tools of computer simulation. These methods possess indisputable advantages, especially when applied to structures with complex geometries and/or material properties. However, these methods do not work well for elongated structures or in high-frequency applications, since the discretization requires a larger number of elements as distances or frequencies increase. Moreover, mesh-based solutions cannot offer the same physically clear descriptions of wave processes that analytical guided wave (GW) representations provide.

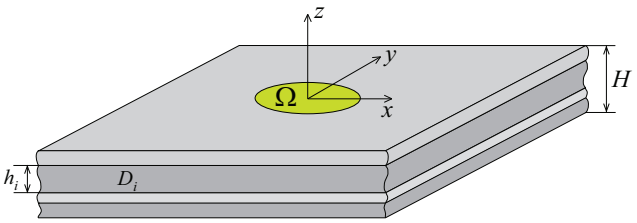

Figure 1: Geometry of problem.

We would like to draw attention to an analytically-based approach; a more detailed description may be found in Refs [1, 2] and papers cited therein. The approach is based on the use of integral and asymptotic representations for the response displacement vector $\mathbf{u} = (u_x, u_y, u_z) = (u_1, u_2, u_3)$. They are derived via the convolution of the Green's matrix of the structure $k(\mathbf{x})$, $\mathbf{x} = (x, y, z)$, with the vector of a time-harmonic loading $\mathbf{q}(x, y)e^{-i\omega t}$. Alternatively, it may be written in terms of their Fourier symbols $K = \mathcal{F}_{xy}[k]$ and $\mathbf{Q} = \mathcal{F}_{xy}[\mathbf{q}]$:

$$\mathbf{u}(\mathbf{x}) = \mathcal{F}_{xy}^{-1}[K\mathbf{Q}] = \frac{1}{4\pi^2}\int\limits_{\Gamma_1}\int\limits_{\Gamma_2} K(\alpha_1, \alpha_2, z)\mathbf{Q}(\alpha_1, \alpha_2)e^{-i(\alpha_1 x+\alpha_2 y)}d\alpha_1 d\alpha_2. \tag{1}$$

Here $\mathcal{F}_{xy}$ is the operator of the integral Fourier transform with respect to the horizontal coordinates x and y (Fig. 1); the integration contours Γ_1 and Γ_2 go along the real axes, deviating from them into the complex planes α_1 and α_2 for rounding real poles of the matrix K elements; Ω is a local area at the plate's top surface $z = 0$, to where the load $\mathbf{q}$ is applied; the factor $e^{-i\omega t}$ is conventionally omitted. The column vectors $\mathbf{k}_j$ of the Green's matrix $k = (\mathbf{k}_1 \vdots \mathbf{k}_2 \vdots \mathbf{k}_3)$ are displacements excited by concentrated point loads applied to the surface $z = 0$ along the basic coordinate vectors $\mathbf{i}_j$, $j = 1, 2, 3$.

Expression (1) provides explicit solution to the 3D boundary value problem for a laminated structure with elastodynamic equations

$$C_{ijkl}u_{l,jk} + \rho\omega^2 u_i = 0, \quad i = 1, 2, 3 \tag{2}$$

given in the subdomains $D_m : |x| < \infty, |y| < \infty, z_{m+1} \le z \le z_m$ of the M-layer domain $D = \cup_{m=1}^{M} D_m$: $|x| < \infty, |y| < \infty, -H \le z \le 0$ (Fig. 1). The elastic stiffness tensor C_{ijkl} and the density ρ remain constant within sublayers D_m; the outer boundaries $z = 0$ and $z = -H$ are stress-free except for the loading area Ω; the sublayers are perfectly bonded.

Although the domain D is infinite, the integral and asymptotic solutions, as well as similar ones for the internal forces, can be efficiently used with finite structural elements too. In hybrid schemes, by combining such solutions with mesh or boundary element discretization of local areas (flaws, stringers, rivets), they provide low-cost continuation to the rest of the structure. Another method is to use solutions with unknown (fictitious) loads and/or body forces as special laminate elements (LEs) meant for the approximation of reflected and scattered waves. Unlike classical boundary elements, the LEs automatically satisfies not only the governing equations but in addition all the boundary conditions at the plane-parallel sides and interfaces so that only conditions at local obstacles and plate edges need to be approximated with LEs.

Efficient computational implementation of the derived solutions becomes possible with fast and reliable matrix K calculation algorithms described in papers [1, 2], which, in fact, are kinds of transfer matrix algorithms [3, 4]. Inside Ω and in its vicinity, the response $\mathbf{u}$ can be obtained by means of direct numerical integration. With elongated structures the response manifests itself as GWs propagating from the loading area Ω, re-radiated by local inhomogeneities and reflected from the sample's edges. In 3D structures, the GWs are quasi-cylindrical waves spreading out from actuators and scatterers. In the isotropic case, representations for such GWs can be obtained in a closed analytical form as residues from real poles ζ_n of the matrix K elements. These poles ζ_n, coinciding with the roots of the modal characteristic equation, play the role of GW wavenumbers; they indirectly specify their phase and group velocities $c_n = \omega/\zeta_n$ and $v_n = d\omega/d\zeta_n$.

However, with anisotropic composites, two-fold integrals (1) are generally irreducible to one-fold ones, and the residue technique does not yield closed GW representations. As a compromise, it was proposed to use the residue technique for one of them with numerical integration of the remaining one [5]. As an alternative, an approximation of a 3D quasi-cylindrical GW radiation by a superposition of 2D plane waves has been also implemented [6]. At the same time, closed-form representations for cylindrical GWs excited in anisotropic plates by localized sources or scattered by local obstacles were already derived as far back as in the 1980-90s, but in English we presented them just recently, in papers [1, 2]. By combining the residual technique with the stationary phase method, they have been obtained in the form

$$\mathbf{u}(\mathbf{x}) = \sum_{n=1}^{N_r} \sum_{j=1}^{N_j} \mathbf{a}_{nj}(\varphi, z) e^{is_{nj}r} / \sqrt{\zeta_{nj} r}, \quad \zeta_{nj} r \to \infty. \tag{3}$$

Here $\mathbf{a}_{nj} = i\sqrt{i\zeta_{nj}/(2\pi s_n''(\gamma_j)}\, \operatorname{res} K(\alpha, \theta_j, z)|_{\alpha=\zeta_{nj}} \mathbf{Q}(-s_{nj}, \varphi)\zeta_{nj}$, $s_{nj} = \zeta_{nj} \sin\gamma_j$, $\zeta_{nj} = \zeta_n(\theta_j)$, $\theta_j = \gamma_j + \varphi + \pi/2$; $\zeta_n = \zeta_n(\gamma)$ are angular dependent poles of matrix K elements with respect to the polar coordinate $\alpha = \sqrt{\alpha_1^2 + \alpha_2^2}$ in the wavenumber plane (α_1, α_2): $\alpha_1 = \alpha\cos\gamma$, $\alpha_2 = \alpha\sin\gamma$; γ_j are stationary points, i.e., the roots of equations $s_n'(\gamma) = (\zeta_n(\gamma)\sin\gamma)' = 0$; N_j are the numbers of these roots; N_r is a number of real poles ζ_n at a frequency ω considered. With isotropic plates, ζ_n are independent of γ, $N_j = 1$, $\gamma_1 = \pi/2$, $s_{nj} = \zeta_n$. From these simplifications, quasi-cylindrical GWs, specified by every term of expansion (3), turn into known cylindrical

GWs generated in isotropic waveguides by a local source. In the anisotropic case, the angular dependence of the wavenumbers s_{nj} results in the dependence of phase and group velocities $c_{nj} = \omega/s_{nj}$ and $v_{nj} = d\omega/ds_{nj}$ on the direction of propagation φ. It was experimentally confirmed that the dispersion dependencies $s_{nj}(\omega)$ are what determine the group velocities v_{nj} and not the roots $\zeta_n(\omega)$ as one could decide by analogy with the isotropic case.

The derived representations have been computer implemented and experimentally verified against the data acquired by means of laser vibrometry of piezowafer actuated surface waves [7, 8]. The measurements were carried out in cooperation with Prof. R. Lammering from Helmut-Schmidt University, Hamburg, in the course of visits of Dr. A. Eremin to his Institute. The abilities of the approach are illustrated by several examples of its application, such as an investigation into frequency dependent GW directivity [2, 7], reconstruction of effective material constants of composite plates, and tuning of actuators' central frequencies with accounting for material anisotropy [8].

This work is partly supported by the Russian Foundation for Basic Research, project No 12-01-00320.

References

[1] Ye.V. Glushkov, N.V. Glushkova, and A.S. Krivonos, The excitation and propagation of elastic waves in multilayered anisotropic composites, Journal of Applied Mathematics and Mechanics. V. 74. P. 297-305 (2010).

[2] E. Glushkov, N. Glushkova, and A. Eremin, Forced wave propagation and energy distribution in anisotropic laminate composites, J. Acoust. Soc. Am., **129**(5), 2923-2934 (2011).

[3] A. H. Nayfeh, The general problem of elastic wave propagation in multilayered anisotropic media, J. Acoust. Soc. Am. **89**(4), 15211531 (1991).

[4] J. J. Ditri and J. L. Rose, Excitation of guided waves in generally anisotropic layers using finite sources, J. Appl. Mech. **61**, 330338 (1994).

[5] S. Banerjee, W. Prosser, A. Mal, Calculation of the response of a composite plate to localized dynamic surface loads using a new wave number integral method, Journal of Applied Mechanics, **72**(1), 18–24 (2005).

[6] A. Velichko, P.D. Wilcox, Modeling the excitation of guided waves in generally anisotropic multilayered media, J. Acoust. Soc. Am., **121**(1), 60–69 (2007).

[7] E. Glushkov, N. Glushkova, A. Eremin, R. Lammering, and M. Neumann, Frequency dependent directivity of guided waves excited by circular transducers in anisotropic composite plates, J. Acoust. Soc. Am. **132**(2), EL119-EL124 (2012).

[8] E. Glushkov, N. Glushkova, and A. Eremin, Efficient mathematical representations for computing the forced wave dynamics of anisotropic laminated composites, CEAS Aeronautical Journal, published online 14 Feb. 2013, doi 10.1007/s13272-013-0064-1.

Optimum Design and Experimental Evaluation for Smart Micro-composites by Using Laser Excitation Technique

Shinya HONDA*[1], Kazuki WATANABE*[2], Yoshihiro NARITA*[3] and Itsuro KAJIWARA*[4]

*[1] Corresponding Author, Faculty of Engineering, Hokkaido University,
N13W8, Kita-ku, Sapporo, Hokkaido, 060-8628, Japan, honda@eng.hokudai.ac.jp
*[2] Graduate School of Engineering, Hokkaido University, watanabe_kazuki@frontier.hokudai.ac.jp
*[3] Hokkaido University, ynarita@eng.hokudai.ac.jp
*[4] Hokkaido University, ikajiwara@eng.hokudai.ac.jp

1. Introduction

Use of micro-devices has become more common in various electrical appliances and mechanical systems. As the performance of those applications is demanding, more advanced mechanical properties are required for the micro-device. An effective technique of vibration suppression is essential for improvement of device performance. The smart structure with piezoelectric (PZT) actuators and sensors is a promising solution for such vibration suppression of micro-devices. Among the types of smart structures, smart composites consisting of laminated fibrous composites, graphite/epoxy (CFRP) materials, are employed here. Adding to their high specific stiffness and strength, the CFRP material has an anisotropic property which can be design. An influence of anisotropy becomes distinguished for the micro-sized structure, and consideration of the anisotropy in the design of smart micro-composite is more important than the macro-sized structures. An efficient use of strong anisotropy of fibrous composite makes it possible to design task specific smart micro-devices, resulting in the improvement of micro-mechanical systems.

2. Optimum design of smart composites

The present study assumes a smart micro-composite as an application to the hard disk drive (HDD) head driver. Figure 1 shows (A) commercial HDD head driver and (B) the present smart micro-composite used in this study. Carbon fiber pre-pregs are used to fabricate the composite, and it has symmetric 6-layers.

Finite element analysis (FEA) is used to model the smart structures and to design a controller for the closed-loop system. The actuator has 0.5 mm in thickness and 2.0 mm in width (Fig. 1(B)) but its mass and stiffness effects are neglected in the modelling since it is possible to assume the actuator is thin and light enough as compared to CFRP plate. The actuator is thus assumed as a segment of line in the controller design problem, and its end points are used as input points of control forces which are loaded in rotational degree-of-freedom.

A multidisciplinary design optimization technique for smart composite structures is presented to enhance the performance of the closed-loop system. Laminated composite plates are formed by thin orthotropic layers (i.e., pre-pregs) and the vibration characteristics depend on the lay-up configuration. At the same time, the vibration control performance depends strongly on the actuator placement and the designed controller. The simultaneous optimization of the lay-up of composite and the placements of actuators will involve high control performances.

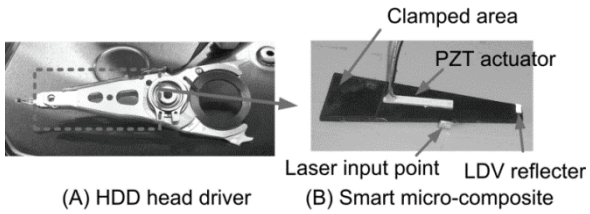

Fig. 1 Commercial HDD head driver and the present micro composite.

The optimization problem is described to achieve the above purpose by

$$\begin{aligned} &\text{Minimizing}: \quad H_{z1} \\ &\text{Subject to}: \quad H_u \le H_u^{\max} \end{aligned} \tag{1}$$

The control problem is defined to reduce the H_∞ norm with respect to the controlled response H_{z1}, under the constraint of the H_∞ norm with respect to the control input H_u. The design variables include the lay-up indexes η_L to represent the lay-up configuration $[\theta_1/\theta_2/\theta_3]$s and the actuator placements η_{AC}. As an optimizer, a simple genetic algorithm (SGA) is employed with a two-point crossover, mutation and elitist tactics.

The present optimization process is configured to follow a three-step procedure [1].

[Step 1] The database containing natural frequencies and modal matrixes for all possible lay-up configurations is prepared by repeated application of the FEA.

[Step 2] Assuming the state feedback, the simultaneous optimization for the lay-up configuration and the PZT actuator placement is performed by the SGA.

[Step 3] Reconstructing the output feedback system with the dynamic compensator $K(s)$ based on the Linear Matrix Inequality (LMI) approach.

3. Experimental method

The present experimental setup is shown in Fig. 2. There is a difficulty in exciting the micro-device experimentally by an impulse hammer or external exciter due to limitations on size and their high natural frequencies. The present paper employs an innovative vibration testing method for the smart micro-structures using an impulse excitation invoked by a laser ablation [2]. A pulse laser irradiated by a high power yttrium aluminium garnet (YAG) laser device ablates quite small mass of the surface instantly and this generates an ideal impulse force to the structure. Further, the laser ablation excites structures without physical contacts, resulting in high reproducibility since the laser beam can be irradiated precisely at the same point of structure with the pre-set same power. The velocity response is also measured by the laser Doppler vibrometer (LDV).

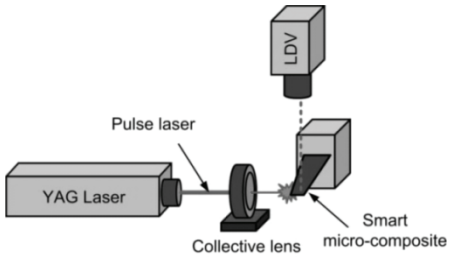

Fig. 2 Experimental setup of the present vibration control system.

Table 1 Suppression amount of magnitude for the first peak. (experimental results)

Suppression amount [db]	[-15/-15/-15]s (Opt.)	[0/0/0]s (Unidirectional)	[0/90/0]s (Cross-ply)	[45/-45/45]s (Angle-ply)
Measured	-15.28	-13.68	-12.36	-3.98
Calculated	-16.30	-6.60	-8.66	-0.65

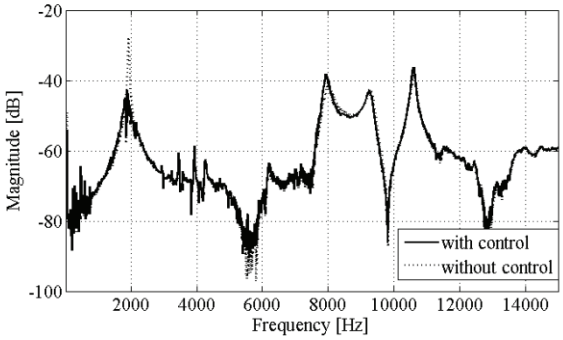

(i) Measured power spectrum of velocity

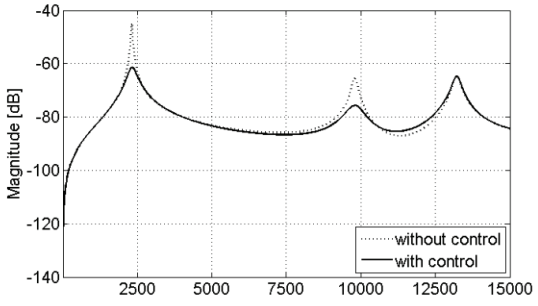

(ii) Calculated FRF of velocity

Fig. 3 (i) Measured power spectrum and (ii) Calculated FRF of velocity for the obtained optimum smart composite [-15/-15/-15]s.

4. Numerical and experimental results

Table 1 indicates reduction amounts of the fundamental frequency in the dB scale obtained by the numerical calculation and experiment. Results of plates with typical lay-ups are also listed in Table 1 for comparison, where comparative plates have fixed lay-ups but optimum actuator placements calculated by the similar procedure with the present method. The suppression amounts are calculated by using the frequency response function (FRF) for numerical calculation and the power spectrum of velocity for the experiment, and both values cannot be compared directly. Figure 3 shows the power spectrum and FRF for the optimum results by the experiment and calculation, respectively.

Although there are some differences between calculated and measured results in Fig. 3, both sets of results show similar tendency in the performance of vibration suppression in Table 1. The optimum plate shows the largest reduction and the angle-ply plate does the lowest. Therefore, it could be concluded that the present optimization method is effective for smart micro-composite and the laser ablation technique works well as the excitation method for the micro-sized structures.

Reference

[1] Honda, S., Kajiwara, I., and Narita, Y., 2011. “Multidisciplinary design optimization for vibration control of smart laminated composite structures”, Journal of Intelligent Material Systems and Structures, 22(13), pp. 1419-1430.

[2] Hosyoya, N. and Kajiwra, I, and Hosokawa, T., 2012, “Vibration testing based on impulse response excited by pulsed-laser ablation: Measurement of frequency response function with detection-free input”, Journal of Sound and Vibration, 331(6), pp. 1355-1365.

Exact natural frequencies of multi-level elastically connected taut strings and related problems

W.P. Howson[1] and A. Watson[2]

[1] Cardiff School of Engineering, Cardiff University, UK

[2] Department of Aeronautical and Automotive Engineering, Loughborough University, UK

Introduction The dynamics of a family of simple, but extremely useful structural elements is governed by a second order Sturm-Liouville equation. This equation allows for the uniform distribution of mass and stiffness and enables the motion of strings and shear beams, together with the axial and torsional motion of bars to be described exactly. As a result, each member type in this family has been treated exhaustively when considered as a single member or when joined contiguously to others. However, when such members are linked in parallel by uniformly distributed elastic interfaces, their complexity becomes significantly more intractable and it is this class of structures that has led to renewed interest and which forms the basis of the work that follows.

Initially, differential equations governing the coupled motion of the system are developed from first principles. These are organised into the form of a generalised linear symmetric eigenvalue problem, from which a family of uncoupled differential operators can be established. These operators define a series of exact substitute systems that together describe the complete motion of the original structure. These equations can then be used in either of two ways. In their most powerful form they can be developed into exact dynamic stiffness matrices that enable all the powerful features of the finite element method to be utilised. This subsequently enables sets of members carrying point masses and subject to point spring supports to be analysed easily. Alternatively, the equations are able to yield an exact relational model that links any uncoupled frequency of an original member to the corresponding set of coupled system frequencies. This approach enables 'back of the envelope calculations' to be undertaken quickly and efficiently. The exact mode shapes of the original structure can be recovered in either case. Due to space limitations, only aspects of the first technique are described briefly herein, but both are covered exhaustively elsewhere [1].

Theory The theory below has been developed for an easily envisioned set of taut string members that are connected to each other by elastic interfaces of unequal stiffness, with the top (i = 1) and bottom ($i = n$) members being additionally connected to foundations. However, the approach applies equally to all the member types previously mentioned. Thus, adopting the assumptions of classical string theory, limiting attention to free vibration and introducing the non-dimensional length parameter, $\xi = x/L$, the equation of motion for a typical elemental length of string, i, and its corresponding constitutive relationship are easily shown to be

$$k_i V_{i-1} - (k_i + k_{i+1})V_i + k_{i+1}V_{i+1} + r_i(D^2 + \gamma_i\omega^2)V_i = 0 \quad \text{and} \quad Q_i = r_i L\, dV_i/d\xi \tag{1a,b}$$

where k_i and k_{i+1} are the stiffness / unit length of the elastic interfaces connecting adjacent strings or foundations and V_i and Q_i are the amplitudes of the lateral displacement and vertical component of string tension, respectively, $D^2 = d^2/d\xi^2$, $r_i = T_i/L^2$, $\gamma_i = m_i/r_i$, m_i is the mass / unit length, L is the length of all members comprising the set and ω is the circular frequency. It is now assumed that m_i/T_i is constant for all i and hence that

$$\gamma_i = \gamma = mL^2/T = \text{constant} \tag{2}$$

This enables the governing equations for the first, last and typical members to be written, respectively, as

$$(k_1 + k_2)V_1 - k_2V_2 - r_1\lambda V_1 = 0\,, \qquad -k_nV_{n-1} + (k_n + k_{n+1})V_n - r_n\lambda V_n = 0 \tag{3a,b}$$

and

$$-k_iV_{i-1} + (k_i + k_{i+1})V_i - k_{i+1}V_{i+1} - r_i\lambda V_i = 0 \tag{3c}$$

where

$$\lambda = D^2 + \gamma\omega^2 \tag{4}$$

and k_1 and k_{n+1} can be zero or non-zero in any combination, thus defining the longitudinal boundary conditions.

Eqs.(3) enable a complete set of equations to be assembled for an *n* level system, as indicated by Eq.(5a)

$$\left\{\begin{bmatrix} k_1+k_2 & -k_2 & & & \\ & \bullet & & & \\ & -k_i & k_i+k_{i+1} & -k_{i+1} & \\ & & & \bullet & \\ & & & -k_n & k_n+k_{n+1} \end{bmatrix} - \lambda \begin{bmatrix} r_1 & & & & \\ & \bullet & & & \\ & & r_i & & \\ & & & \bullet & \\ & & & & r_n \end{bmatrix}\right\} \begin{bmatrix} V_1 \\ \bullet \\ V_i \\ \bullet \\ V_n \end{bmatrix} = \begin{bmatrix} 0 \\ \bullet \\ 0 \\ \bullet \\ 0 \end{bmatrix} \tag{5a}$$

where zeros have been omitted for clarity. Eq.(5a) can then be written concisely as

$$(\mathbf{k} - \lambda\,\mathbf{r})\mathbf{V} = \mathbf{0} \tag{5b}$$

The form of Eqs.(5) is that of a generalized symmetric linear eigenvalue problem, for which a number of standard routines are available for calculating the eigenvalues, λ, and corresponding modal vectors, $\mathbf{V}$.

Substitute systems The *n* values of λ that satisfy Eqs.(5) define a family of second order differential operators that satisfy the original problem and which are given by Eq.(4) as

$$D^2 + \gamma\omega^2 = \lambda_i \qquad i = 1,2,\ldots\ldots n \tag{6}$$

Eq.(6) can be assigned a physical context by noting that it is a property of such differential operators that they can be written as

$$(D^2 + \gamma\omega^2)V_i = \lambda_i V_i \qquad i = 1,2,\ldots n \tag{7}$$

and hence that

$$(D^2 + \chi_i^2)V_i = 0 \qquad i = 1,2,\ldots n \tag{8}$$

where

$$\chi_i^2 = \gamma\omega^2 - \lambda_i \tag{9}$$

and V_i is a typical lateral displacement amplitude. In this case, each equation now describes the free vibration of a single unified member, but supported on a Winkler foundation of different magnitude in each case. Eqs.(8) therefore represent *n* substitute systems, each of which yield an infinite number of frequencies that, when arranged in ascending order, comprise the complete spectrum of frequencies of the original problem. It therefore follows that the fundamental frequency of the original problem is given by the single substitute system that yields the lowest frequency, namely the one that incorporates the lowest linear eigenvalue derived from Eqs.(5).

An exact stiffness formulation (exact finite element) is now adopted to solve the i^{th} substitute system and can be expressed as

$$\begin{bmatrix} Q_{i0} \\ Q_{i1} \end{bmatrix} = r_i L \frac{\chi_i}{S_i} \begin{bmatrix} C_i & -1 \\ -1 & C_i \end{bmatrix} \begin{bmatrix} V_{i0} \\ V_{i1} \end{bmatrix} \tag{10}$$

where

$$C_i = \cos \chi_i \text{ and } S_i = \sin \chi_i \text{ for } \chi_i^2 > 0 \text{ and } C_i = \cosh \chi_i \text{ and } S_i = \sinh \chi_i \text{ for } \chi_i^2 < 0 \qquad (11a,b)$$

and the subscripts 0 and 1 relate to the left and right hand end of the unified member, respectively.

Identical boundary conditions are now imposed on each substitute system in turn by adding spring supports and/or nodal masses at both $\xi = 0$ and $\xi = 1$. There is no requirement for the masses to be the same at each end and the stiffnesses can be assigned any value between zero (free support) and $+\infty$ (clamped support). The required natural frequencies stemming from each of the *n* substitute systems can then be converged upon to any desired accuracy using the Wittrick-Williams algorithm. All the frequencies thus calculated are natural frequencies of the original system and can be arranged in ascending order to cover any frequency range of interest, which will be guaranteed to be fully populated if the highest frequency is bounded above in each of the substitute systems.

Example Consider now the problem of two identical and parallel taut strings of length 1 m that are linked by an elastic interface of stiffness k = 200 N/m^2. The mass/unit length and string tension for both members are 0.01 kg/m and 50 N, respectively. The results are presented in Table 2, where they are compared with those of Oniszczuk [2]. It is interesting to note that in this example the natural frequencies corresponding to anti-symmetric modes are identical to the uncoupled frequencies of the two members, since both members move identically in the same direction and do not extend the massless elastic interface that connects them. Hence $\lambda_1 = 0.0$.

Table 2 Comparison between the natural frequencies given by Oniszczuk [2] and the presented theory for the parallel string problem described above. The frequencies correspond to either A/S (Anti-Symmetric) or S (Symmetric) modes about the horizontal axis of symmetry. * This value has been confirmed as a typing error in the original paper and should be 222.1.

Modal No.	Natural frequencies (rad/sec)			
	[2]		Presented theory	
	A/S	S	Substitute system 1 $\lambda_1 = 0.0$	Substitute system 2 $\lambda_2 = 8.0$
1	221.1*	298.9	222.144	298.911
2	444.3	487.2	444.288	487.229
3	666.4	695.8	666.432	695.796
4	888.6	910.8	888.577	910.806
5	1110.7	1128.6	1110.72	1128.58
6	1332.9	1347.8	1332.86	1347.80

References

[1] Howson, WP, Watson, A and Rafezy, B. Free vibration of multi-level elastically connected members: A simple method for exact solutions. *Int. J. Solids Structs*. (Under review)

[2] Oniszczuk, Z. Transverse vibrations of elastically connected double-string complex system, Part II: Forced vibrations. *J. Sound Vib*. (2000) 232, 367-386.

Modelling voids using embedded negative structures – the story of the spurious modes

S. Ilanko[1], Y. Mochida[1], P. Hagedorn[2], A. Wagner[2] and D. Kennedy[3]

[1]The School of Engineering, The University of Waikato, New Zealand

[2]The Technical University of Darmstadt, Germany

[3]Cardiff School of Engineering, U.K.

Spurious Modes

The idea of modelling a solid with holes or cut-outs by embedding negative bodies was mooted in a previous symposium [1]. This concept emerged following the successful use of negative stiffness and negative mass in modelling constraints in vibration analysis [2,3]. In constraint modelling, it was found that the use of large magnitudes of either stiffness or inertial type penalty parameters effectively created a constraint, irrespective of the sign of the penalty parameter. The use of positive and negative values helped to determine and control the error due to constraint violation. Although triggered by the above mentioned developments, the use of negative structures, i.e. structures possessing both negative stiffness and negative mass, for the purpose of modelling voids, is actually a different concept. An attempt to test this procedure by removing a cantilever beam segment in a longer cantilever beam by embedding a negative cantilever beam produced natural frequencies and modes of the remaining free-free beam. However, there were also extra spurious modes, some of which could not be explained. The embedding was achieved by using a continuous distribution of penalty terms. Further studies show that the extra spurious modes fall into two different categories and could be identified by their shape. One type is associated with violation of the embedding constraints thus permitting the embedded negative parts and the associated positive part to have differential displacements. An example of this type of spurious modes is given in Figure 1. The figure shows a completely free square plate on which a negative free plate is embedded at the centre. As can be seen from the figure, the negative part, (the smaller plate at the centre) vibrates differently from the positive part. This type of spurious mode seems to occur at high frequencies. There is another type of spurious modes where the embedded negative part and the associated positive part move together without any violation of the constraint, but the remainder of the structure remains stationary. Figure 2 shows an example of this type of spurious mode. In this mode, only the domain in which the negative part is attached vibrates and there is no discrepancy between the displacement of the positive and negative parts. This is understandable since the positive and negative parts completely cancel each other, so they do not

result in any net forces or moments that need to be transferred to the remaining structure, which therefore does not participate in vibration. However, some of the modes in this category showed an anomaly in discrete systems where degrees of freedom that were connected to the actual structure had some displacement while the rest of the structure was stationary. This caused some initial concern as it implied that some force would have to be induced at the boundaries, in which case the lack of any motion of the remaining structure would indicate violation of Newton's law. However, it was noted that these occurred at very high frequencies which in the limiting case would approach infinity, thus while the displacement may approach zero the accelerations may be finite and be consistent with the boundary force.

There are still some additional spurious modes for which it is difficult to make a classification as described above [l]. This may be due to large round off errors and work is still in progress to understand those extra modes.

Elimination of spurious modes:

One possibility to distinguish at least some spurious modes from desired, original modes of the structure under consideration is to set the density of the negative structure not to the exact counterpart of the positive one. Instead, the absolute value of the density of the negative structure can be set to be slightly lower than that of the positive one leading to small residual portions of mass. Since the stiffness properties are cancelled completely, this leads to spurious modes with very low natural frequencies, which can be eliminated as desired. This technique is especially suitable for assembled structures whose first natural frequency is known to be higher than a certain value, e.g. brake discs with inserted holes, whose first actual frequency will at least be an order of magnitude higher than the frequencies of the spurious modes [4,5].

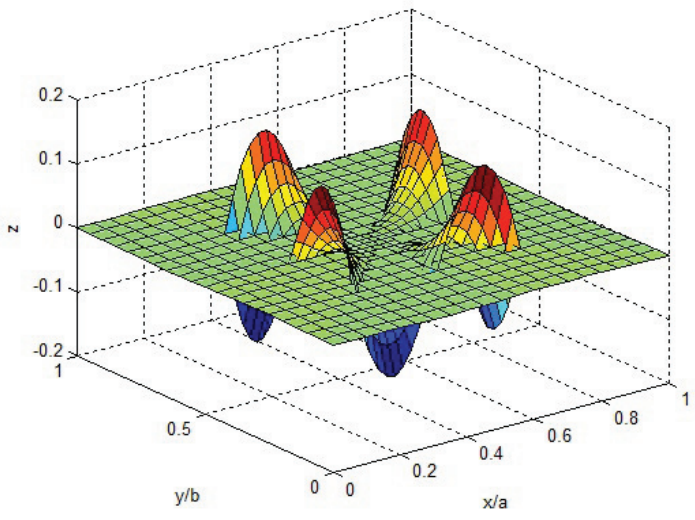

Figure 1. An example of a spurious mode for which there is a violation of constraints between the positive and negative parts.

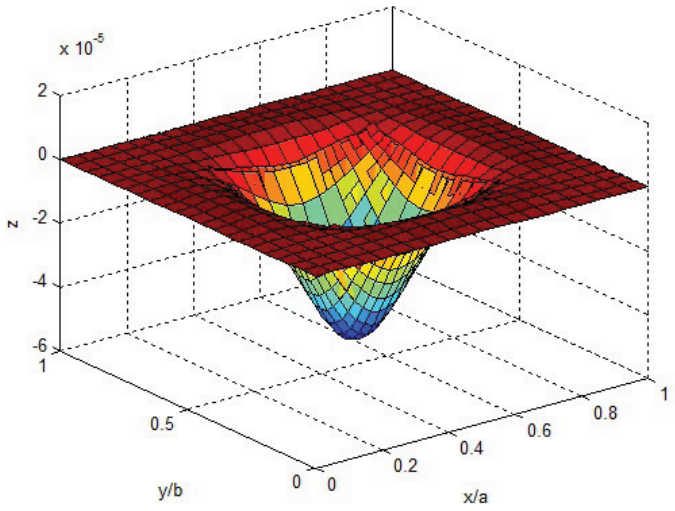

Figure 2. An example of a spurious mode for which only the negative part vibrates together with the associated positive part while the remainder of the structure remains stationary.

References

1 Ilanko, S (2009) Embedding Negative Structures to Model Holes and Cut-Outs, *Proceedings of the 7th International Symposium on Vibrations of Continuous Systems*, 30-33, July Zakopane, Poland.

2 Ilanko, S. (2002) Existence of natural frequencies of systems with imaginary Restraints and their convergence in asymptotic modelling, Journal of Sound and Vibration, 255, 5, 883-898

3 Ilanko. S. (2005) Introducing the Use of Positive and Negative Inertial Functions in asymptotic modeling, Royal Society Proceedings A (Mathematical, Physical and Engineering Sciences) v461, No.2060, 2524-2562.

4 Wagner, A., Spelsberg-Korspeter, G. and Hagedorn, P. (2012) FEM system matrix modifications for structural optimization problems*, 83rd annual Meeting of the GAMM*, March, Darmstadt, Germany, oral presentation.

5 Wagner, A. and Spelsberg-Korspeter, G. (2013): An efficient approach for the assembly of mass and stiffness matrices of structures with modifications, *Journal of Sound and Vibration*, (in press)

Acknowledgement

The authors wish to acknowledge the financial support from the Marsden Fund (http://www.royalsociety.org.nz/programmes/funds/marsden/).

Understanding spurious modes of structures with voids using dynamic stiffness method

[1]David Kennedy, [2]Sinniah Ilanko, [2]Yusuke Mochida
[1]Cardiff School of Engineering, Cardiff University, U.K.
[2]The School of Engineering, The University of Waikato, New Zealand

In another paper being presented at this symposium [1], the existence of natural frequencies and modes of a solid structure which includes an embedded negative structure is discussed. The same paper also describes the challenges associated with the presence of some spurious modes. In this paper, we explain the presence of actual and spurious modes using the exact dynamic stiffness method. We limit the analysis to structures consisting of an assembly of continuous systems (possessing both positive and negative elastic and inertial properties) which are connected at certain nodal points.

Consider modelling an original structure [o] with a void, see Figure 1(a). This could be represented by connecting the full (i.e. perfect) structure [f] to a negative structure [n] which completely cancels part of [f] to yield [o], see Figure 1(b).

This may be considered as the actual structure [o], linked to a positive structure [p] and a corresponding negative structure [n] as shown in Figure 1(c).

The nodes of the system are denoted as follows in the figure:

- o Nodes which are internal to structure (o)
- p Nodes which are internal to structure (p)
- n Nodes which are internal to structure (n)
- c Nodes which are common to all the structures

The nodes denoted p and n are linked together by stiff springs [s].

Let the displacement vectors for the nodes denoted o, p, n and c be $\mathbf{d}_o$, $\mathbf{d}_p$, $\mathbf{d}_n$ and $\mathbf{d}_c$ respectively.

Then the dynamic stiffness matrices and displacement vectors for the system components can be written as follows.

$$\begin{pmatrix} \mathbf{K}_{oo} & \mathbf{K}_{oc} \\ \mathbf{K}_{oc}^{\mathrm{T}} & \mathbf{K}_{cc} \end{pmatrix}, \quad \begin{pmatrix} \mathbf{d}_o \\ \mathbf{d}_c \end{pmatrix} \quad \text{for structure [o]} \tag{1}$$

$$\begin{pmatrix} \mathbf{k}_{11} & \mathbf{k}_{1c} \\ \mathbf{k}_{1c}^{\mathrm{T}} & \mathbf{k}_{cc} \end{pmatrix}, \quad \begin{pmatrix} \mathbf{d}_p \\ \mathbf{d}_c \end{pmatrix} \quad \text{for structure [p]} \tag{2}$$

$$\begin{pmatrix} -\mathbf{k}_{11} & -\mathbf{k}_{1c} \\ -\mathbf{k}_{1c}^{\mathrm{T}} & -\mathbf{k}_{cc} \end{pmatrix}, \begin{pmatrix} \mathbf{d}_n \\ \mathbf{d}_c \end{pmatrix} \quad \text{for structure [n]} \tag{3}$$

$$\begin{pmatrix} \mathbf{S} & -\mathbf{S} \\ -\mathbf{S} & \mathbf{S} \end{pmatrix}, \quad \begin{pmatrix} \mathbf{d}_p \\ \mathbf{d}_n \end{pmatrix} \quad \text{for the springs [s]} \tag{4}$$

where **S** is a diagonal matrix of (large) spring stiffnesses, and superscript T denotes transpose.

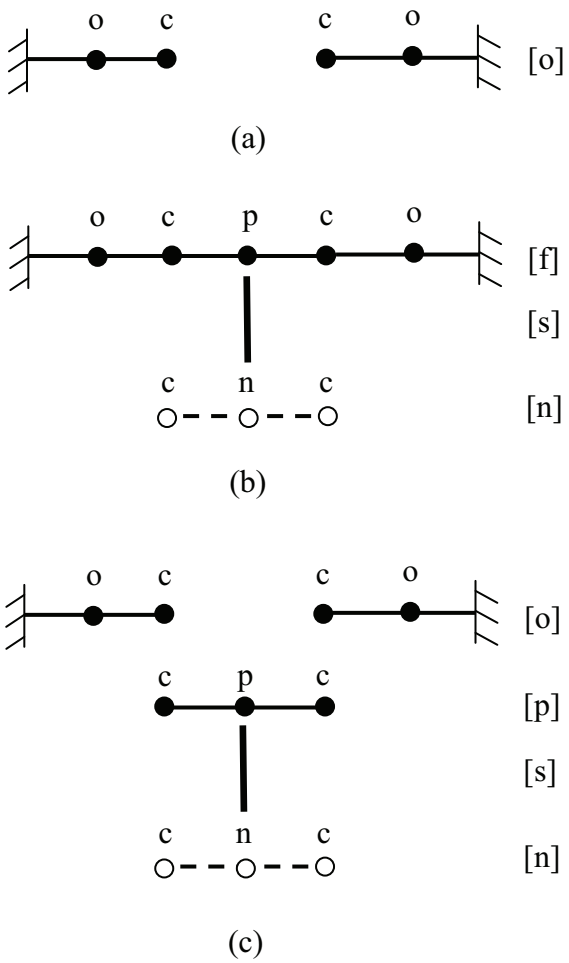

Figure 1. (a) Original structure [o] with a void. (b) Full structure [f] attached by springs [s] to a negative structure [n]. (c) Original structure [o] linked to positive [p] and negative [n] structures attached by springs [s].

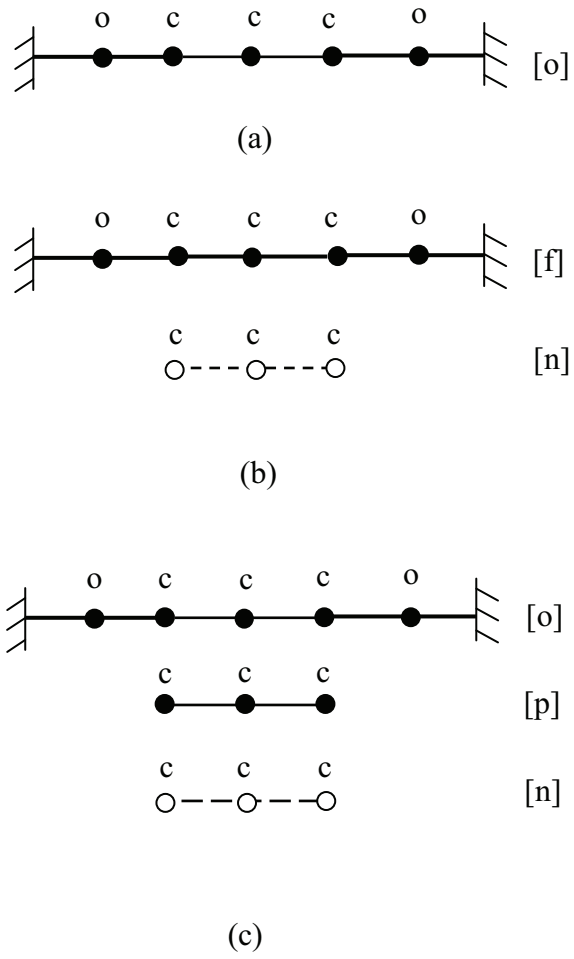

Figure 2. (a) Original structure [o] with damage. (b) Full structure [f] attached to a negative structure [n]. (c) Original structure [o] linked to positive [p] and negative [n] structures.

Thus the global dynamic stiffness equations for free vibration are assembled as

$$\begin{pmatrix} \mathbf{K}_{oo} & \mathbf{0} & \mathbf{0} & \mathbf{K}_{oc} \\ \mathbf{0} & \mathbf{k}_{11}+\mathbf{S} & -\mathbf{S} & \mathbf{k}_{1c} \\ \mathbf{0} & -\mathbf{S} & -\mathbf{k}_{11}+\mathbf{S} & -\mathbf{k}_{1c} \\ \mathbf{K}_{oc}^{\mathrm{T}} & \mathbf{k}_{1c}^{\mathrm{T}} & -\mathbf{k}_{1c}^{\mathrm{T}} & \mathbf{K}_{cc} \end{pmatrix} \begin{pmatrix} \mathbf{d}_o \\ \mathbf{d}_p \\ \mathbf{d}_n \\ \mathbf{d}_c \end{pmatrix} = \begin{pmatrix} \mathbf{0} \\ \mathbf{0} \\ \mathbf{0} \\ \mathbf{0} \end{pmatrix} \tag{5}$$

Eliminating the internal nodes of structure [o] gives

$$\begin{pmatrix} \mathbf{k}_{11}+\mathbf{S} & -\mathbf{S} & \mathbf{k}_{1c} \\ -\mathbf{S} & -\mathbf{k}_{11}+\mathbf{S} & -\mathbf{k}_{1c} \\ \mathbf{k}_{1c}^{\mathrm{T}} & -\mathbf{k}_{1c}^{\mathrm{T}} & \mathbf{K}_{cc}^{*} \end{pmatrix} \begin{pmatrix} \mathbf{d}_p \\ \mathbf{d}_n \\ \mathbf{d}_c \end{pmatrix} = \begin{pmatrix} \mathbf{0} \\ \mathbf{0} \\ \mathbf{0} \end{pmatrix} \tag{6}$$

where $\mathbf{K}_{cc}^{*} = \mathbf{K}_{cc} - \mathbf{K}_{oc}^{\mathrm{T}}\,\mathbf{K}_{oo}^{-1}\mathbf{K}_{oc}$

Adding the first two rows of Eq. (6) gives $\mathbf{k}_{11}(\mathbf{d}_p - \mathbf{d}_n) = \mathbf{0}$ (7)

which is satisfied either if $|\mathbf{k}_{11}|$=0 or if $\mathbf{d}_p = \mathbf{d}_n$.

In the latter case, the displacements at nodes p and n have been made equal regardless of the magnitude of the spring stiffnesses **S**, and the third row of Eq. (6) gives

$$\mathbf{K}^{*}_{cc}\mathbf{d}_c = \mathbf{0} \tag{8}$$

which is identical to the dynamic stiffness equation for structure [o] obtained from Eq. (1) when its internal nodes have been eliminated.

The former case $|\mathbf{k}_{11}|=0$ gives additional spurious eigenvalues, so that the eigenvalues of the combined system are those of structure [o] (i.e. as required), together with those for which $|\mathbf{k}_{11}|=0$ (i.e. spurious eigenvalues).

Figure 2 shows an analogous model in which the actual structure [o] contains a region of damage (i.e. reduced stiffness) rather than a void. In this case, all nodes of structures [p] and [n] also belong to structure [o], so there are no internal nodes denoted p and n. Hence $\mathbf{k}_{11}$ does not exist, no springs are required and the global dynamic stiffness equations (5) simplify to

$$\begin{pmatrix} \mathbf{K}_{oo} & \mathbf{K}_{oc} \\ \mathbf{K}_{oc}^{\mathrm{T}} & \mathbf{K}_{cc} \end{pmatrix} \begin{pmatrix} \mathbf{d}_o \\ \mathbf{d}_c \end{pmatrix} = \begin{pmatrix} \mathbf{0} \\ \mathbf{0} \end{pmatrix} \tag{9}$$

i.e. those of the original structure. Thus there are no spurious eigenvalues.

The difficulty for problems with voids (such as that illustrated in Figure 1) could conceivably be avoided by adding to structure [o] nodes corresponding to nodes p and n (which will therefore become common nodes c), and connecting them to the rest of structure [o] by members with very low stiffness. If these members have no mass there will be no problems associated with their local modes of vibration.

All the above arguments are valid for both discrete and continuous systems provided the force (or moment) - displacement (translation or rotation) relationship at the nodes or nodal lines can be expressed exactly in terms of the frequency. However, the component members of continuous systems conceptually include infinitely many internal nodes and those of structures [p] and [n] will necessarily be distinct. Thus, for the examples of both Figures 1 and 2, spurious modes associated with the fixed-end natural frequencies of structures [p] and [n] might be expected.

The symposium presentation will include an in-depth exploration of the ideas outlined here, illustrated with results for systems of beams.

Acknowledgement

The authors wish to acknowledge the financial support from the Marsden Fund (http://www.royalsociety.org.nz/programmes/funds/marsden/).

References

1. S. Ilanko, Y. Mochida, P. Hagedorn, A. Wagner and D. Kennedy, Modelling voids using embedded negative structures – the story of the spurious modes, *Proceedings of the 9th International Symposium on Vibrations of Continuous Systems.* (accepted)

Motion Control of a Flexible Robot Arm by Utilizing Its Dynamics

Yukinori Kobayashi*, Ryohei Yamakawa, Yizhi Gai, Yohei Hoshino and Takanori Emaru
* Faculty of Engineering, Hokkaido University
N13W8, Kita-ku, Sapporo-shi, Hokkaido, 060-8628, Japan
kobay@eng.hokudai.ac.jp

Key Words: Motion control, Flexible robot arm, Optimization, Ball-throwing motion

1. Introduction

This paper studies highly-efficient motion of a flexible robot arm to throw a ball. Many researchers have investigated the vibration suppression control of flexible robot arms to achieve the precise motion [1]. Flexible structures are used for sports equipment to obtain high performance of motion [2]. In this paper, a flexible arm is used to store potential energy and throw a ball effectively. Input torque determined by using optimization technique is utilized for a motion of the flexible arm. Simulations and experiments are performed to confirm the usefulness of the effective ball-throwing motion.

2. Model descriptions and state equation

Figure 1 shows the model of the flexible robot arm to throw a ball. The model consists of a hub with the radius r_h and a flexible beam fixed on the hub. The beam has a ball holder with a ball at the end of the beam. The O-*XY* coordinate denotes the inertial reference frame which is in global coordinate. The angle θ is the rotational angle of the hub under the torque τ. The beam is treated as a homogeneous isotropic one with uniform cross section. Displacement at an arbitrary point x of the beam is represented by $v(x,t)$. When the modal analysis is employed, the displacement $v(x,t)$ is approximated as

$$v(x,t) = \sum_{i=1}^{n} \phi_i(x) q_i(t) , \tag{1}$$

where $\phi_i(x)$ is the eigenfunction of the vibration of the cantilevered beam and $q_i(t)$ is the time function for each mode of the vibration.

Following the Hamilton's principle, we can obtain the governing equations of the system as follows:

$$\mathbf{M}\ddot{\mathbf{z}} + \mathbf{C}\dot{\mathbf{z}} + \mathbf{K}\mathbf{z} = \mathbf{D}\tau, \ \ \mathbf{z} = \left[\theta \ q_1 \ q_2 \ \cdots \ q_n\right]^T \tag{2}$$

where $\mathbf{M}$ is the mass matrix, $\mathbf{C}$ is the damping matrix, $\mathbf{K}$ is the stiffness matrix and $\mathbf{D} = \left[1 \ \ 0 \ \ \cdots \ \ 0\right]^T$ is the input vector. Vector $\mathbf{z}$ consists of the angle of the hub and time functions for each mode of the vibration of the beam. Introducing state vector $\mathbf{x} = \left[\mathbf{z}, \dot{\mathbf{z}}\right]^T$, Eq.(2) is rewritten as

$$\dot{\mathbf{x}} = \mathbf{A}\mathbf{x} + \mathbf{B}\tau \tag{3}$$

where

$$\mathbf{A} = \begin{bmatrix} 0 & \mathbf{I} \\ -\mathbf{M}^{-1}\mathbf{K} & -\mathbf{M}^{-1}\mathbf{C} \end{bmatrix}, \ \mathbf{B} = \begin{bmatrix} 0 \\ -\mathbf{M}^{-1}\mathbf{D} \end{bmatrix}. \tag{4}$$

In this paper, we call the system holding a ball as Model 1 and the system without ball as Model 2. Model 1 is employed during the takeaway and throwing motion before the velocity of the hand becomes maximum value. At the maximum velocity of the hand, the ball is released and Model 2 is employed for the following simulation.

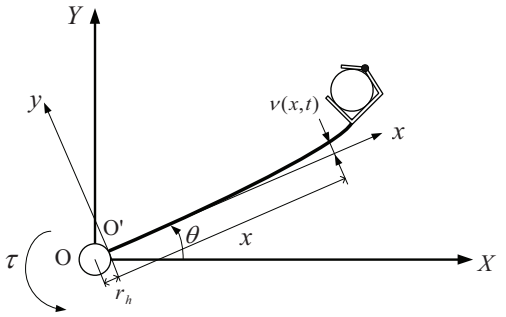

Fig.1 Model of a ball throwing robot arm

3. Input torque optimization

Whole motion of the robot arm is designed as the ball-throwing motion following the takeaway motion. To realize this motion, input toque is determined by the combination of sinusoidal functions as follows:

$$\tau = \begin{cases} -A_1 \sin\dfrac{2\pi}{T_1} t & \left(0 \le t \le \dfrac{T_1}{2}\right) \\ A_2 \sin\dfrac{2\pi}{T_2}\left(t - \dfrac{T_1}{2}\right) & \left(\dfrac{T_1}{2} < t \le \dfrac{T_1+T_2}{2}\right) \\ 0 & \left(\dfrac{T_1+T_2}{2} < t\right) \end{cases} \tag{5}$$

where A_1 and T_1 are the amplitude and period for the takeaway motion, and A_2 and T_2 are the amplitude and period for the ball-throwing motion. These four parameters are optimized by employing Genetic Algorithm (GA) and Particle Swarm Optimization (PSO) [3]. A cost function for the PSO is defined as

$$J = w_1 \frac{1}{v_{\max}} + w_2 \int_0^{\infty} u(t)\,\dot{\theta}(t)dt + w_3\left(\frac{T_1+T_2}{2}\right), \tag{6}$$

where $v_{\max}$ is the release speed of the ball and w_i denotes the weight for each term. This cost function is minimized to obtain the optimized solution. Second term expresses the external work done by the motor and third term is the input time of the torque. In the case of the GA, inverse function of Eq. (6) is used as the cost function to maximize.

4. Simulation and experiment

Experimental study is performed by using a steel beam reinforced by FRP whose length is 0.37m and bending rigidity is 2.12Nm^2. Figure 2 shows the experimental setup. A direct drive motor (SGMCS-05B3C11, YASKAWA) is used to rotate the robot arm. Strain of the beam is measured and control command is generated by using the DSP controller (iBIS DSP 7101, MTT Corp.). A robot hand to hold a ball is attached at the tip of the beam. An artificial muscle, which is a pneumatic actuator (Sik-t-BW12PE30S, SQUSE), is used to actuate the hand mechanism. While the robot arm is operated for the takeaway motion, the robot hand is closed to hold the ball. When the velocity of the robot hand becomes fastest, the robot hand is opened to release the ball. A tennis ball was used in this experiment. Weighting coefficients in Eq. (6) are given as w_1=20, w_2=1 and w_3=0.1 in the simulation. Fundamental natural frequency of the arm with the hand mechanism is 4.821Hz. Considering the constraint conditions like maximum torque of the motor and maximum deformation of the beam, simulations by GA and PSO were conducted to obtain the optimum combinations of parameters. As the result of five times calculations by PSO and GA, the cost function by PSO showed better values than that by GA. Although here is a possibility to tune parameters for GA better, the best set by PSO (A_1, T_1, A_2, T_2) = (0.058, 0.102, 2.285, 0.582), was selected as the input for experimental study. The value of the cost function was J = 6.551.

Figure 3 shows the comparison of rotating angles between the simulation and experiments. Vertical line shows the release point of the ball where the velocity of the ball becomes fastest. Figure 4 shows the comparison of the strain of the arm between the simulation and experiment. Although here is a slight phase difference between both results, the simulation result expresses the dynamic property of the robot arm well.

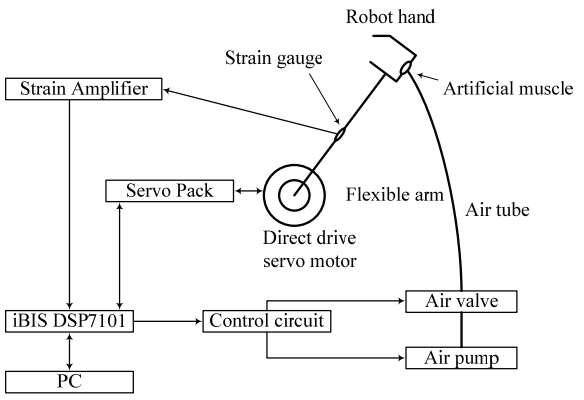

Fig.2 Experimental setup

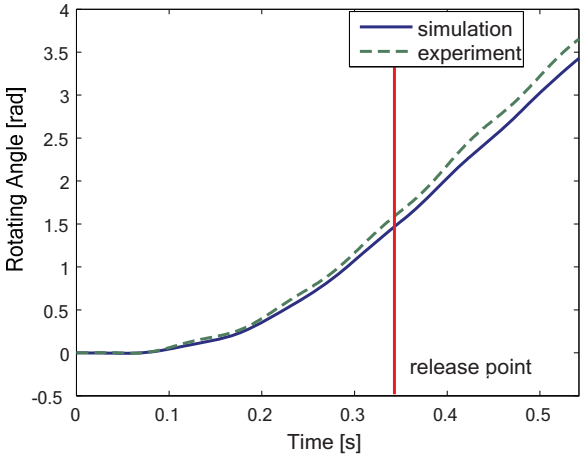

Fig.3 Comparison of rotating angles between simulation and experiment

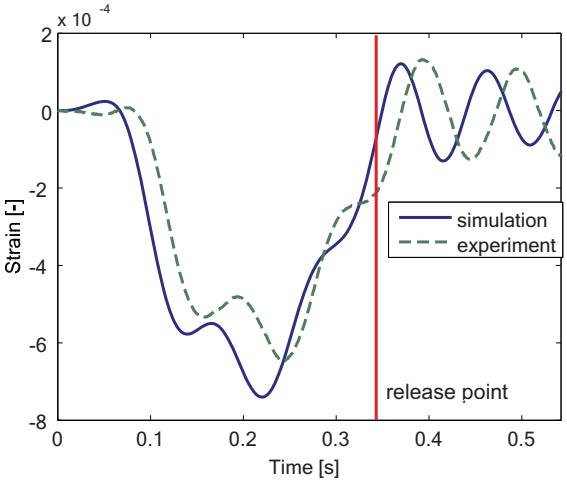

Fig.4 Comparison of strain between simulation and experiment

A simultaneous optimization of parameters for the input torque and the beam is attempted by adding the bending rigidity and length of the beam as the parameters. As the result of calculations by PSO, the best result was obtained in the case (A_1, T_1, A_2, T_2, EI, l) = (2.676, 0.100, 4.659, 0.324, 4.950, 0.353). The value of the cost function J = 6.484 was smaller than that of the previous optimization result.

Figure 5 shows the comparison of velocities of the robot hand between rigid and flexible arms. At the release point of the ball, velocity of the flexible arm is faster than that of the rigid arm. This result shows the possibility that we can design a flexible robot arm of high performance by utilizing the flexibility as an energy storage mechanism.

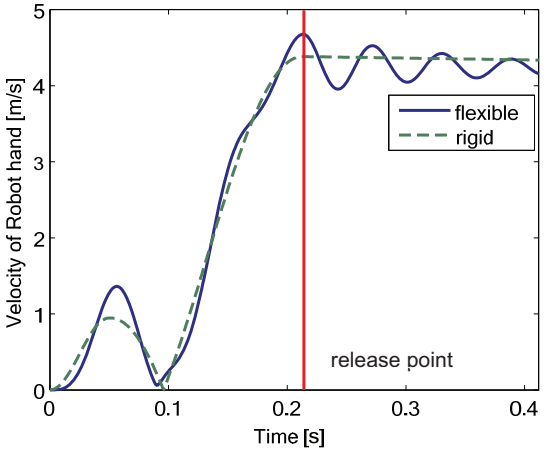

Fig.5 Comparison of velocities of robot hand between rigid and flexible arms

5. Conclusion

This paper derived the state equation for the ball-throwing flexible manipulator. GA and PSO algorithms were introduced to optimize the parameters for the input torque. Simultaneous optimization of the parameters for input torque and structure were also studied by the simulation. Simulation results show good agreement with those of experiment and the optimized results for the flexible arm gave better performance than that of the rigid arm.

References

[1] A. Abe, Residual Vibration Suppression for Robot Manipulator Attached to a Flexible Link by Using Soft Computing Techniques, *Proceedings of the* 2011 *IEEE International Conference on Robotics and Biomimetics*, (2011), pp. 2324–2329.

[2] Y. Hoshino, Y. Kobayashi, Shock and Vibration Control of a Golf-Swing Robot at Impacting the Ball, *Journal of System Design and Dynamics*, Vol.2,No.5, (2008), pp. 1069–1080.

[3] K. E. Parsopoulos and M. N. Vrahatis, *Particle Swarm Optimization and Intelligence: Advances and Applications*. Information Science Reference, Hershey, New York, (2009), pp. 253-254.

NATURAL FREQUENCIES OF BEAMS AND FRAMES WITH CONCENTRATED OPEN CRACKS

Amr Labib, David Kennedy and Carol A. Featherston

Cardiff School of Engineering, Cardiff University, Queen's Buildings, The Parade, Cardiff CF24 3AA, United Kingdom. Email kennedyd@cf.ac.uk

The dynamic stiffness matrix is obtained for a Bernoulli-Euler beam with one or more open cracks, each concentrated at a specific axial location. Such a crack is represented by a rotational spring of stiffness k^*, which is assumed to be related to the crack depth d by a suitable empirical formula, e.g. see [1, 2].

A beam portion containing a single crack is modelled by connecting two elements, labelled A and B, as shown in Figure 1. The exact dynamic stiffness equations for such an element m (=A, B), connecting nodes i and j, with length L_m, Young's modulus E, second moment of area I and mass per unit length μ, which is vibrating at frequency ω are given by [3]

$$\begin{Bmatrix} F_i \\ M_i \\ F_j \\ M_j \end{Bmatrix} = \begin{bmatrix} a_m & b_m & -d_m & e_m \\ b_m & c_m & -\varepsilon_m & f_m \\ -d_m & -\varepsilon_m & \alpha_m & -\beta_m \\ e_m & f_m & -\beta_m & \gamma_m \end{bmatrix} \begin{Bmatrix} w_i \\ \theta_i \\ w_j \\ \theta_j \end{Bmatrix} \tag{1}$$

where, for a uniform member,

$$\left.\begin{aligned} a_m = \alpha_m = EI\lambda^3\left(S_m C_m^{'} + C_m S_m^{'}\right)/\sigma_m \quad & b_m = \beta_m = EI\lambda^2\left(S_m S_m^{'}\right)/\sigma_m \\ c_m = \gamma_m = EI\lambda\left(S_m C_m^{'} - C_m S_m^{'}\right)/\sigma_m \quad & d_m = EI\lambda^3\left(S_m + S_m^{'}\right)/\sigma_m \\ e_m = \varepsilon_m = EI\lambda^2\left(C_m^{'} - C_m\right)/\sigma_m \quad & f_m = EI\lambda\left(S_m^{'} - S_m\right)/\sigma_m \end{aligned}\right\} \tag{2}$$

$$\left.\begin{aligned} C_m = \cos(\lambda L_m) \quad S_m = \sin(\lambda L_m) \quad C_m^{'} = \cosh(\lambda L_m), \quad S_m^{'} = \sinh(\lambda L_m) \\ \lambda = \sqrt[4]{\mu\omega^2/EI} \quad \sigma_m = 1 - C_m C_m^{'} \end{aligned}\right\} \tag{3}$$

Axial stiffness is disregarded, so only transverse displacements and rotations are considered. Connecting elements A and B as shown in Figure 1 gives the stiffness equations

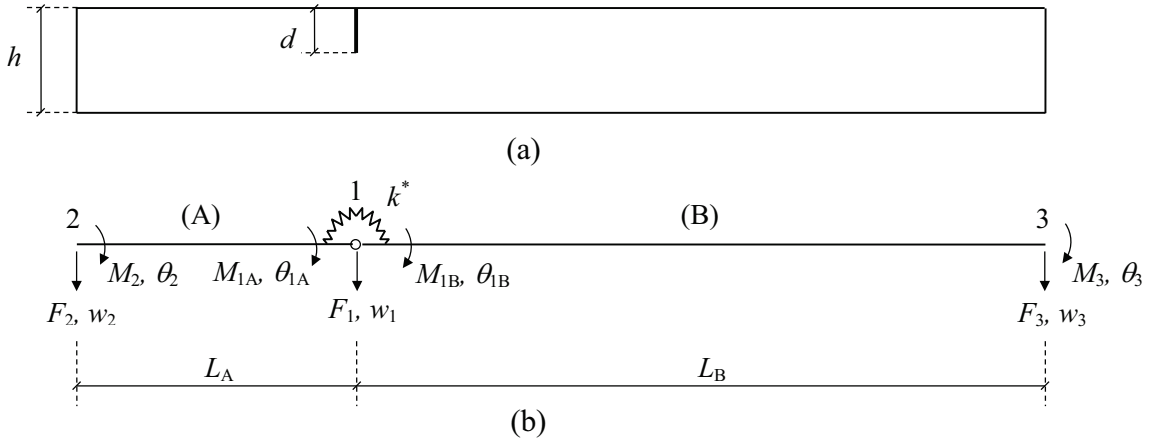

Figure 1. (a) Beam of height h with a crack of depth d. (b) Rotational spring model.

$$\begin{Bmatrix} M_{1A} \\ M_{1B} \\ F_1 \\ F_2 \\ M_2 \\ F_3 \\ M_3 \end{Bmatrix} = \begin{bmatrix} \gamma_A + k^* & -k^* & -\beta_A & e_A & f_A & 0 & 0 \\ -k^* & c_B + k^* & b_B & 0 & 0 & -\varepsilon_B & f_B \\ -\beta_A & b_B & \alpha_A + a_B & -d_A & -\varepsilon_A & -d_B & e_B \\ e_A & 0 & -d_A & a_A & b_A & 0 & 0 \\ f_A & 0 & -\varepsilon_A & b_A & c_A & 0 & 0 \\ 0 & -\varepsilon_B & -d_B & 0 & 0 & \alpha_B & -\beta_B \\ 0 & f_B & e_B & 0 & 0 & -\beta_B & \gamma_B \end{bmatrix} \tag{4}$$

where the presence of the rotational spring results in the separate moments and rotations at node 1, indicated by the subscripts A and B. Applying partial Gaussian elimination, without row interchanges, to the first three rows and columns of Equation (4) gives the stiffness equations for the combined element (AB) in the form of Equation (1) with

$$\left.\begin{array}{ll} a_m = a_A - e_A^2 q_1 - p_1^2 \Delta_3 & b_m = b_A - e_A f_A q_1 - p_1 p_2 \Delta_3 \\ c_m = c_A - f_A^2 q_1 - p_2^2 \Delta_3 & d_m = -e_A \varepsilon_B \Delta_1 \Delta_2 + p_1 p_3 \Delta_3 \\ e_m = -e_A f_B \Delta_1 \Delta_2 - p_1 p_4 \Delta_3 & f_m = -f_A f_B \Delta_1 \Delta_2 - p_2 p_4 \Delta_3 \\ \alpha_m = \alpha_B - \varepsilon_B^2 \Delta_2 - p_3^2 \Delta_3 & \beta_m = \beta_B - \varepsilon_B f_B \Delta_2 + p_3 p_4 \Delta_3 \\ \gamma_m = \gamma_B - f_B^2 \Delta_2 - p_4^2 \Delta_3 & \varepsilon_m = -f_A \varepsilon_B \Delta_1 \Delta_2 + p_2 p_3 \Delta_3 \end{array}\right\} \tag{5}$$

where

$$\left.\begin{array}{ll} p_1 = -d_A + e_A q_2 & p_2 = -\varepsilon_A + f_A q_2 \\ p_3 = -d_B + \varepsilon_B q_3 & p_4 = e_B - f_B q_3 \\ q_1 = \Delta_1 (f^* + \Delta_1 \Delta_2) & q_2 = \beta_A q_1 - b_B \Delta_1 \Delta_2 \\ q_3 = \Delta_2 (b_B - \beta_A \Delta_1) & \Delta_1 = 1/(1 + \gamma_A f^*) \\ \Delta_2 = 1/(c_B + \gamma_A \Delta_1) & \Delta_3 = 1/(\alpha_A + a_B - \beta_A^2 q_1 - b_B^2 \Delta_2 + 2\beta_A b_B \Delta_1 \Delta_2) \end{array}\right\} \tag{6}$$

and $f^* = 1/k^*$ is the compliance of the spring. If there is no crack, $f^* = 0$ and the expressions in Equation (5) reduce to those of Equation (2) for a uniform beam of length $L_m = L_A + L_B$.

Multiple cracks connecting elements A, B, C, … are modelled by recursively applying the above procedure to derive element AB from elements A and B, element ABC from AB and C, and so on, until a 4×4 dynamic stiffness matrix **K** is obtained for the whole beam. Thus the damaged beam can be easily assembled into a larger frame structure.

Undamped natural frequencies are found to any required accuracy using the Wittrick-Williams algorithm [4]. The number of natural frequencies lying below a trial frequency ω^* is given by

$$J = s\{\mathbf{K}\} + \sum_m J_m + \sum_c J_c \tag{7}$$

where: $s\{\mathbf{K}\}$ is the sign count of **K**, i.e. the number of negative leading diagonal elements of the upper triangular matrix obtained from **K** by standard Gaussian elimination; for each element m = A, B, C, …, J_m is the number of fixed end natural frequencies lying below ω^*; and for each crack c,

$$J_c = sg\{\Delta_1\} + sg\{\Delta_2\} + sg\{\Delta_3\} \tag{8}$$

where $sg\{\Delta\} = 1$ if $\Delta < 0$, and = 0 otherwise.

Analysis by previous authors also included shear and longitudinal springs [5], and obtained the dynamic stiffness matrix using a series solution [6]. The results in Tables 1 and 2 show that the present method compares well with these earlier approaches. In addition, it permits the use of the Wittrick-Williams algorithm to determine higher natural frequencies exactly without requiring the insertion of additional nodes in the global stiffness matrix.

Table 1. Natural frequencies of a cantilever beam of length 0.2 m, depth h = 0.0078 m, EI = 213.548 Nm^2, m = 1.5308 kg/m, with a crack of depth d located at a distance L_A from the clamped end.

L_A (m)	L_B (m)	d/h	k^* (kNm/rad)	ω_1 (rad/s)		ω_2 (rad/s)		ω_3 (rad/s)	
				Present	[5]	Present	[5]	Present	[5]
-	-	Intact	∞	1038.2	1038.2	6506.3	6506.4	18218	18218
0.08	0.12	0.2	130	1034.6	1031.8	6469.6	6441.3	18152	18098
0.08	0.12	0.4	28.8	1022.2	1010.1	6348.9	6237.0	17942	17740
0.08	0.12	0.6	8.39	985.98	949.82	6036.0	5768.5	17447	17015
0.12	0.08	0.2	130	1037.3	1036.6	6456.8	6419.0	18137	18070
0.12	0.08	0.4	28.8	1034.2	1030.9	6292.3	6139.9	17879	17633
0.12	0.08	0.6	8.39	1024.4	1013.7	5852.0	5468.2	17276	16761

Table 2. First four (non-rigid) natural frequencies of a beam of length 1.208 m, depth h = 0.01 m, EI = 1477 Nm^2, m = 6.30 kg/m, with free ends and symmetrically located cracks of depth d in the top and bottom surfaces at a distance L_A = 0.445 m from one end.

d/h	k^* (kNm/rad)	ω_1 (Hz)		ω_2 (Hz)		ω_3 (Hz)		ω_4 (Hz)	
		Present	[6]	Present	[6]	Present	[6]	Present	[6]
Intact	∞	37.4	36.6	103.0	100.9	201.9	197.8	333.8	326.9
0.1	602.5	37.3	36.5	102.8	100.7	201.9	197.8	333.2	326.3
0.2	111.9	37.0	36.2	102.1	100.1	201.9	197.7	330.6	323.9
0.3	33.27	36.1	35.4	100.3	98.3	201.8	197.7	324.0	317.7
0.4	7.766	32.7	32.2	94.3	92.6	201.6	197.5	304.6	299.0

The Symposium presentation will include results for frames formed of multi-cracked beams. It is planned to study in depth the effects of damage on the natural frequencies and mode shapes, with a view to the identification of damage by vibration measurements and analysis similar to that in [7].

Acknowledgement
Financial support is acknowledged from the Marsden Fund of the Royal Society of New Zealand.

References

[1] A.D. Dimarogonas. Vibration of cracked structures: a state of the art review. *Engineering Fracture Mechanics*, 55(5):831-837, 1996.

[2] S. Caddemi, I. Caliò. Exact closed-form solution for the vibration modes of the Euler-Bernoulli beam with multiple open cracks. *Journal of Sound and Vibration*, 327(3–5):473-489, 2009.

[3] S. Błaszkowiak, Z. Kączkowski. *Iterative Methods in Structural Analysis*. Oxford: Pergamon Press, 1966.

[4] W.H. Wittrick, F.W. Williams. A general algorithm for computing natural frequencies of elastic structures. *Quarterly Journal of Mechanics and Applied Mathematics*, 24(3):263-284, 1971.

[5] J.R. Banerjee, S. Guo. On the dynamics of a cracked beam. *Proceedings of the 50th AIAA/ASME/ASCE/AHS/ASC Structures, Structural Dynamics, and Materials Conference*, Palm Springs, USA, Paper AIAA-2009-2429, 2009.

[6] S. Caddemi, A. Morassi. Multi-cracked Euler-Bernoulli beams: mathematical modeling and exact solutions. *International Journal of Solids and Structures*, 50(6):944-956, 2013.

[7] A. Greco, A. Pau. Damage identification in Euler frames. *Computers and Structures*, 92-93:328-336, 2012.

Looking Back at Curve Veering

Arthur Leissa
Fort Collins, Colorado, USA

Fifty years ago the writer came across a paper [1] which used an approximate series-type method of analysis to obtain the free vibration frequencies of thin, cantilevered, rectangular plates. No exact solutions for this problem are known. This paper showed many astonishing curves of frequencies plotted versus the nondimensional ratio of length to width of the plate. The curves behaved smoothly everywhere except where they approached each other. Then, instead of continuing smoothly and crossing, they each suddenly and violently veered away from each other and continued along the path that the other would have taken had it been permitted to cross! The same type of curve veering was shown in another paper [2] for the frequencies of rectangular plates (1) completely clamped and (2) clamped on two edges, free on the two others.

Furthermore, if the frequency curves *did* cross, the same basic mode shape of free vibration would exist before and after the crossing. In the "transition zones" [1] of frequencies veering away, the mode shapes and nodal patterns must undergo a violent change --- figuratively speaking, "a dragonfly one instant, a butterfly the next, and something indescribable in between" [3].

Subsequently, in reading the extensive literature for his plates vibration monograph [4], as well as numerous other published papers for eigenvalue problems, the present writer encountered this "curve veering" many times. While in Switzerland for the academic year 1972-1973, he decided to explore whether curve veering could be caused by using a well-known approximate method of analysis on a relatively simple problem, for which a simple, exact solution is available --- the transverse free vibrations of a stretched rectangular membrane. These results were published in ZAMP [3], and are described very briefly below.

Consider a uniformly stretched, rectangular membrane of dimensions a x b, with the origin of a rectangular x, y coordinate system located in one corner of the membrane, and the axes falling along its edges. An exact solution of the governing two-dimensional wave equation of motion is obtained using the transverse displacement as $w(x,y) = \sin m\pi x/a \ \sin n\pi y/b$, where m and n are integers. Substituting this into the wave equation yields the well-known nondimensional frequency parameters

$$\lambda^2 = (\pi/2)^2 \left[m^2 + (a/b)^2 n^2\right] = \omega^2 a^2 \rho / T \qquad (1)$$

where ω is a frequency, ρ is mass density per unit area, T is the membrane tension per edge length, and m and n are integers. It is seen from Eq. (1) that λ^2 plotted versus the square of the aspect ratio (a/b) determines a family of straight lines. Three of these are depicted in

Figure 1 as dashed lines for mn = 11, 13 and 31, corresponding to mode shapes which are doubly symmetric. It is seen there that λ^2 for the 13 and 31 modes cross at a/b = 1.

Approximate solutions to this problem may be obtained by using the Galerkin or Ritz methods, which are equivalent here. Considering the symmetries (and antisymmetries) of the free vibration modes, a ξ,η coordinate system is now chosen with origin at the center of the rectangular membrane. It is clear that the boundary conditions W = 0 are satisfied exactly on all four edges by taking the algebraic polynomial

$$W = (\xi^2 - 1)(\eta^2 - 1)\sum_{i,j}^{M,N} a_{ij}\,\xi^i \eta^j \qquad (2)$$

where $\xi = 2x/a$, $\eta = 2y/b$; i and j are integers 0, 1, 2... ; and the a_{ij} are undetermined coefficients.

Retaining only the first three doubly-symmetric terms of the algebraic series in Eq. (2), (i, j = 0, 2) and using the Galerkin or Ritz methods, yields a third order determinant for upper bound approximations of λ^2, which are shown by the solid lines in Fig. 1. The curve for the lowest frequency falls virtually on top of that for the exact one. The curves for the higher two approximate eigenvalues λ_{13}^2 and λ_{31}^2 appear in Fig. 2 to be straight lines, parallel to or rotated from the corresponding exact value straight lines. The lines seem to cross at a/b = 1. However, enlarging Fig. 1 a hundred times, and looking closely in the interval $0.95 \leq (a/b)^2 \leq 1.05$, as shown in Fig. 2, it is seen that the lines veer sharply away from each other in this interval.

Free vibration mode shapes and nodal patterns for the approximate solution are obtained in the usual manner by substituting the eigenvalues back into the homogeneous equations which generated the frequency determinant. The change in the nodal patterns in the interval $0.95 \leq (a/b)^2 \leq 1.00$ is shown in Fig.3 for the lower curve of Fig.2. Only the first of the four membrane quadrants is shown. The similar drastic change in the nodal patterns of the 31 mode for $(a/b)^2 \leq 0.95$ is shown by the solid lines in Fig. 4. For a/b = 1 the approximate solution yields a nodal circle in Fig. 4. The corresponding line for the EXACT solution is the dashed-line, near-circle in Fig.4.

In the above example the "curve veering" aberration of reality occurs because of the use of an approximate solution method. Yet the method has widespread usage for free vibration problems. In this example the aberration also implies coupling of exact modes when there is none. Here the approximate solution eigenfunctions are representable by infinite Fourier series, typical terms of which are the exact trigonometric eigenfunction terms. Perhaps most importantly, the approximation causing the aberration may occur in the mathematical model (e.g. differential equations and boundary conditions) of a physical phenomenon.

In addition to his early encounter [1,2] with curve veering, and his later investigation of this phenomenon [3], the writer has seen it many times in publications dealing with eigenvalue problems.

REFERENCES:

1. R. W. Claassen and C.J. Thorne, *Vibrations of a Rectangular Cantilever Plate,* J. Aerospace Sci., Vol. 29, pp. 1300-1305 (1962).
2. R. W. Claassen and C.J. Thorne, *Vibrations of Thin Rectangular Isotropic Plates,* J. Appl. Mech., Vol. 28, pp. 304-305 (1961).
3. A. W. Leissa, *On a Curve Veering Aberration,* J. Appl. Math. Phys. (ZAMP), Vol. 25, pp. 99-111 (1974).
4. A. W. Leissa, *VIBRATION OF PLATES,* NASA SP-160, U.S. Govt. Printing Off., 353 pp., (1969), Acoust. Soc. Amer. (1993).

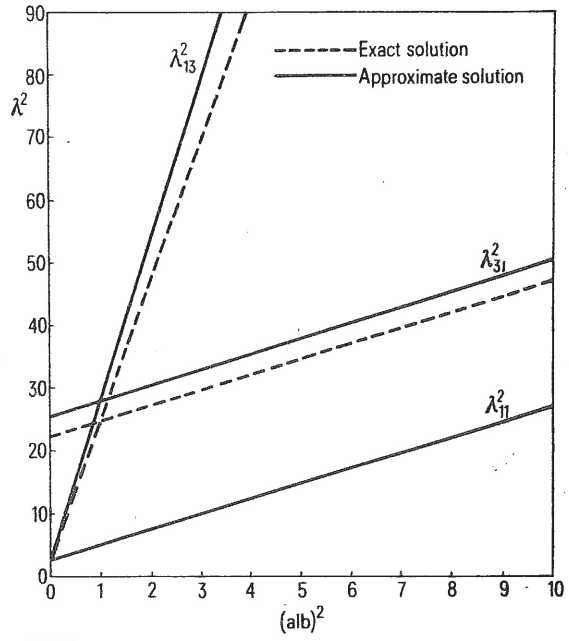

Figure 1

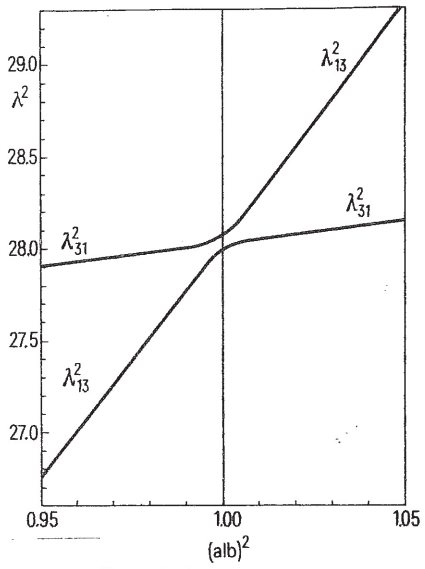

Figure 2

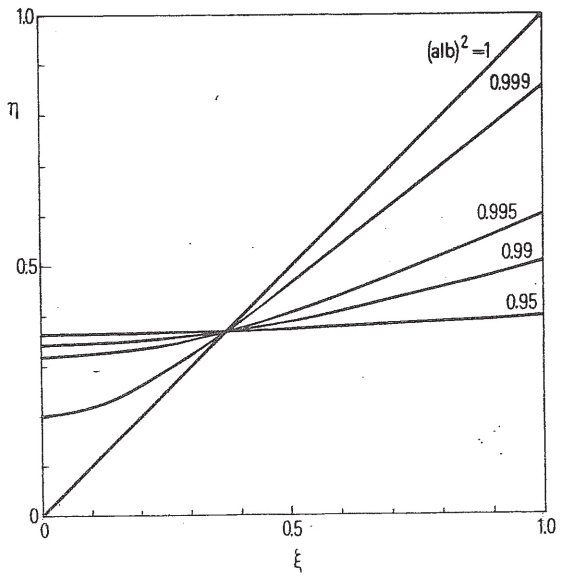

Figure 3

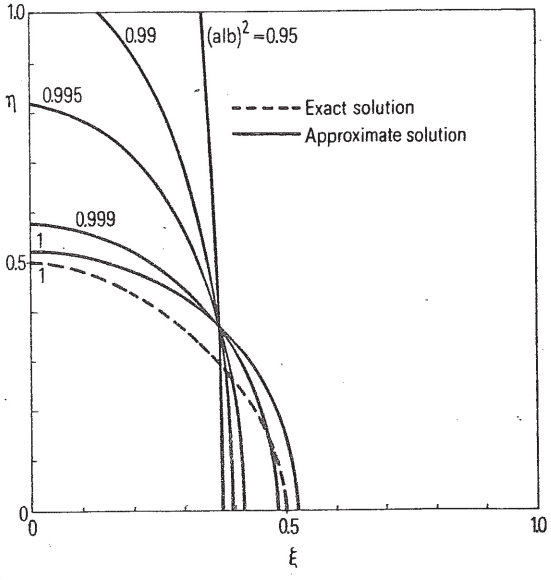

Figure 4

Chaotic Vibrations of a Shell-panel with In-plane Asymmetric Elastic Constraints

Shinichi MARUYAMA, Ken-ichi NAGAI, Suguru SAKURAI and Takao YAMAGUCHI
Division of Mechanical Science and Technology, Faculty of Science and Technology,
Gunma University, 1-5-1 Tenjin-cho, Kiryu, Gunma 376-8515, JAPAN,
maruyama@gunma-u.ac.jp

1. Introduction Recently, technology of micro electro-mechanical systems (MEMS) has been developed drastically. In such devices, lightweight thin plates and shell-panels are widely utilized. In practical applications, the boundaries of the plates and shells are often constrained by other elastic structures. Furthermore, the boundaries might be subjected to non-uniform in-plane compression as well as uniform compression. Nonlinear and chaotic vibrations of the shell-panels, which are generated owing to dynamic snap through or internal resonance, are sensitive to the boundary conditions. Therefore, in this paper, analytical results are presented on chaotic vibrations of a shell-panel with in-plane asymmetric elastic constraints. The simply supported shell-panel is subjected to gravitational and periodic acceleration laterally. The panel is also constrained with in-plane uniform and asymmetric displacements elastically. Neglecting the effect of in-plane inertia force, the Donnell type equations modified with lateral inertia are applied as the governing equations of the shell-panel. The response of lateral deflection is assumed with multiple modes of vibration. Stress function is introduced to satisfy compatibility equation and in-plane boundary condition. Applying the Galerkin procedure, equation of motion is reduced to a set of nonlinear ordinary differential equations. Nonlinear periodic responses are calculated with the harmonic balance method. Non-periodic responses are integrated numerically.

2. Procedure of Analysis Fig. 1 shows the analytical model of the rectangular shell-panel in this research. All the symbols in the figure are shown with non-dimensional notations. We introduce the ξ, η axes along the in-plane directions of the shell-panel and the z axis in the lateral direction. The origin is taken at the center of the panel. The symbols α_x, α_y are non-dimensional curvatures in ξ and η directions, respectively. The symbols w, w_0 denote the deflection and initial deflection of the panel, respectively, and u, v are in-plane displacements in the ξ and η directions, respectively. We assume that the boundaries of the panel are simply supported in the lateral direction and are elastically constrained in the normal in-plane direction. The symbols k_{xm}, k_{xp} and k_{ym}, k_{yp} are spring constants per unit length corresponding to the elastic constraints. At the outer ends of the elastic constraints, initial uniform in-plane displacements u_{0ms}, u_{0ps}, v_{0ms}, v_{0ps} and initial asymmetric in-plane displacements u_{0ma}, u_{0pa}, v_{0ma}, v_{0pa} are applied in the ξ, η direction, respectively. The Poison's ratio of the panel is denoted by ν. In the lateral direction, the shell-panel is assumed to be subjected to static and periodic acceleration $p_s + p_d \cos\omega\tau$, where p_s, p_d are magnitude of static acceleration and amplitude of periodic acceleration, respectively, ω is the excitation frequency and τ is the time. We assume the panel is sufficiently thin and that the in-plane inertia can be neglected, the equation of motion of the shell-panel is expressed as the following equations.

$$L(w,f) = w_{,\tau\tau} + \bar{\nabla}^4(w-w_0) - \alpha_x\beta^2 f_{,\eta\eta} - \alpha_y f_{,\xi\xi} - \beta^2(f_{,\xi\xi}w_{,\eta\eta} - 2f_{,\xi\eta}w_{,\xi\eta} - f_{,\eta\eta}w_{,\xi\xi}) - (p_s + p_d\cos\omega\tau) - q_s\delta(\xi-\xi_1)\delta(\eta-\eta_1) = 0 \tag{1a}$$

$$\bar{\nabla}^4 f = c\left[-\alpha_x\beta^2(w-w_0)_{,\eta\eta} - \alpha_y(w-w_0)_{,\xi\xi} + \beta^2\left\{w_{,\xi\eta}^2 - w_{0,\xi\eta}^2 - \left(w_{,\xi\xi}w_{,\eta\eta} - w_{0,\xi\xi}w_{0,\eta\eta}\right)\right\}\right] \tag{1b}$$

Equation (1a) denotes the equation of motion of the panel in the lateral direction, and Eq (1b) is the compatibility equation of the in-plane strain in terms of the stress function f, which is related to the in-plane resultant force n_x, n_y, n_{xy} as follows.

$$n_x = \beta^2 f_{,\eta\eta},\ n_y = f_{,\xi\xi},\ n_{xy} = -\beta f_{,\xi\eta} \tag{2}$$

The simply-supported boundary condition for the deflection is denoted by,

$$\xi=-1/2,\ 1/2\ :\ w=0,\ w_{,\xi\xi}=0,\quad \eta=-1/2,\ 1/2\ :\ w=0,\ w_{,\eta\eta}=0 \tag{3}$$

The deflection and initial deflection, satisfying the foregoing condition, are assumed as follows.

$$\left[w(\xi,\eta,\tau),w_0(\xi,\eta)\right]=\sum_m\sum_n\left[\hat{b}_{mn}(\tau),\hat{a}_{mn}\right]\hat{\zeta}_{mn}(\xi,\eta),\ \ \hat{\zeta}_{mn}(\xi,\eta)=\sin\left[m\pi\left(\xi+1/2\right)\right]\sin\left[n\pi\left(\eta+1/2\right)\right] \tag{4}$$

The notation $\hat{b}_{mn}(\tau)$ is unknown time function, $\hat{a}_{mn}$ is the known constants for initial deflection and $\hat{\zeta}_{mn}(\xi,\eta)$ is the sinusoidal function for the coordinate function. The integers m, n are half-wave numbers in the ξ, η directions, respectively.

The solution of the compatibility equation (1b) can be expressed as follows.

$$f=f_0+f_1+f_2,\quad f_0=\frac{1}{2}p_{\mathrm{y}}\xi^2+\frac{1}{2}p_{\mathrm{x}}\eta^2+p_{\mathrm{xy}}\xi\eta+\frac{1}{6}p_{\mathrm{ya}}\xi^3+\frac{1}{6}p_{\mathrm{xa}}\eta^3 \tag{5}$$

In the above expression, f_1, f_2 are the particular solution corresponding to the linear and square terms of deflection, respectively, in the right-hand-side of Eq. (1b), which can be expressed with trigonometric functions. The notation f_0 is the approximated homogeneous solution of Eq. (1b), where p_x, p_y correspond to uniform normal stresses, p_{xy} denotes uniform shear stress and p_{xa}, p_{ya} denote normal stresses proportionally distribute along the edges. These unknown coefficients can be determined by equating the virtual work by the in-plane forces, which corresponds to the in-plane boundary condition, to be zero as follows.

$$\begin{aligned}
&\left[\int_{-1/2}^{1/2}\left\{n_x+k_{xp}\left(u-u_{0ps}-2u_{0pa}\eta\right)\right\}\delta u\,d\eta\right]_{\xi=1/2}-\left[\int_{-1/2}^{1/2}\left\{n_x-k_{xm}\left(u-u_{0ms}-2u_{0ma}\eta\right)\right\}\delta u\,d\eta\right]_{\xi=-1/2}\\
&+\left[\beta\int_{-1/2}^{1/2}\left\{n_y+k_{yp}\left(v-v_{0ps}-2v_{0pa}\xi\right)\right\}\delta v\,d\xi\right]_{\eta=1/2}-\left[\beta\int_{-1/2}^{1/2}\left\{n_y-k_{ym}\left(v-v_{0ms}-2v_{0ma}\xi\right)\right\}\delta v\,d\xi\right]_{\eta=-1/2}\\
&+\left[\int_{-1/2}^{1/2}n_{xy}\,\delta v\,d\eta\right]_{\xi=1/2}-\left[\int_{-1/2}^{1/2}n_{xy}\,\delta v\,d\eta\right]_{\xi=-1/2}+\left[\beta\int_{-1/2}^{1/2}n_{xy}\,\delta u\,d\xi\right]_{\eta=1/2}-\left[\beta\int_{-1/2}^{1/2}n_{xy}\,\delta u\,d\xi\right]_{\eta=-1/2}
\end{aligned} \tag{6}$$

Then, substituting Eqs. (4) and (5) to Eq. (1a) and applying the Galerkin procedure, the equation of motion is reduced to ordinary differential equations in terms of $\hat{b}$ in multiple-degree-of-freedom system. Neglecting the time variant terms, static deflection due to the static lateral acceleration and the in-plane initial displacements is obtained. Next, the ordinary differential equation is transformed to the equation in terms of the dynamic variable $\tilde{b}_j$ which is measured from the static equilibrium position. Furthermore, the ordinary differential equations are transformed to the standard form in terms of normal coordinates b_i corresponding to the linear natural modes of vibration $\tilde{\xi}_i$ at the static equilibrium position of the shell-panel as follows.

$$M\left(b_i\right)=b_{i,\tau\tau}+2\varepsilon_i\omega_i b_{i,\tau}+\omega_i^2 b_i+\sum_j\sum_k D_{ijk}b_j b_k+\sum_j\sum_k\sum_l E_{ijkl}b_j b_k b_l-p_d G_i\cos\omega\tau=0\ \ \left(i,j,k,l=1,2,3,...,I_{\mathrm{c}}\right) \tag{7}$$

Dynamic responses are calculated with the harmonic balance method and the numerical integration.

3. Results and Conclusion Analysis is conducted for the square cylindrical shell panel ($\beta=1$) with the curvature $\alpha_{\mathrm{x}}=4$ in the ξ direction without initial deflection ($\hat{a}_{mn}=0$). The maximum half-wave number is taken as 3 in the coordinate function, and the lowest 6 modes are adopted for the calculation of dynamic response, i.e. $I_{\mathrm{c}}=6$. In the following results, deflection is calculated at the position $\xi=0.1,\ \eta=0.1$, under the static load $p_{\mathrm{s}}=351$, and amplitude of periodic load $p_{\mathrm{d}}=500$. Damping ratio for the each mode is $\varepsilon_i=0.01$, and the spring constants of the elastic constraints are $k_{\mathrm{xm}}=k_{\mathrm{xp}}=k_{\mathrm{ym}}=k_{\mathrm{yp}}=0.01$. The initial in-plane displacement is applied only in the ξ direction. We consider two conditions as shown in Fig. 2 : (a) uniform compressive in-plane displacement $u_{0\mathrm{ms}}=-u_{0\mathrm{ps}}=5100$ and (b) compressive displacement including asymmetric component $u_{0\mathrm{ms}}=-u_{0\mathrm{ps}}=5100$, $-u_{0\mathrm{ma}}=u_{0\mathrm{pa}}=5100$.

Figure 3 shows the characteristics of restoring force of the panels with and without asymmetric compression under a concentrated lateral force. The restoring force shows the characteristics of a softening-and-hardening spring. By the asymmetric component of in-plane displacement, the region

where the negative gradient appears in the curve enlarged at the compressive side, and shortened at the tensile side of the panel. The nodal lines of the natural vibration modes of the panel are also deformed by the asymmetric constraints, as shown in Table 1.

Figures 4 and 5 shows the results of nonlinear frequency response of the shell-panels with and without asymmetric constraints, respectively. The thick rigid lines denote the periodic response calculated with the harmonic balance method. Although the principal resonance of the (1,1) mode corresponds to the characteristics of a softening-and-hardening spring, those of the higher modes (3,1) and (1,3) correspond to a hardening spring. By applying the asymmetric constraints, the principal resonance of the lowest mode shows more complex figure, and the hardening feature of the principal resonance of the mode (1,3) increases. Furthermore, the principal resonance of the mode (1,2) appears when the asymmetric constraints are applied which cannot be observed in the panel with uniform constraints.

In Figs. 4 and 5, the symbol C(1,1;1/2) denotes chaotic response accompanied with dynamics snap-through generated from sub-harmonic response of 1/2 order of the lowest vibration mode obtained by numerical integration. Fig. 6 shows the chaotic response of the panel with asymmetric constraints. The Fourier spectrum has dominant peak at the half frequency of the excitation. The Poincaré projection shows scattered fractal figure. The maximum Lyapunov exponent of the response has positive value of $\lambda_{\max} = 2.2$. Figs. 7(a) and (b) show the numerical results of Poincaré projection for each vibration mode of the panel with and without asymmetric constraints, respectively. Owing to the asymmetric constraints, contributions of asymmetric modes, such as (1,2) and (2,2), drastically increase.

References

(1) S. Maruyama, K. Nagai and Y. Tsuruta, "Modal interaction in chaotic vibrations of a shallow double-curved shell-panel", *Journal of Sound and Vibrations* 315 (2008) pp. 607-625.

(2) K. Nagai, S. Maruyama, T. Murata and T. Yamaguchi, Experiments and analysis on chaotic vibrations of a shallow cylindrical shell-panel, *Journal of Sound and Vibration* 305 (2007) pp. 492-520.

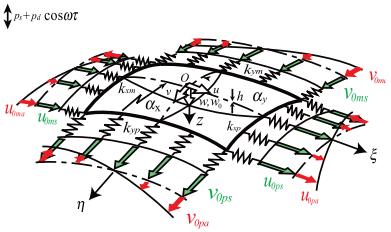

Fig.1 Model of a shell-panel

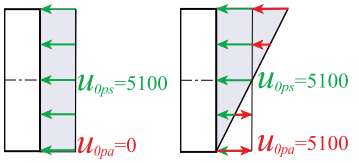

(a)Uniform (b)Asymmetric

Fig.2 In-plane compression

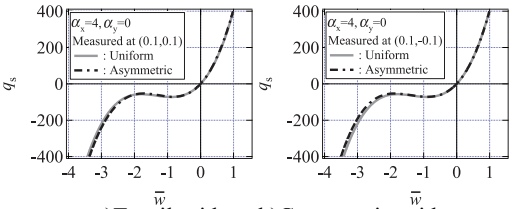

a)Tensile side b)Compressive side

Fig.3 Characteristics of restoring force

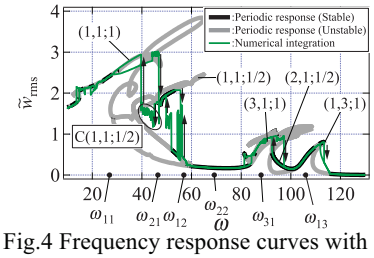

Fig.4 Frequency response curves with uniform compression

Table 1 Natural frequency and vibration mode

	Mode (m,n)	(1,1)	(2,1)	(1,2)	(2,2)	(3,1)	(1,3)
Uniform compression $u_{0ma}=-u_{0pa}=0$	ω_{mn}	26.9	46.4	56.9	69.2	88.1	106.0
	Modal pattern						
Asymmetric compression $u_{0ma}=-u_{0pa}=5100$	ω_{mn}	27.0	45.2	57.0	69.9	85.9	106.0
	Modal pattern						

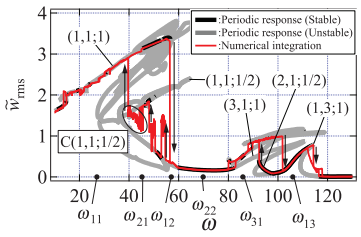

Fig5. Frequency response curves with asymmetric compression

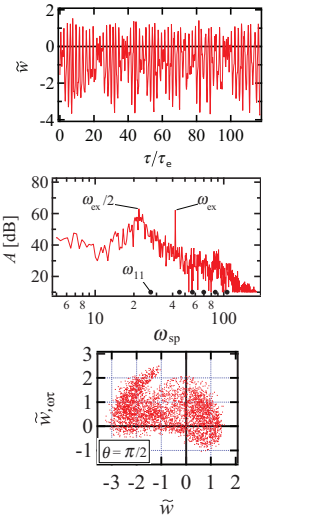

Fig.6 Chaotic response of the panel with asymmetric compression

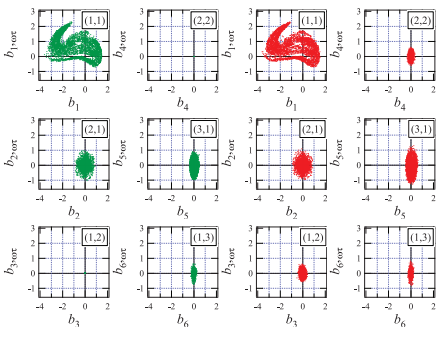

(a)Uniform (b)Asymmetric

Fig.7 Poincaré projection of each mode

Natural frequencies of a three-dimensional body using the Rayleigh-Ritz method and penalty parameters

Luis E. Monterrubio[1] and S. Ilanko[2]

[1]Department of Structural Engineering, University of California, San Diego , 9500 Gilman Drive, Mail Code 0085, La Jolla, CA 92093-0085, USA, Email: lemonterrubiosalaza@ucsd.edu

[2]School of Engineering, The University of Waikato, Hamilton, New Zealand.
Email: ilanko@waikato.ac.nz

The purpose of this paper is to present a Rayleigh-Ritz analysis to obtain the frequency parameters of a three-dimensional body in completely free condition and with constraints through the use of artificial springs. In the past, several researchers have presented vibration solutions of three-dimensional bodies including the work by Leissa and Zhang [1], Liew *et al* [2-3], Zhou *et al* [4-5] and Nagino *et al* [6].The motivation for this work comes from the following drawbacks of the classical Rayleigh-Ritz method: a) the need to used different sets of admissible functions to model elements with different boundary conditions, b) a limitation in the number of admissible functions due to ill-conditioning, and c) the limitation to solve problems defined by domains with simple geometries. Thus a set of admissible functions that models the structure in free condition, converges fast to the "exact solution" with respect to the number of functions included in the solution and that allows the use of a large number of functions without causing ill-conditioning is ideal for this approach. The latter characteristic is very important to be able to add a large number of artificial springs (penalty parameters) that reduce the number of degrees of freedom. It is also worth noting that structures in free condition are easy to inter-connect using the penalty method. A set of admissible functions with the properties mentioned above can be built by a linear and a square term plus a cosine series. This set of functions model a beam in a completely free condition and this set has been used together with penalty parameters to solve vibration and buckling problems of beams, plates, shells, frames built by two or more beams, structures built by shells of different curvature and box-type structures built by plate elements. Some of these examples can be found in [7-8]. The error due to violation of constraints has also been investigated using pairs of penalty parameters of positive and negative magnitude representing artificial springs or artificial inertia [7].

Here we take a similar approach as the one in [1] to define the displacements u, v and w along the x, y and z directions in the Rayleigh-Ritz analysis of a three dimensional element, but in this case the three-dimensional body of dimensions a, b and h is in completely free condition and its origin is located in one corner extending towards the positive directions of the x, y and z axes. Thus the displacements are defined as:

$$u(x,y,z,t)=U(x,y,z)\sin\omega t,\ v(x,y,z,t)=V(x,y,z)\sin\omega t \text{ and } w(x,y,z,t)=W(x,y,z)\sin\omega t \quad (1a,1b,1c)$$

where ω is the circular frequency and t is time and presenting the solution in non-dimensional form using non-dimensional coordinates of the three-dimensional body $\eta=x/a$ and $\chi=y/b$ and $\xi=z/h$,

$$U(\eta,\chi,\xi)=\sum_{i=1}^{I}\sum_{j=1}^{J}\sum_{k=1}^{K}A_{ijk}\phi_i(\eta)\phi_j(\chi)\phi_k(\xi),\ V(\eta,\chi,\xi)=\sum_{l=1}^{L}\sum_{m=1}^{M}\sum_{n=1}^{N}B_{lmn}\phi_l(\eta)\phi_m(\chi)\phi_n(\xi) \text{ and}$$

$$W(\eta,\chi,\xi)=\sum_{p=1}^{P}\sum_{q=1}^{Q}\sum_{r=1}^{R}C_{pqr}\phi_p(\eta)\phi_q(\chi)\phi_r(\xi), \qquad (2a,2b,2c)$$

and using the same number of functions $\overline{N}$ to simplify the solution $\overline{N}=I=L=P=J=M=Q=K=N=R$, and

$$\phi_{\bar{i}}(\eta)=(\eta)^{\bar{i}-1} \quad \text{for} \quad \bar{i}=i,l,p=1,2 \text{ and } 3,$$

$$\phi_{\bar{i}}(\eta)=\cos(\bar{i}-3)\pi\eta \quad \text{for} \quad \bar{i}=i,l,p=4,5,\ldots\overline{N}, \qquad (3a,3b,3c)$$

Similar equations are used in the other two non-dimensional coordinates. Carrying out the appropriate substitutions and minimizations of the terms defined in Eqs. (1-3) into the kinetic and strain energy terms of the three-dimensional body, (Eq. 6 and 7 in Leissa [1]), and into the strain energy of the artificial springs, (Eq. (33) in Nagino [6]), results in an eigenproblem. Three sets of results for frequency parameters of square ($a/b=1$) based three-dimensional bodies are presented. Tables 1 and 2 present results for bodies in free condition with height to side ratio $h/a=0.001$ and $h/a=0.5$, respectively. Table 3 presents results for a body with the four edges on the $z=0$ in clamped conditions. Results are compared with those of previous publications. Frequency parameters are defined as $\lambda=\omega b^2\sqrt{\rho h/D}$, where ρ is the density of the material and D is the flexural rigidity of the plates $D=Eh^3/12(1-\upsilon^2)$. In all cases the values of the poisson ratio υ was fixed to 0.3.

Table 1. Frequency parameters of a rectangular three-dimensional element in completely free condition with height to side ratio $h/a=0.001$.

	Frequency parameters [rad/s]					
$\overline{N}$	1	2	3	4	5	6
4	14.194	22.504	30.564	41.501	41.568	80.601
5	13.836	22.447	30.581	40.211	40.267	80.702
6	13.597	21.955	29.374	38.271	38.284	75.356
7	13.576	19.791	24.724	35.194	35.263	64.654
8	13.516	19.680	24.459	34.924	34.930	63.470
9	13.532	19.542	24.338	34.863	34.935	62.086
10	13.495	19.682	24.251	34.870	34.936	61.455
[7]	13.468	19.596	24.270	34.801	34.801	61.093

The results in Table 1 for a free body similar to a thin plate do not converge monotonically increasing the number of degrees of freedom, but that is due to geometrical parameters. Table 2 shows the results of a thick body in free condition with monotonic convergence as the value of $\overline{N}$ is increased. Table 3 shows the frequency parameters of the body with clamped edges at the base and the value of $\overline{N}$ fixed to ten. In this case, non-dimensional penalty parameters $\bar{k}=ka/E$ representing artificial springs (stiffness) were used to model all constraints, where k is the rigidity of the translational spring. Results on Table 3 show the typical monotonic convergence from below as the value of the penalty parameter of stiffness type $\bar{k}$ is increased. Results show that the set of admissible functions given in Eq. (3) can be used to model a three-dimensional body in free condition or constraint through the use of penalty parameters. More complex constraints and inter-connection of elements can be also modeled using the penalty method.

Table 2. Frequency parameters of a rectangular three-dimensional element in completely free condition with height to side ratio $h/a = 0.5$.

	Frequency parameters [rad/s]					
$\overline{N}$	1	2	3	4	5	6
4	8.835	13.342	16.299	16.658	18.029	18.029
5	8.822	12.548	15.036	16.117	17.062	17.062
6	8.787	12.523	14.973	16.080	17.041	17.041
7	8.786	12.518	14.967	16.075	17.033	17.033
8	8.782	12.516	14.964	16.074	17.032	17.032
9	8.781	12.515	14.963	16.073	17.031	17.031
10	8.781	12.515	14.962	16.073	17.030	17.030
11	8.780	12.515	14.962	16.073	17.030	17.030
[6]	8.780	12.515	14.961	16.072	17.030	17.030

Table 3. Frequency parameters of a rectangular 3-D element with edges clamped at the base, $h/a = 0.5$, $\overline{N} = 10$ and different values of non-dimensional penalty parameters $\overline{k}$ as defined in [6].

	Frequency parameters [rad/s]					
$\overline{k}$	1	2	3	4	5	6
10^3	15.278	24.060	24.060	24.773	24.773	29.344
10^4	15.313	24.094	24.094	24.835	24.835	29.375
10^5	15.316	24.098	24.098	24.841	24.841	29.379
10^6	15.317	24.098	24.098	24.841	24.841	29.379
[6]	15.286	24.071	24.071	24.816	24.816	29.376

Acknowledgement
The authors wish to acknowledge the financial support from the Marsden Fund (http://www.royalsociety.org.nz/programmes/funds/marsden/).

References

[1] Leissa A. and Zhang Z. 1983 On the three-dimensional vibrations of cantilevered rectangular parallelepiped, *J. Acoust. Soc. Am.* **73**, 2013-2021.

[2] Liew K.M., Hung K.C. and Lim M.K. 1993 A continuum three-dimensional vibration analysis of thick rectangular plates, *Int. J. Solids Structures* **30**, 3357-3379.

[3] Liew K.M., Hung K.C. and Lim M.K. 1994 Three dimensional vibration of rectangular plates: variance of simple support conditions and influence of in-plane inertia, *Int. J. Solids Structures* **31**, 3233-3247.

[4] Zhou D., Cheung Y.K., Au F.T.K. and Lo S.H. 2002 Three-dimensional vibration analysis of thick rectangular plates using Chebyshev polynomial and Ritz method, *Int. J. Solids Structures* **39**, 6339-6353.

[5] Zhou D., Cheung Y.K., Au F.T.K. and Lo S.H. 2004 Three-dimensional vibration analysis of rectangular thick plates on Pasternak foundation, *Int. J. Numer. Meth. Engng*. **59**, 1313–1334.

[6] Nagino H., Mikami T. and Mizusawa T. 2008 Three-dimensional free vibration analysis of isotropic rectangular plates using the B-spline Ritz method, *J. Sound Vib*. **317**, 329–353.

[7] Monterrubio L.E.and Ilanko S. 2012 Sets of Admissible Functions for the Rayleigh-Ritz Method, *Proceed. Eleventh Intl. Conf .Comp. Struct. Tech.*, Paper 97.

[8] Monterrubio L.E. 2012 Frequency and buckling parameters of box-type structures using the Rayleigh–Ritz method and penalty parameters, Comp. & Struct. **104–105**, 44–49.

Analysis and Lay-up Optimization for Vibration of Laminated Composite Plate with Rigid Body Attachments

Yoshihiro NARITA*[1], Shinya HONDA*[1] and Takahiro FUNAMIZU*[2]

*[1] Faculty of Engineering, Hokkaido University,
N13W8, Kita-ku, Sapporo, Hokkaido, 060-8628, Japan, narita@eng.hokudai.ac.jp
*[2] Graduate School of Engineering, Hokkaido University

1. Introduction

The vibration of plates with various attachments, such as spring, point mass and dashpot, has received considerable attention in the past literature, since such applications are found in many engineering structures. This technical trend is getting more obvious by the appearance of smart structures, where sensors and actuators are attached to the plate surfaces. The effect of the attachments has been studied on the vibration characteristics for cases of springs and masses, but very little has been done on the plates with *long* rigid attachments.

The objective of this work is to analyze the free vibration of laminated composite rectangular plates with single or plural rigid bodies attached on the plate surface. The Ritz method is applied to the problem by introducing rotational inertia of the long rigid body in the energy formulation of the plate. The plate is assumed to be symmetrically laminated with respect to the mid-surface. An experiment is also conducted to make the comparison between the analytical and experimental results.

A lay-up optimization problem is then solved by using a layerwise optimization method, and in numerical examples, the optimum lay-up designs are determined to make the maximum fundamental frequencies of the laminated plate-rigid body system.

2. Analysis of laminated rectangular plate with rigid body

Figure 1 shows a laminated composite rectangular plate of dimensions $a \times b$ with thickness h, having some bar-like rigid bodies (p=1,2,…,P). A Cartesian coordinate system o-xy is taken with its origin at the center of the plate. The direction of the fibers and the transverse direction to the fibers are denoted by L and T, respectively, and the fiber orientation angle between the axes is denoted by θ. Each layer is considered to be macroscopically orthotropic. Symmetrically laminated plate with even numbers of layer is considered in the present work and the total number of layers is defined as $2N$.

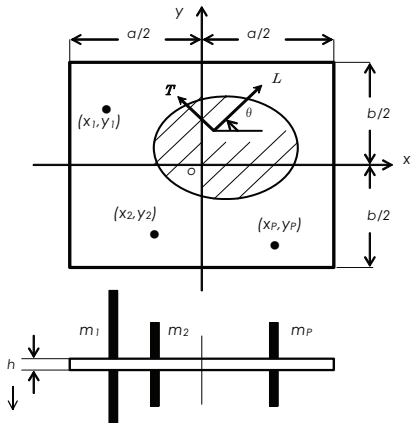

Fig.1 Laminated plate with symmetrically attached bars

The bending stiffness which relates the stress resultant to the plate curvature is given in the lamination theory. For small amplitude vibration, the strain and kinetic energies are written in terms of deflection w by

$$U = \frac{1}{2}\iint_A \{\kappa\}^T \begin{bmatrix} D_{11} & D_{12} & D_{16} \\ D_{12} & D_{22} & D_{26} \\ D_{16} & D_{26} & D_{66} \end{bmatrix} \{\kappa\} dA \quad \text{with} \quad \{\kappa\} = \left\{ -\frac{\partial^2 w}{\partial x^2} \quad -\frac{\partial^2 w}{\partial y^2} \quad -2\frac{\partial^2 w}{\partial x \partial y} \right\}^T \tag{1}$$

$$T=\frac{1}{2}\rho h\iint_A\left(\frac{\partial w}{\partial t}\right)^2 dA+\frac{1}{2}\sum_{p=1}^{P}\left[m_p\left(\frac{\partial w}{\partial t}\right)^2+I_{x,p}\left\{\frac{\partial}{\partial t}\left(\frac{\partial w}{\partial x}\right)\right\}^2+I_{y,p}\left\{\frac{\partial}{\partial t}\left(\frac{\partial w}{\partial x}\right)\right\}^2\right] \quad (2)$$

where D's are bending stiffness, m_p, and $I_{x,p}$, $I_{y,p}$ are translational and rotational inertia of the attached rigid bodies, respectively. Natural frequency is normalized as a frequency parameter $\Omega=\omega a^2(\rho/D_0)^{1/2}$ with $D_0=E_T h^3/12(1-\nu_{LT}\nu_{TL})^{1/2}$ where ω is a radian frequency, ρ is the averaged mass per unit area and D_0 is a reference bending stiffness.

After the displacement function is substituted into the functional composed of eqs.(1) and (2), the Ritz minimizing process is applied to yield a frequency equation. The frequency parameter for the fundamental (lowest) mode, denoted by Ω_1, is used later as the object function and is maximized in the optimization.

3. Lay-up optimization for the maximum fundamental frequency

The objective function to be maximized is the fundamental frequency parameter Ω_1, and the design variables are the fiber orientation angles θ_i (i = 1, 2, … , N) where θ_1 is the angle in the outermost layer. To solve this optimization problem, the present paper employs the layerwise optimization (LO) scheme, and the LO method is based on the well known physical fact that the outer layer has a stronger stiffening effect than the inner layers and plays a larger role in the natural frequency of bending vibration. This suggests that the outer layer plays the decisive role in determining the maximum frequency of laminated plates. The effectiveness of the LO method was already shown in a number of papers by the present authors.

Table 1 Comparison of the lowest four frequencies.

(Aluminum plate WITHOUT rigid body)

	1st	2nd	3rd	4th
Ritz	56.62	186.9	350.8	633.8
Measured	50.24	180.4	322.7	608.2

(Aluminum plate WITH rigid body)

	1st	2nd	3rd	4th
Ritz	32.40	66.67	117.7	302.6
Measured	29.92	64.86	110.8	305.7

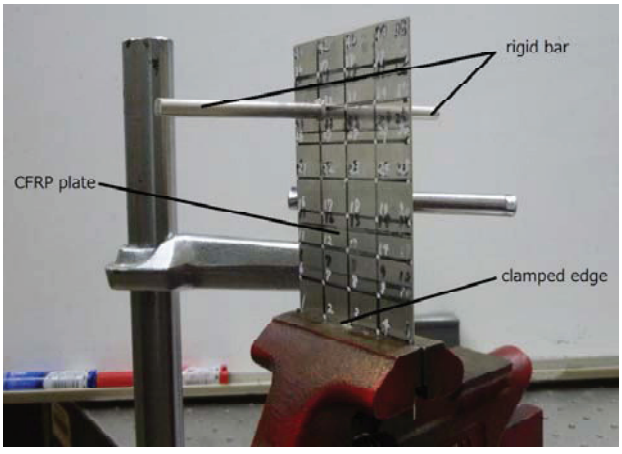

Fig. 2 Test specimen for the experiment.

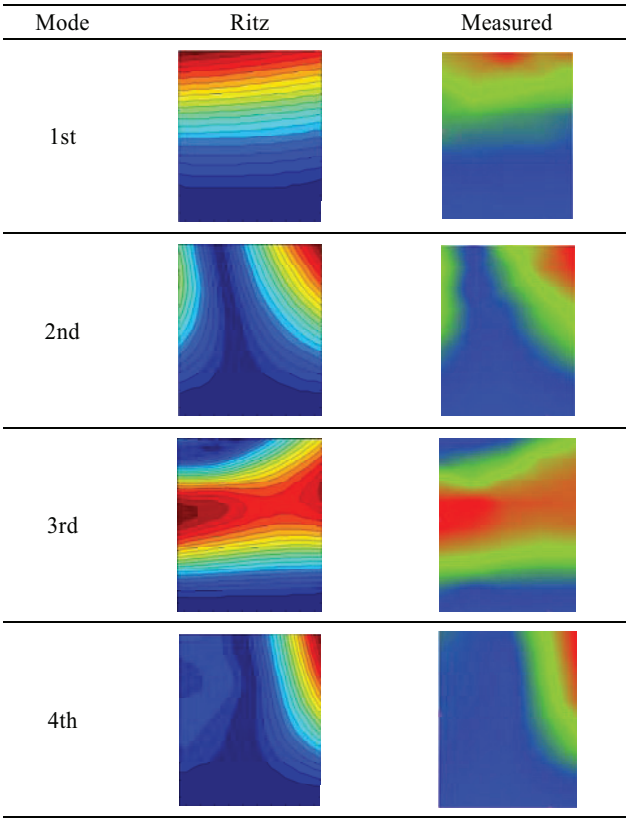

Fig. 3 The lowest four vibration mode shapes from the Ritz method and the experiment.

4. Comparison of analytical and experimental results

As shown in Fig.2, an experiment is conducted to verify the validity of analytical modeling for aluminum cantilever plates with/without a rigid aluminum bar by using the modal analysis technique. The plate is set to stand vertically by a vise and has the free edge dimension of 120×80×0.95 mm except the part fixed by the vise. The rigid bar has the total length of 160 mm with a radius of 3.5 mm, and attached symmetrically to the plate. For measuring the natural frequencies and mode shapes, the plate is excited at many points by an impact hammer, and the acceleration is measured by the piezoelectric accelerometer.

Table 1 presents the lowest four natural frequencies (Hz) obtained by the Ritz method and experiment for the plates with/without a rigid body. The difference of the Ritz and experimental results is between 3.5 and 11.3 percent for a plate without a bar, and is between -1.0 and 7.7 percent for the plate with a bar, and no significant difference is found between the two plates. The Ritz method gives higher estimated frequencies than the experimental ones, except for the fourth mode of the plate with a bar, mainly due to the less perfect clamping that the vise would apply.

Figure 3 illustrates the mode shapes of the plate with a bar, and the effect of the bar is observed when the mode shapes are compared with those of the plate without a bar. It is clearly seen from these results that the modeling and formulation of the problem are reasonably accurate for the present problem.

For the lay-up optimization, Table 2 presents randomly chosen parameters for comparison with the optimum results of the symmetrically laminated eight-layer, cantilever plate with a rigid body. The plates are assumed to have the rigid body of length $2l$, mass m and radius r, and the parameters are defined as $\alpha = a/b$, $\beta = a/l$, $\gamma = a/r$, $\mu = m/\rho abh$ with the non-dimensional location of the bar at $\xi = 2x/a$ and $\eta = 2y/b$.

In Table 3, the optimum solution is compared with the results of A, B, C and D cases for the lay-up design and the fundamental frequencies. Under the conditions listed in Table 2, the obtained optimum solutions are [5°/5°/50°/-35°]s, [0°/0°/0°/0°]s, [0°/0°/-5°/-5°]s, [0°/0°/0°/-5°]s in the upper (lower) layers. The optimum solutions obtained by the layerwise optimization are higher than the other results. It is concluded that the optimum fiber orientation angles are influenced by the present of the bar, while the optimum lay-up is always [0°/0°/0°/0°]s for the cantilever plates without bar, regardless of the aspect ratios. **References (omitted)**

Table 2 Selected parameters for the optimization problem.

Case	α	β	γ	μ	ξ	η
A	0.5	1.0	30	1.0	0.5	0.5
B	1.0	3.0	15	0.2	-0.3	0.4
C	3.0	2.0	10	0.5	0.1	-0.2
D	5.0	1.5	5	0.8	-0.8	-0.7

Table 3 Obtained natural frequencies of the plates with optimum lay-ups and typical lay-ups for each case.

Case	A	B	C	D
Optimum	4.12	13.41	10.93	13.35
$[0°/0°/0°/0°]_s$	3.85	13.41	10.92	13.34
$[45°/-45°/45°/-45°]_s$	2.99	7.12	5.29	6.11
$[0°/90°/0°/90°]_s$	3.72	11.30	9.20	11.20

Vibrations of Carbon Nanotubes: nonlinear models and energy distribution

F. Pellicano†, M. Strozzi†, L. I. Manevitch‡

† Dept. of Engineering "Enzo Ferrari", University of Modena and Reggio Emilia, Modena, Italy. email: francesco.pellicano@unimore.it, matteo.strozzi@unimore.it
‡ N.N. Semenov Institute of Chemical Physics, Russian Academy of Sciences, Moscow, Russia. email: manevitchleonid3@gmail.com

Abstract
Vibrations of Single-Walled Carbon Nanotubes for various boundary conditions are considered in the framework of the Sanders-Koiter thin shell theory. A double series expansion of displacement fields, based on the Chebyshev orthogonal polynomials and harmonic functions, is used to analyse numerically the natural frequencies of shells having free or clamped edges. A reduced form of the Sanders-Koiter theory is developed by assuming small circumferential and shear deformations; such approach allows to determine an analytical solution for the natural frequencies.
The numerical model is validated with the results of molecular dynamics and finite element analyses present in literature. The analytical model is validated by means of comparisons with the numerical approach. Nonlinear vibrations and energy distribution of carbon nanotubes are then considered.

Introduction
Carbon Nanotubes were discovered in 1991 by Iijima [1], who first analysed the synthesis of molecular carbon structures in the form of fullerenes and then reported the preparation of a new type of finite carbon structure consisting of needle-like tubes, the carbon nanotubes, described as helical microtubules of graphitic carbon.
Rao et al. [2] studied the vibrations of SWNTs by using Raman scattering experimental techniques with laser excitation wavelengths in the range of the nanometers. They observed numerous Raman peaks, which correspond to vibrational modes of the nanotubes.
Bandow et al. [3] analysed the effect of the temperature on the diameter distribution and chirality of SWNTs by comparing different experimental techniques, such as electron microscopy, X-ray diffraction and Raman spectroscopy. They studied the effect of the catalysts on the tube yield and the evolution of the tube distribution with increasing environment temperature.
Jorio et al. [4] studied the vibrations of SWNTs by resonant confocal micro-Raman spectroscopy. They developed a method to assign the carbon nanotube chirality uniquely by measuring one radial breathing mode frequency and applying the theory of resonant transitions.
Molecular dynamics (MD) simulations and finite element (FE) analyses provide good predictions of the mechanical behaviour of CNTs under external forces, with results close to the experiments. However, such techniques are not suitable for considering nonlinear effects due to their very huge computational cost.
In this paper, a semi-analytical approach is proposed for the study of carbon nanotubes vibrations; this method is computationally efficient, accurate and suitable for considering nonlinear effects.

Theory
According to the Sanders-Koiter theory, the elastic strain energy U of a cylindrical shell, neglecting both the transverse normal stress σ_z (plane stress hypothesis) and the transverse shear strains γ_{xz}, $\gamma_{\theta z}$ (Kirchhoff's hypothesis), as in the Love's "first approximation", is written in the form

$$U = \frac{1}{2} LR \int_0^1 \int_0^{2\pi} \int_{-h/2}^{h/2} \left(\sigma_x \varepsilon_x + \sigma_\theta \varepsilon_\theta + \tau_{x\theta} \gamma_{x\theta} \right) dz d\theta d\eta \qquad (1)$$

The kinetic energy T of a cylindrical shell (rotary inertia effect is neglected) is given by

$$T = \frac{1}{2}\rho hLR \int_0^1 \int_0^{2\pi} \left(\dot{u}^2 + \dot{v}^2 + \dot{w}^2 \right) d\theta d\eta \tag{2}$$

Here, the three displacement fields (u, v, w) are nondimensionalized by means of the radius R of the carbon nanotube $u = R\tilde{u}$, $v = R\tilde{v}$, $w = R\tilde{w}$. A nondimensional time τ is considered by introducing a reference natural frequency ω_0 in the following form $t = \omega_0^{-1}\tau$, $\omega_0 = \sqrt{\frac{E}{(1-\nu^2)\rho R^2}}$.

The problem is analysed by means of an approach based on a double series expansion in terms of harmonic functions and polynomials followed by the application of the Rayleigh-Ritz procedure. Once the linear analysis is carried out, the displacement fields are re-expanded by means of approximate eigenfunctions; using the Lagrange equations and the potential energy with nonlinear terms, a set of nonlinear ordinary differential equations is obtained and solved numerically.

Numerical results

First of all the model is validated with experimental data present in literature [4]; the results reported in Table 1 show that the model is sufficiently accurate.

Natural frequency (THz)			Difference %
(r, s)	ESKT – Present model	RRS – Ref. [4]	
(8, 7)	6.905	7.165	3.63
(10, 5)	6.785	7.105	4.50
(11, 4)	6.669	6.865	2.85
(14, 1)	6.177	6.295	1.87
(18, 0)	5.025	5.276	4.76

Table 1. Natural frequencies of the radial breathing mode (m = 0, n = 0): comparisons between the extended Sanders-Koiter theory (ESKT) and the Resonant Raman Spectroscopy (RRS).

In order to analyse the discrete molecular carbon nanotubes as continuum thin shells, equivalent mechanical parameters (Young's modulus, Poisson's ratio, mass density, wall thickness) must be considered. These parameters are not dependent from the CNT diameter (no size effect). The carbon nanotube described in Table 2 is considered for the following computations.

Effective thickness h_0 (nm)	0.10 ÷ 0.15
Equivalent thickness h (nm)	0.066
Effective Young's modulus E_0 (TPa)	1.0 ÷ 2.0
Equivalent Young's modulus E (TPa)	5.5
Effective Poisson's ratio ν_0	0.12 ÷ 0.28
Equivalent Poisson's ratio ν	0.19
Surface density of graphite σ (kg/m^2)	7.718×10^{-7}
Equivalent mass density ρ (kg/m^3)	11700

Table 2. Effective and equivalent parameters of the Single-Walled Carbon Nanotube.

In Figure 1 the first three mode shapes of a free-free carbon nanotube are presented, such modes are then considered for the development of the semi-analytic nonlinear model of the nanotube in the re-expansion procedure. In Figure 2 the total vibration energy distribution is represented, the nanotube is unwrapped on a plane in order to allow the representation. The sequence of Figures 2(a-d) shows the development of the total energy density [Jm^{-2}] during a time period corresponding to the natural frequency of the fundamental mode; clearly, due to the presence of the nonlinearity, one can observe the absence of periodicity. It is to note that the damping is not considered here, so the total energy

should be constant (the integral of the density over the surface); a specific check is carried out, the results are omitted for the sake of brevity.
The analysis of the energy distribution over the shell shows a periodicity along the circumferential direction. This is partially expected as in the present preliminary analysis no conjugate modes are present. The energy is initially distributed non symmetrically in the axial direction, see Figure 2a, indeed here we are combining a symmetric mode (0,2) and an asymmetric mode (1,2). Then, such initial distribution is destroyed due to nonlinearity and the energy evolves in a mode more complex pattern, see Figures 2(b-e).

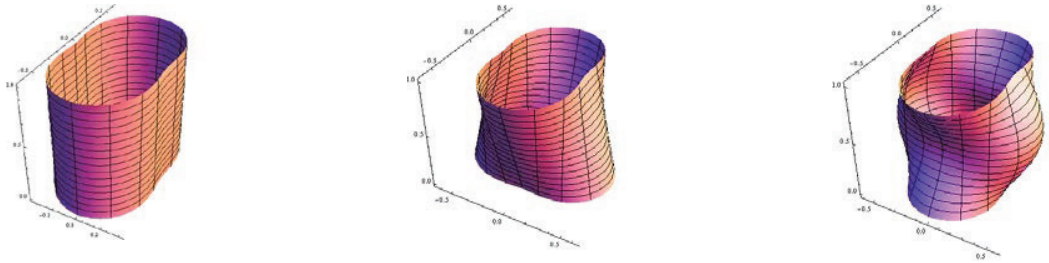

Figure 1. Mode shapes of the vibration modes (j, n). (a) Mode (0, 2). (b) Mode (1, 2). (c) Mode (2, 2).

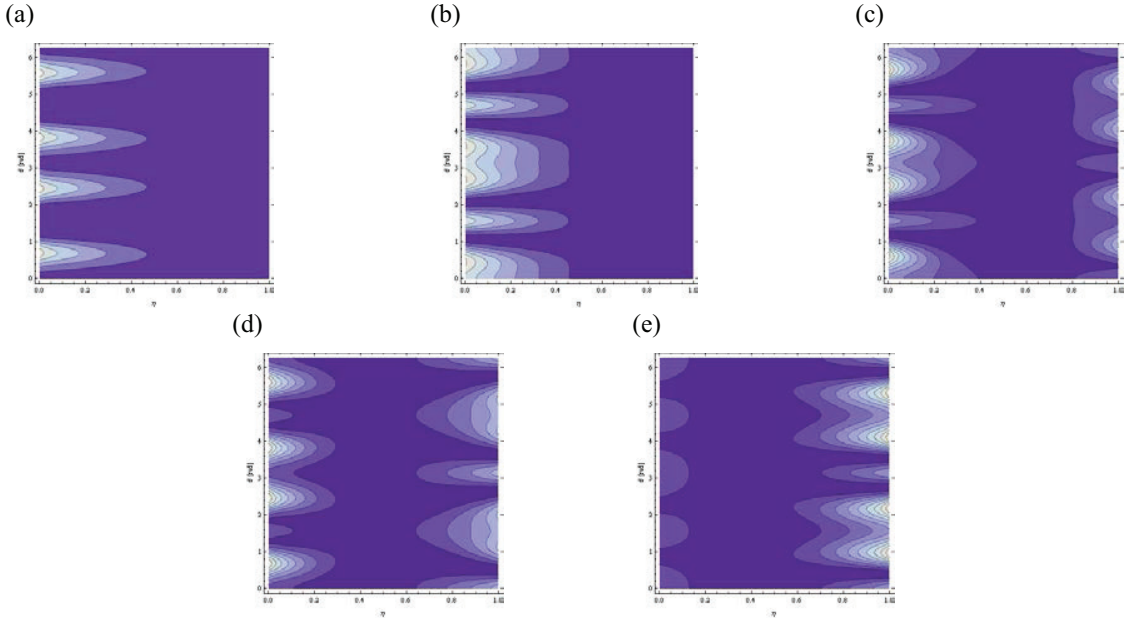

Figure 2. Contour plots of the total energy distribution $\tilde{E}$ (η, θ, τ). Combination of the vibration modes (0, 2) and (1, 2). (a) Time τ = 0. (b) Time τ = 1/4. (c) Time τ = 1/2. (d) Time τ = 3/4. (e) Time τ = 1.

References

[1] Iijima S. Helical microtubules of graphitic carbon. *Nature* 354 (1991) 56-58.
[2] Rao AM, Richter E, Bandow S, Chase B, Eklund PC, Williams KA, Fang S. Diameter-Selective Raman Scattering from Vibrational Modes in Carbon Nanotubes. *Science* 275 (1997) 187-191.
[3] Bandow S, Asaka S, Saito Y. Effect of the Growth Temperature on the Diameter Distribution and Chirality of Single-Wall Carbon Nanotubes. *Physical Review Letters* 80 (1998) 3779-82.
[4] Jorio A, Saito R, Hafner J, Lieber CM. Structural Determination of Isolated Single-Wall Carbon Nanotubes by Resonant Raman Scattering. *Physical Review Letters* 86 (2001) 1118-21.

AEROELASTICITY ANALYSIS OF ROTOR BLADES OF AXIAL COMPRESSOR IN THE CASE OF PARTIALLY BLOCKED ENGINE INLET

Romuald Rzadkowski

Department of Aeroelasticity, Institute of Fluid Flow Machinery,

Polish Academy of Sciences,

J. Fiszera st., 14, Gdansk, 80 952 Poland

E-mail: z3@imp.gda.pl

INTRODUCTION

Foreign objects entering aircraft engines are a perennial problem. Mathematical analysis and computer simulations can provide information on component stresses already in the design phase.

Foreign objects (e.g. a bird) were characterized as a water-like hydrodynamic response by Wilbeck and Rand [1] in their tests. Storace et al. [2] developed a computer program to predict structural response due to soft body impact. Heidari, Carlson and Yantis [3] developed rotor dynamics as a nonlinear transient analysis for a propulsion system during bird strike induced fan blade loss. Experiments were carried out on SO-3 compressor first stage rotor blades [4] to initiate a crack by placing rectangular blocks on the stator blades, simulating birds engulfed in the engine.

The Fluent code was used to analyze the low frequency excitation caused by inlet blockage of 1.5 stages of an SO-3 engine, but it did not take into account rotor blade vibration Rzadkowski et al. [5], Soliński et al.[6]. Aeroeleastic behaviour of rotor blade 1.5 first compressor stage was analyzed by Rzadkowski et al. [7].

In this paper the unsteady forces acting on rotor blades will be calculated for a 3D non-viscous ideal gas flow through 2.5 compressor stages using an in-house code and taking into account rotor blade vibration.

AERODYNAMICAL MODEL

Blade failures in the first stage of SO-3 compressors were reported in the years 1975-1991 [4]. Experiments were carried out on a first stage rotor blade in an SO-3 engine compressor at the Air Force Institute of Technology in Warsaw to initiate a crack by placing rectangular blocks on the stator blades, which in real life could be caused by birds engulfed in the engine.

The 3D transonic flow of an inviscid non-heat conductive gas through the first compressor stages of an SO-3 aircraft engine was simulated.

In order to model the engine inlet bird strike, four stator blade passages were blocked. Each of the passages is meshed, using an H-type grid for the stators domain and a hybrid H-H grid for the rotor domain ([8], [9], [10]). Here the outer H-grid of the rotor remains stationary during the calculation, while the inner H-grid is rebuilt in each iteration by a given algorithm, so that the external points of the inner grid remain unmoved, but the internal points (on the blade surface) move according to the blade motion. Mesh dependency concerning the fluid-flow and mesh size was analysed in [9], [10].

The spatial transonic flow, including in the general case strong discontinuities in the form of shock waves and wakes behind the exit edges of blades is written in the relative Cartesian coordinate system rotating with constant angular velocity ω according to full non-stationary Euler equations, presented in the form of integral conservation laws of mass, impulse and energy [8], [9]. Wakes were not simulated.

In the general case, when axial velocity is subsonic, at the inlet boundary initial values for total pressure, total temperature and flow angles are used, while at the outlet boundary only the static pressure has to be imposed. Non-reflecting boundary conditions must be used, i.e., incoming waves (three at the inlet, one at the outlet) have to be suppressed, which is accomplished by setting their time derivative to zero [9], [10].

On the blade's surface, because the grid moves with the blade, the normal relative velocity is set to zero.

STRUCTURAL MODEL

The blade vibration formulation is based on a modal approach of the coupled problem ([11], [12]). The first step of the modal approach consists of solving the problem of the natural mode shapes and eigenvalues without damping and in a vacuum. Then the displacement of each blade can be written as a linear combination of the first *N* mode shapes with the modal coefficients depending on time.

NUMERICAL RESULTS

The numerical calculations were carried out for the two and half stages of the SO-3 engine compressor.

The blade vibration was defined by taking into account the first five natural mode shapes of the rotating R1 and R2 blades. Mechanical damping was not taken into consideration, because we did not have experimental values. Aerodynamical damping was part of the calculation process [10].

The calculation included two regimes. In the first regime the calculations of the unsteady flow through the turbine stage were made by first taking into account the rotor rotation without blade vibration. Next the blades vibration began.

In the numerical model R1 and R2 rotor blade vibrations were taken into consideration, hence an aeroelastic analysis was possible.

A comparison between the vibration of rotor blades with and without a blocked inlet is discussed.

CONCLUSIONS

This paper has presented the calculation results for unsteady low-frequency aerodynamic forces acting on SO-3 jet engine compressor R1 and R2 blades, which took into account blade vibration. The forces were analyzed in two operating conditions: with an unblocked and partially blocked engine inlet. The obtained results show that disturbances in the engine inlet strongly influence the level of unsteady forces acting on the rotor blades. With a partially blocked inlet the whole spectrum of low-frequency harmonics was observed, including the natural frequency of blades.

The vibration amplitudes of rotor blades with a blocked inlet are considerably higher than in the case of an unblocked inlet. In this case R1 and R2 blade vibrations differ from their first mode shape and include torsional components.

ACKNOWLEDGMENTS

The authors wish to acknowledge NCBiR (project PBS1/B4/5/2012) for the financial support of this work.

All numerical calculations were made at the Academic Computer Centre TASK (Gdansk, Poland).

REFERENCES

[1] Wilbeck, J. S. and Rand, J. L., The Development of a Substitute Bird Model, Journal of Engineering for Power, ASME, vol. 103, p. 725, 1981.

[2] Storace, A. F., Nimmer, R. P. and Ravenhall, R., Analytical and Experimental Investigation of Bird Impact on Fan and Compressor Blading. Journal of Aircraft, Vol. 21, July 1984.

[3] Heidari, M. A., Carlson, D. L. and Yantis, T., Rotor-dynamics Analysis Process, p.3601, Worldwide Aerospace Conference & Technology Showcase, April 8 - 10, Toulouse, 2002.

[4] Szczepanik, R., Experimental Analysis of Rotor Blades of Aircraft Engines in Various Operating Conditions, DSc Thesis, ITWL Warsaw, (in Polish) 2010.

[5] Rzadkowski, R., Solinski, M., Szczepanik, R., The Unsteady Low-Frequency Aerodynamic Forces Acting on the Rotor Blade in the First Stage of an Jet Engine Axial Compressor, Advances in Vibration Engineering, 11(2), 193-204, 2012.

[6] Solinski, M., Rzadkowski, R., Pajak, A., Szczepanik, R., The Unsteady Low-Frequency Forces Acting on the Rotor Blade in the First Stage on an Axial Compressor of SO-3 Jet Engine, Proceedings of the 8th International Conference on Vibration Engineering and Technology of Machinery, VETOMAC –VIII, p. 277-278, Gdansk, Sept 3-6, 2012.

[7] Rzadkowski, R., Gnesin, V., Kolodyazhnaya, L., Szczepanik, R., Aeroelastic Behaviour of First Stage Compressor Rotor Blades with Foreign Object in Engine Inlet, *ISUAAAT'2012, 13TH International Symposium on Unsteady Aerodynamics, Aeroacustics and Aeroelasticity of Turbomachines*, Tokyo, 10-15 Sept, 2012.

[8] Godunov, S., K. et al., Numerical Solution of Multidimensional Problems in Gasdynamicse, Nauka, Moskva, 1976, (in Russian).

[9] Rzadkowski, R., Gnesin, V., 3D Unsteady Forces of the Transonic Flow Through a Turbine Stage with Vibrating Blades, ASME Paper GT-2002-300311, ASME TURBOEXPO 2002, Amsterdam, (June 3-6, 2002) 2002.

[10] Gnesin, V., Kolodyazhnaya, L., Rzadkowski, R., A Numerical Model of Stator-Rotor Interaction in a Turbine Stage with Oscillating Blades, Journal of Fluids and Structures, 19(8), 1141-1153, 2004.

[11] Bathe, K., Wilson, E, Numerical Methods in Finite Element Analysis, Prentice-Hall, Inc Englewood Cliffs, New Jersey, 1976.

[12] Rzadkowski, R., Dynamics of Steam Turbine Blading, Part Two Bladed Discs, Ossolineum, Wrocław-Warszawa, 1998.

VIBRATION ANALYSIS OF LAMINATED DOUBLY-CURVED SHELLS AND PANELS USING HIGHER-ORDER EQUIVALENT-SINGLE-LAYER AND LAYER-WISE THEORIES

Francesco Tornabene*, Nicholas Fantuzzi*, Erasmo Viola*

* DICAM - Department, University of Bologna,
Viale del Risorgimento 2, 40136 Bologna, Italy
e-mail: francesco.tornabene@unibo.it, nicholas.fantuzzi@unibo.it, erasmo.viola@unibo.it
web page: http://software.dicam.unibo.it/diqumaspab-project

Key words: Doubly-Curved Shells, Higher-Order Equivalent-Single-Layer Theory, Layer-Wise Theory, Composite Laminates, Generalized Differential Quadrature.

ABSTRACT

An accurate determination of the modal parameters is required for the technical design of structural shell elements. In this study, the free vibrations of laminated doubly-curved shells are investigated. There are three different ways to study anisotropic shell structures: the 3D Elasticity [1-3], Equivalent-Single-Layer (ESL) [1-3] and Layer-Wise (LW) [3,4] theories. The mechanical model proposed in this study, for the two ESL and LW approaches, is based on the Carrera's Unified Formulation (CUF) [4]. The investigated kinematic models are presented in the following:

$$\text{LD4 model}\begin{cases} U_1^{(k)} = F_b u_{1b}^{(k0)} + F_1 u_1^{(k1)} + F_2 u_1^{(k2)} + F_3 u_1^{(k3)} + F_t u_{1t}^{(k4)} \\ U_2^{(k)} = F_b u_{2b}^{(k0)} + F_1 u_2^{(k1)} + F_2 u_2^{(k2)} + F_3 u_2^{(k3)} + F_t u_{2t}^{(k4)} \\ U_3^{(k)} = F_b u_{3b}^{(k0)} + F_1 u_3^{(k1)} + F_2 u_3^{(k2)} + F_3 u_3^{(k3)} + F_t u_{3t}^{(k4)} \end{cases} \qquad \text{EDZ4 model}\begin{cases} U_1 = u_1^{(0)} + \zeta u_1^{(1)} + \zeta^2 u_1^{(2)} + \zeta^3 u_1^{(3)} + \zeta^4 u_1^{(4)} + (-1)^k z_k u_1^{(5)} \\ U_2 = u_2^{(0)} + \zeta u_2^{(1)} + \zeta^2 u_2^{(2)} + \zeta^3 u_2^{(3)} + \zeta^4 u_2^{(4)} + (-1)^k z_k u_2^{(5)} \\ U_3 = u_3^{(0)} + \zeta u_3^{(1)} + \zeta^2 u_3^{(2)} + \zeta^3 u_3^{(3)} + \zeta^4 u_3^{(4)} + (-1)^k z_k u_3^{(5)} \end{cases} \quad (1)$$

$$\text{ED4 model}\begin{cases} U_1 = u_1^{(0)} + \zeta u_1^{(1)} + \zeta^2 u_1^{(2)} + \zeta^3 u_1^{(3)} + \zeta^4 u_1^{(4)} \\ U_2 = u_2^{(0)} + \zeta u_2^{(1)} + \zeta^2 u_2^{(2)} + \zeta^3 u_2^{(3)} + \zeta^4 u_2^{(4)} \\ U_3 = u_3^{(0)} + \zeta u_3^{(1)} + \zeta^2 u_3^{(2)} + \zeta^3 u_3^{(3)} + \zeta^4 u_3^{(4)} \end{cases} \qquad \text{FSDT model}\begin{cases} U_1 = u_1^{(0)} + \zeta u_1^{(1)} \\ U_2 = u_2^{(0)} + \zeta u_2^{(1)} \\ U_3 = u_3^{(0)} \end{cases}$$

The LD4 model of the expressions (1) refers to a fourth order Layer-Wise approach in terms of displacements (LD4), where the generalized displacements $u_{ib}^{(k\tau)}, u_{it}^{(k\tau)}, u_i^{(k\tau)}$ are defined at the k-th layer level and the thickness functions F_b, F_1, F_2, F_3, F_t are assumed as Legendre polynomials [4]. The other three model EDZ4, ED4 and FSDT can be classified as fourth order Equivalent Single Layer models in terms of displacements with (EDZ4) or without (ED4) the zig-zag effect (Z). In particular, the last one of the expressions (1) is the well-known First-order Shear Deformation Theory (FSDT). The curvature effect is included in the formulation of the constitutive equations. The fundamental operators, concerning a laminated composite doubly-curved shell in orthogonal curvilinear coordinate system, are obtained for the first time by the authors. Using the Differential Geometry [1,2] to completely describe the doubly-curved shell, the Differential Quadrature (DQ) [5] rule leads to numerically evaluate all the derivatives involved in the numerical calculations. The governing equations are expressed as functions of various kinematic parameters, when the constitutive and the kinematic relationships are used [6-11]. The system of second-order linear partial differential

equations is solved considering the Generalized Differential Quadrature (GDQ) method [5]. In order to verify the formulation accuracy, the worked out results are compared with the ones obtained using analytical and numerical solutions. Tables 1, 2 and 3 show the first five natural frequencies for six different types of shell structures. Some mode shapes of the considered shell structures are illustrated in Figure 1. Various boundary conditions and general lamination schemes are investigated.

Mode [Hz]	EDZ4 GDQ	3D FEM	$e_{\%} = \frac{\lvert f_{GDQ} - f_{FEM} \rvert}{f} \cdot 100$	EDZ4 GDQ	3D FEM	$e_{\%} = \frac{\lvert f_{GDQ} - f_{FEM} \rvert}{f} \cdot 100$	EDZ4 GDQ	3D FEM	$e_{\%} = \frac{\lvert f_{GDQ} - f_{FEM} \rvert}{f} \cdot 100$
Shell Structure	C-C-C-C (30/70/45) Hyperbolic Paraboloid			C-C-C-C (30/70/45) Elliptic Paraboloid			C-C-F-F (Isotropic) Parabolic Degenerate Plate		
f_1	193.14	193.18	0.0194	209.59	209.56	0.0125	30.30	30.37	0.2401
f_2	194.70	194.64	0.0327	214.37	214.34	0.0144	101.52	101.50	0.0240
f_3	215.35	215.31	0.0193	231.88	231.79	0.0390	136.82	136.79	0.0189
f_4	238.53	238.41	0.0523	276.06	275.95	0.0393	236.50	236.51	0.0043
f_5	292.38	292.24	0.0487	305.78	305.63	0.0496	277.51	277.53	0.0054

Table 1. First ten frequencies for three different shell and panel structures.

Mode [Hz]	EDZ4 GDQ	3D FEM	$e_{\%} = \frac{\lvert f_{GDQ} - f_{FEM} \rvert}{f} \cdot 100$	EDZ4 GDQ	3D FEM	$e_{\%} = \frac{\lvert f_{GDQ} - f_{FEM} \rvert}{f} \cdot 100$	EDZ4 GDQ	3D FEM	$e_{\%} = \frac{\lvert f_{GDQ} - f_{FEM} \rvert}{f} \cdot 100$
Shell Structure	C-C-C-C (30/45) Catenoidal Panel			C-C-C-C (Isotropic) Curved Cylindrical Panel (Elliptic Curve on Catenary Curve)			F-C-F-F (Isotropic) Bi-polar Degenerate Plate with Variable Thickness		
f_1	385.52	385.32	0.0529	382.60	382.76	0.0412	26.06	25.97	0.3640
f_2	437.77	437.28	0.1113	452.15	452.31	0.0346	42.20	42.27	0.1637
f_3	485.73	485.43	0.0615	558.19	558.36	0.0308	62.82	62.28	0.8724
f_4	574.36	573.56	0.1390	687.02	687.23	0.0298	79.20	79.40	0.2501
f_5	640.12	639.50	0.0968	741.24	741.28	0.0051	121.47	121.70	0.1903

Table 2. First ten frequencies for three different shell and panel structures.

Mode [Hz]	FSDT GDQ	ED4 GDQ	EDZ4 GDQ	LD4 GDQ	3D FEM	FSDT $e_{\%} = \frac{\lvert f_{GDQ} - f_{FEM} \rvert}{f} \cdot 100$	ED4 $e_{\%} = \frac{\lvert f_{GDQ} - f_{FEM} \rvert}{f} \cdot 100$	EDZ4 $e_{\%} = \frac{\lvert f_{GDQ} - f_{FEM} \rvert}{f} \cdot 100$	LD4 $e_{\%} = \frac{\lvert f_{GDQ} - f_{FEM} \rvert}{f} \cdot 100$
f_1	380.90	385.52	385.67	385.30	385.32	1.1470	0.0530	0.0896	0.0041
f_2	431.13	437.77	437.90	437.19	437.28	1.4058	0.1119	0.1426	0.0208
f_3	478.34	485.73	485.83	485.36	485.43	1.4596	0.0618	0.0815	0.0145
f_4	563.46	574.36	574.44	573.48	573.56	1.7612	0.1392	0.1540	0.0145
f_5	628.23	640.12	640.28	639.27	639.50	1.7618	0.0974	0.1216	0.0356

Table 3. First ten frequencies for C-C-C-C (30/45) catenoidal panel.

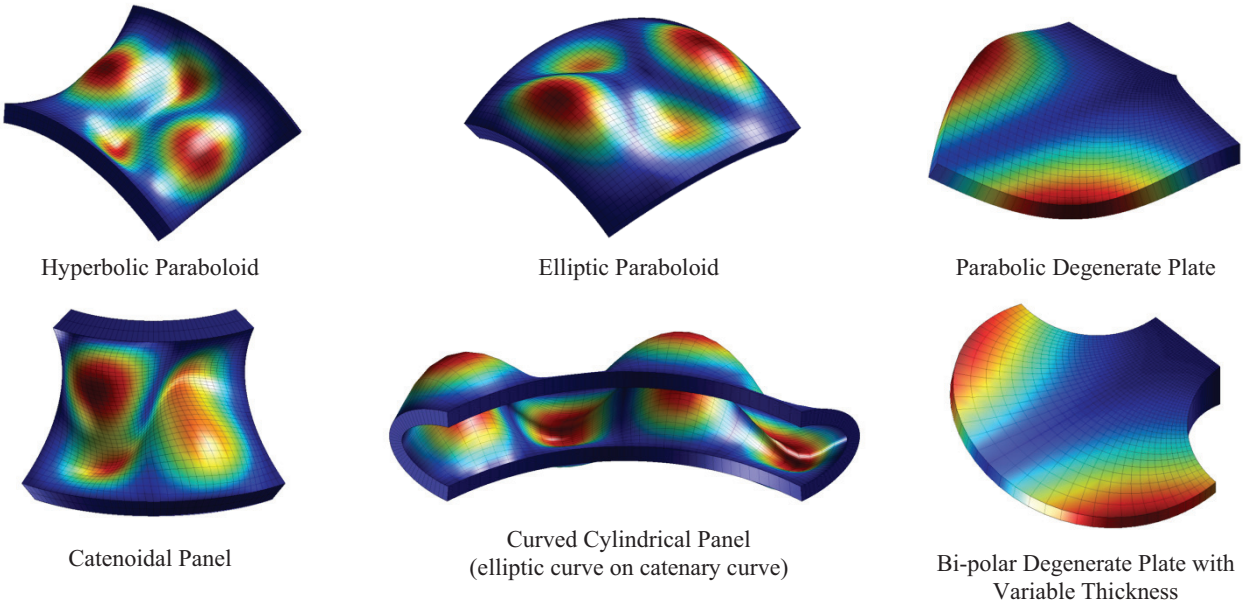

Figure 1. Different mode shapes for various shell structures.

REFERENCES

[1] H. Kraus, *Thin Elastic Shells*, John Wiley & Sons, 1967.

[2] W. Soedel, *Vibrations of Shells and Plates*, Marcel Dekker, 2004.

[3] J.N. Reddy, *Mechanics of Laminated Composite Plates and Shells*, CRC Press, 2003.

[4] E. Carrera, S. Brischetto, P. Nali, *Plates and Shells for Smart Structures: Classical and Advanced Theories for Modeling and Analysis*, John Wiley & Sons, 2011.

[5] C. Shu, *Differential Quadrature and Its Application in Engineering*, Springer, 2000.

[6] F. Tornabene, "Vibration analysis of functionally graded conical, cylindrical and annular shell structures with a four-parameter power-law distribution", *Comput. Methods Appl. Mech. Engrg.* 198, 2911-2935, (2009).

[7] F. Tornabene, "2-D GDQ solution for free vibrations of anisotropic doubly-curved shells and panels of revolution", *Compos. Struct.* 93, 1854-1876, (2011).

[8] F. Tornabene, "Free Vibrations of Anisotropic Doubly-Curved Shells and Panels of Revolution with a Free-Form Meridian Resting on Winkler-Pasternak Elastic Foundations", *Compos. Struct.* 94, 186-206, (2011).

[9] E. Viola, F. Tornabene, N. Fantuzzi, "General higher-order shear deformation theories for the free vibration analysis of completely doubly-curved laminated shells and panels", *Compos. Struct*. 95, 639-666, (2013).

[10] E. Viola, F. Tornabene, N. Fantuzzi, "Static analysis of completely doubly-curved laminated shells and panels using general higher-order shear deformation theories", *Compos. Struct.* 101, 59-93, (2013).

[11] F. Tornabene, E. Viola, "Static analysis of functionally graded doubly-curved shells and panels of revolution", *Meccanica* 48, 901-930, (2013) .

On the vibro-acoustics of piles in layered media

A. Tsouvalas and A.V. Metrikine
Section of Structural Mechanics, Faculty of Civil Engineering and Geosciences, Delft University of Technology, The Netherlands

Introduction. The aim of the present study is the development of a model for the prediction of the high-frequency pile-soil-water dynamics induced by offshore pile driving. The ground motion and the generated sound field due to pile driving depends on the source parameters (driving method, input energy of the hydraulic hammer etc.), the soil-fluid-pile interaction and the propagation of waves in the surrounding media. Steel monopiles are nowadays widely used as foundation of offshore wind turbines and are driven into place with the help of hydraulic hammers as shown in Fig.1. The installation process is accompanied with high sound pressures in the surrounding fluid which are considered to be harmful for the marine ecosystem. In this study, a linear semi-analytical formulation of the coupled vibro-acoustic problem of the complete system is addressed. The model is similar to, but significantly more advanced than, the one presented by the authors in [1]. The advance is associated with a three-dimensional description of the soil adopted in the new model. The pile is described by a thin shell theory whereas both fluid and soil are treated as three-dimensional continua. Fluid is assumed to be present only at the exterior of the pile.

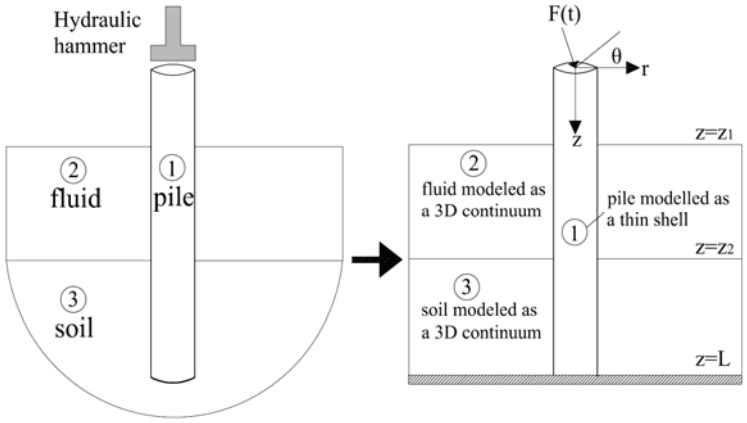

Fig.1 Geometry of the model and definition of the adopted coordinate system

The solution of the system of coupled partial differential equations is based on the dynamic sub-structuring technique according to which the total system is divided into two sub-systems: the shell structure and the soil-fluid layered medium. The linearity of the model allows for the representation of the response of each subsystem in the form of a superposition over appropriate eigenfunctions. The completeness of the modal sum for the layered soil-fluid domain is guaranteed by the introduction of a rigid boundary at a certain depth as shown in Fig.1.

Model description. The pile is described by an appropriate thin shell theory which includes the effects of shear deformation and rotational inertia [2]. The governing equation describing the shell vibrations in the time domain reads:

$$\mathbf{L}\mathbf{u}_{\mathrm{p}}(z,\theta,t)+\mathbf{I}_{\mathrm{m}}\mathbf{u}_{\mathrm{p}}(z,\theta,t)=-H(z-z_2)\ \boldsymbol{\sigma}_{\mathrm{s}}(R,\theta,z,t)+\left[H(z-z_1)-H(z-z_2)\right]\ \mathbf{p}_{\mathrm{f}}(R,\theta,z,t)+\mathbf{f}_{\mathrm{e}}(z,\theta,t). \tag{1}$$

In the equation above, $\mathbf{u}_{\mathrm{p}}(z,\theta,t)$ is the displacement vector of the mid-surface of the shell. The terms $\mathbf{L}$ and $\mathbf{I}_{\mathrm{m}}$ are the stiffness and modified inertia matrix operators of the shell, respectively, which are based on the applied thin shell theory. Material dissipation is accounted for by means of a frequency independent complex-valued elasticity modulus of the steel in the frequency domain. The term $\boldsymbol{\sigma}_{\mathrm{s}}(R,\theta,z,t)$ represents the boundary traction vector that takes into account the reaction of the soil

surrounding the shell at $z_2 \le z \le L$. The term $\mathbf{p_f}(R,\theta,z,t)$ represents the fluid pressure exerted at the outer surface of the shell at $z_1 \le z \le z_2$. The functions $H(z-z_i)$ are the Heaviside step functions which are used here to account for the fact that the soil and the fluid are in contact with different segments of the shell.

The fluid is treated as a three-dimensional inviscid compressible medium with a pressure release boundary describing the sea surface. The motion of the fluid is fully characterized by a velocity potential $\varphi_f(r,\theta,z,t)$:

$$\nabla^2\varphi_f(r,\theta,z,t)-\frac{1}{c_f^2}\frac{\partial^2\varphi_f(r,\theta,z,t)}{\partial t^2}=0 \tag{2}$$

where c_f is the sound speed in the exterior fluid domain. The soil is described as a three-dimensional perfectly elastic continuum able to support both dilatational and shear waves and is terminated at a certain depth with a rigid boundary. The body waves generated at the pile tip are not accounted for in the framework of this model. These waves are not expected to contribute to the acoustic field significantly since they will mainly consist of shear and compressional body waves with a spherical front spreading outwards and thus they will experience large attenuation [3] at the frequency range of interest. The motion of the soil medium is described by the following set of linear equations:

$$\mu_s\cdot\nabla^2\mathbf{u}+(\lambda_s+\mu_s)\cdot\nabla\nabla\cdot\mathbf{u}=\rho_s\cdot\frac{\partial^2\mathbf{u}}{\partial t^2} \tag{3}$$

$\lambda_s = E_s v_s/[(1+v_s)\cdot(1-2v_s)]$ and $\mu_s = E_s/2\cdot(1+v_s)$ being the *Lamè* constants for the soil. The constants E_s and v_s correspond to the Young's modulus and the density of the soil respectively. The solution for the soil domain can be found using the *Lamb's* decomposition and introduction of potentials. The response of the coupled system is sought for in the form of a modal expansion with respect to the *in vacuo* shell modes and to those of the soil-fluid domain. The analytical approach is based on the following steps: **i)** solution of the eigenvalue problem of the shell without the presence of the fluid and the soil; **ii)** solution of the eigenvalue problem of the soil-fluid domain; **iii)** solution of the coupled system of equations resulting from the substitution of the obtained solutions for the shell and the soil-fluid domains into the interface conditions. For the shell *in vacuo* the response can be represented as follows:

$$u_{j,p}(z,\theta,t)=\sum_{n=0}^{\infty}\sum_{m=1}^{\infty}A_{nm}U_{jnm,p}(z)\cos\left(\delta_{j\theta}\frac{\pi}{2}-n\theta\right)\exp(\mathrm{i}\Omega_{mn}\mathrm{t}), \tag{4}$$

where $n=0,1,2,..,\infty$ is the circumferential order and $m=1,2,..,\infty$ is the axial order. The functions $U_{jnm,p}(z)$ with $j=z,\theta,r$ describe the axial distribution for the axial, circumferential and radial displacement fields respectively. A_{nm} are the undetermined shell modal factors. For the exterior soil-fluid domain the response can be represented as:

$$u_{j,s;f}(r,\theta,z,t)=\sum_{n=0}^{\infty}\sum_{k=1}^{\infty}C_{nk}U_{jnk,s;f}(z)\begin{Bmatrix}\cos(n\theta)\\ \sin(n\theta)\end{Bmatrix}R_{nk}(r)\exp(\mathrm{i}\omega\mathrm{t}). \tag{5}$$

The subscripts s and f refer to the soil and fluid respectively. The eigenfunctions $U_{jnk,s;f}(z)$ along the vertical coordinate are obtained by satisfying the set of boundary and interface conditions at $z=z_q$ with $q=1,2,...,l$ corresponding to the different layers. The index *k* is used here to reflect the different modes along the vertical coordinate. In accordance with Fig.1, the following set of boundary and interface conditions is imposed. At $z=z_1$ the fluid pressure is set equal to zero. At $z=z_2$ the normal stress and displacement are continuous whereas the shear stress of the soil is set equal to zero (inviscid fluid). Finally, at $z=L$ the displacements of the soil are set equal to zero. The functions $R_{nk}(r)$ correspond to the Hankel functions of the second type and of different order depending on the circumferential index *n*, which appropriately describe the radial dependence of the field. By enforcing force equilibrium and displacement compatibility at the interface between the shell and the exterior

domain, the original system of coupled partial differential equations is reduced to a system of coupled algebraic equations which can be solved with high accuracy. To achieve this, the orthogonality condition for the shell structure *in vacuo* and the one of the exterior soil-fluid domain are used to relate the unknown sets of modal coefficients (A_{nm} , C_{nk}) and to solve the coupled problem.

Numerical Results. In this section some preliminary results are presented for a pile with length L=32.4 m, diameter D=0.92 m and thickness t=0.02 m. The material parameters of the pile are E_p=2.1 10^5 Mpa, v_p=0.28 and ρ_p=7850 kg m^{-3}. The soil consists of a single layer with E_s=100 Mpa , v_s=0.40 and ρ_s=1600 kg m^{-3} in the case of a *soft soil* and E_s=500 Mpa , v_s=0.40 and ρ_s=1800 kg m^{-3} in the case of a *stiff soil*. The water is modelled as an inviscid fluid with c_f=1500 ms^{-1} and ρ_f=1000 kg m^{-3}. In accordance with Fig.1, z_1=6 m and z_2=13.2 m. The external load corresponds to a hammer input energy of 90 kJ. The maximum force amplitude equals 12 MN and the duration of the main pulse is equal to 5 ms. In Fig.2, the generated wave field is shown for the (outer to the shell) soil-fluid domain.

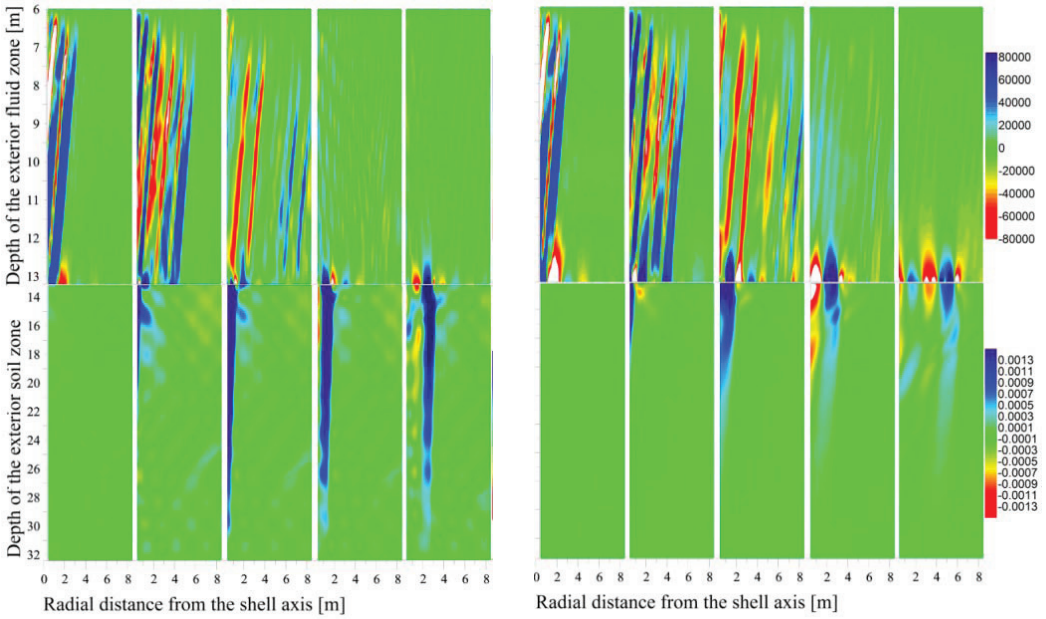

Fig. 1.2 Pressures in the fluid (top) and vertical displacements in the soil (bottom) for successive time moments after the impact in the case of a *soft soil* (left) and a *stiff soil* (right). In both figures from left to right: t=4ms; t=6ms; t=10ms; t=15ms; t=25ms after the impact of the hammer.

As can be seen, the response in the fluid region is dominated by pressure *Mach cones* due to the supersonic compressional waves in the pile generated by the impact hammer. These cones are formed with an angle of about $\sin^{-1}\left(c_f / c_p\right) \approx \sin^{-1}\left(1500/5000\right) \approx 17^0$ to the vertical. The soil response is dominated by shear waves with almost vertical polarization. *Scholte* waves are generated at the soil-fluid interface. These waves propagate with a velocity slightly lower than that of the shear waves in the soil and their energy is localized in a restricted zone close to the interface. The penetration depth of the *Scholte* waves into the soil depends on soil elasticity. For stiffer soils, a larger portion of the input energy is localized in the fluid.

References

[1] A. Tsouvalas, A.V. Metrikine, 2013. A semi-analytical model for the prediction of underwater noise from offshore pile driving. *Journal of Sound and Vibration,* Volume 332 (2013), pp. 3232-3257.

[2] A.V. Belov, J.D. Kaplunov, E.V. Nolde, 1999. A refined asymptotic model of fluid-structure interaction in scattering by elastic shells. *Flow, Turbulence and Combustion,* Volume 61, pp. 255-267.

[3] H.R. Masoumi, G. Degrande, 2008. Numerical modelling of free field vibrations due to pile driving using a dynamic soil-dtructure interaction formulation. *Journal of Computational and Applied Mathematics,* Volume 215, pp. 503-511.

Damping Effects on Stabilizing Rotating Non-Circular Shafts Subjected to Pulsating Axial Force

Jörg Wauer*, Hartmut Hetzler, Christoph Baum
Institute of Engineering Mechanics (ITM), Karlsruhe Institute of Technology (KIT)
Kaiserstraße 10, 76131 Karlsruhe, Germany

Introduction Well-known and extensively discussed is the instability of parametrically excited mechanical systems, see [1], for instance. In 1998 when Tondtl found out [2] that a specific parametric excitation can also stabilize an otherwise unstable system, this stabilizing effect attracted more and more attention, see [3,4,5], for instance. Also for rotating systems, this stabilization phenomenon has recently been examined [6,7,8]. From earlier work in rotor dynamics it is well-known that damping can significantly influence the stability of rotors, in particular internal damping which for rotating systems is much more important [9,10]. Therefore, also for stabilizing rotating non-circular shafts by pulsating force, the study of damping effects seems to be very important which was not sufficiently discussed within the work [6,7,8] established. The present contribution aims on this particular aspect.

Problem Description Considering a rotating (Ω) non-circular Bernoulli–Euler shaft (mass per unit length ϱA, bending stiffnesses $EI_{u,v}$), simply supported on both ends, subjected to an axial time-dependent load $F(t)$ and including external (d_e) and internal (d_i) damping, the governing boundary value problem reads (see [11], for instance)

$$\varrho A\left(\ddot{u}-2\Omega\dot{v}-\Omega^2 u\right)+d_e\varrho A\left(\dot{u}-\Omega v\right)+EI_u\left(u_{,xxxx}+d_i\dot{u}_{,xxxx}\right)-F(t)u_{,xx} \;=\; 0 \quad (1)$$

$$\varrho A\left(\ddot{v}+2\Omega\dot{u}-\Omega^2 u\right)+d_e\varrho A\left(\dot{v}+\Omega u\right)+EI_v\left(v_{,xxxx}+d_i\dot{v}_{,xxxx}\right)-F(t)v_{,xx} \;=\; 0 \quad (2)$$

$$\text{BCs.:}\;\; u(0)=0, u(L)=0, u_{,xx}(0)=0, u_{,xx}(L)=0,\; v(0)=0, v(L)=0, v_{,xx}(0)=0, v_{,xx}(L) \;=\; 0, \quad (3)$$

where $u=u(x,t)$ and $v=v(x,t)$ are the displacements of the shaft's neutral fibre measured with respect to a rotating reference frame and $()_{,x}=\partial()/\partial x$ and $()_{,t}=\partial()/\partial t$. The scaling of variables $\xi=x/L$, $\tau=\Omega_0 t$, $U=u/L$, and $V=v/L$ yields dimensionless parameters

$$EI_0=(EI_u+EI_v)/2\;,\;\mu=\frac{EI_u-EI_v}{EI_0}\;,\;f=\frac{FL^2}{EI_0}\;,\;\Omega_0=\frac{EI_0}{L^4\varrho A}\;,\;\bar{d}_i=d_i\Omega_0\;,\;\bar{d}_e=\frac{d_e}{\Omega_0} \quad (4)$$

and the dimensionless boundary value problem

$$\begin{pmatrix}U\\V\end{pmatrix}''+\begin{bmatrix}\bar{d}_e+\bar{d}_i(1+\mu)\frac{\partial^4}{\partial\xi^4} & -2\eta\\ +2\eta & \bar{d}_e+\bar{d}_i(1-\mu)\frac{\partial^4}{\partial\xi^4}\end{bmatrix}\begin{pmatrix}U\\V\end{pmatrix}' \quad \Big|\;()'=\partial()/\partial\tau. \quad (5)$$

$$+\begin{bmatrix}(1+\mu)\frac{\partial^4}{\partial\xi^4}-\eta^2-f(t)\frac{\partial^2}{\partial\xi^2} & -\eta\bar{d}_e\\ +\eta\bar{d}_e & (1-\mu)\frac{\partial^4}{\partial\xi^4}-\eta^2-f(t)\frac{\partial^2}{\partial\xi^2}\end{bmatrix}\begin{pmatrix}U\\V\end{pmatrix}=\begin{pmatrix}0\\0\end{pmatrix} \qquad +\text{BCs.}$$

Evaluation Using the series expansion

$$U \;=\; \sum_{i=1}^{N}\sqrt{2}\sin(k\pi\xi)\,,\quad V=\sum_{j=1}^{N}\sqrt{2}\sin(k\pi\xi) \quad (6)$$

which fulfills all boundary conditions, yields a system of $2N$ coupled ordinary differential equations

$$\mathbf{M}\mathbf{q}''+(\mathbf{D}+\mathbf{G})\mathbf{q}'+(\mathbf{K}+\tilde{\mathbf{K}}f(\tau)+\mathbf{N})\mathbf{q}=\mathbf{0} \quad (7)$$

*joerg.wauer@kit.edu

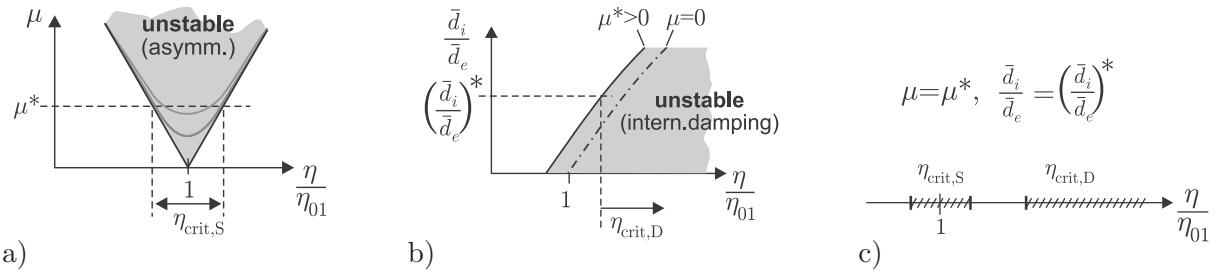

Figure 1: Steady state stability ($N = 1$): a) Non-symmetric stiffness. b) Damping. c) Critical speeds.

where the matrix elements can easily be computed for each desired finite N–term truncation. For the following, a harmonic axial force $f(\tau) = \cos\eta\tau$ is considered where the condition $\left(\mathbf{K} + \tilde{\mathbf{K}}\cos\eta\tau\right) > 0$ for $\pi^4(1-|\mu|) - \eta^2 - \pi^2\hat{f} > 0$ or $\hat{f} < \pi^2(1-|\mu|) - \frac{\eta^2}{\pi^2}$ should be fulfilled to avoid buckling (quasistatic f). The stability behavior for such systems with harmonic force can be studied using Floquet theory where the simpler case of constant or missing force can be decided applying the Hurwitz criteria. The lowest $N = 1$–term approximation

$$\mathbf{M} = \begin{bmatrix} 1 & 0 \\ 0 & 1 \end{bmatrix} \quad , \quad \mathbf{D} = \begin{bmatrix} \bar{d}_e + \bar{d}_i\pi^4(1+\mu) & 0 \\ 0 & \bar{d}_e + \bar{d}_i\pi^4(1-\mu) \end{bmatrix} \quad , \quad \mathbf{G} = \begin{bmatrix} 0 & -2\eta \\ +2\eta & 0 \end{bmatrix} \quad , \tag{8}$$

$$\mathbf{K} = \begin{bmatrix} \pi^4(1+\mu) - \eta^2 & 0 \\ 0 & \pi^4(1-\mu) - \eta^2 \end{bmatrix} \quad , \quad \tilde{\mathbf{K}} = \begin{bmatrix} -\pi^2 & 0 \\ 0 & -\pi^2 \end{bmatrix} \quad , \quad \mathbf{N} = \begin{bmatrix} 0 & -\eta\bar{d}_e \\ +\eta\bar{d}_e & 0 \end{bmatrix} \tag{9}$$

corresponds with a non-circular Jeffcott rotor to primarily be discussed within this contribution.

Results The starting point is the stability of the trivial solution $U, V = 0$ for the non–circular rotor without axial force. Destabilization due to non-symmetric bending stiffness occurs in an interval of critical speeds, which for $\bar{d}_i = 0, \bar{d}_e = 0$ reads

$$\eta_{crit,S} \in \eta_{01}[\sqrt{1-\mu}, \sqrt{1+\mu}] \tag{10}$$

where $\eta_{01} = \pi^2$ is the first critical speed of the symmetric rotor ($\mu = 0$). For non-vanishing damping this is still a conservative approximation (see Fig. 1 a). Well–known is the stabilizing effect of external damping and the destabilization due to inner damping which occurs if a critical speed is trespassed. Using Hurwitz' criteria, this stability threshold is found as

$$\eta_{crit,D} \approx \eta_{01}\left(1 + \frac{1}{\pi^4}\left(\frac{\bar{d}_e}{\bar{d}_i}\right) + \frac{1}{2\pi^8}\left(\frac{\bar{d}_e}{\bar{d}_i}\right)^2 - \frac{1}{2}\mu^2\right) + \ldots \qquad \text{for} \quad \frac{\bar{d}_e}{\bar{d}_i} \ll \pi^4. \tag{11}$$

Next – via Floquet theory – we investigate the stability of the trivial solution for the rotor with harmonic axial force (frequency η_P, intensity f): first without internal damping (see Fig. 2) and then also accounting for internal damping (see Fig. 3). It is obvious that beside the well-known areas of parametric destabilization (near $\eta_P/\eta_{01} \approx 1/p$, $p = 1, 2, \ldots$) there also appear small areas where the harmonic axial force stabilizes parameter combinations which would be unstable without axial force. However, it is also found that this effect of parametric stabilization strongly interacts with the effect of internal damping: on the one hand, there are parameter regions where the varying axial force intensifies the destabilizing effect of internal damping – on the other hand, the axial force can also neutralize destabilization due to internal damping for some parameter combinations.

For the more general case of a $N = 2$–term approximation, there are 4 coupled ordinary differential equations. Similar results as before are obtained: Instead of one pair of critical speeds with one unstable band between, there are now two pairs of critical speeds with an unstable area between each of them. External damping is stabilizing once again and internal damping is destabilizing as explained for a similar system within the paper [9]. For a pulsating axial force, there is a more complex stability behavior than for the $N = 1$–truncation. Details will be shown during the symposium.

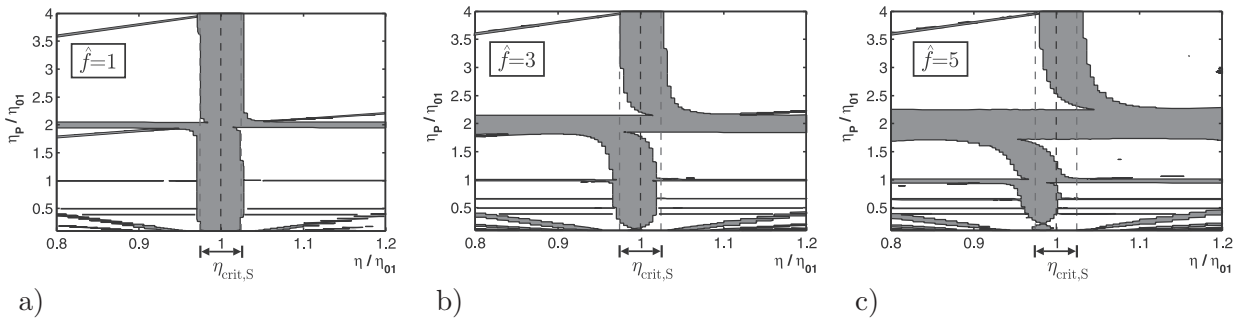

Figure 2: Steady state stability of a rotor without internal damping ($\bar{d}_i = 0$, $\bar{d}_e = 1 \cdot 10^{-3}$, $N = 1$). Gray areas indicate unstable parameter combinations, dashed lines are stability borders for vanishing axial force.

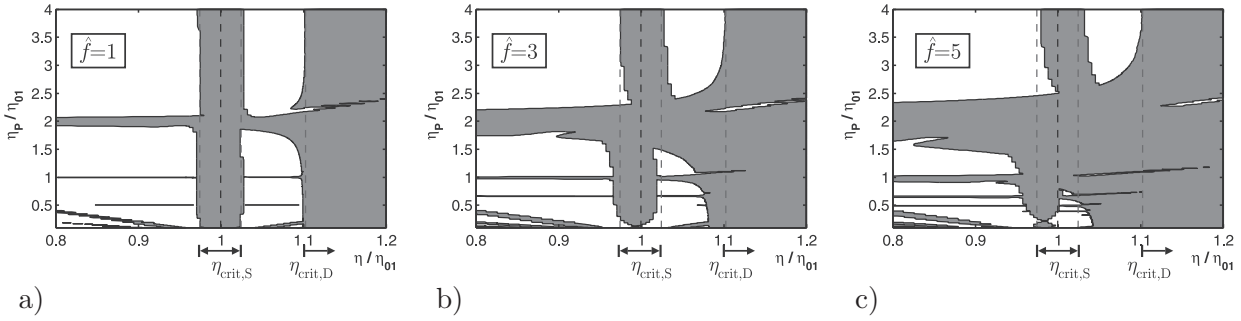

Figure 3: Steady state stability of a rotor with internal damping ($\bar{d}_i = 5 \cdot 10^{-4}$, $\bar{d}_e = 5 \cdot 10^{-3}$, $N = 1$). Gray areas indicate unstable parameter combinations, dashed lines are stability borders for vanishing axial force.

Conclusion As expected, pulsating axial forces on rotating shafts provoke typical parametric instabilities near parameter frequencies of $\eta_P/\eta_{01} \approx 1/p$ ($p = 1, 2, \dots$). As a surprising result, both destabilizing effects may neutralize each other if this parametric excitation interacts with other instabilies – e.g. due to non-symmetric bending stiffness or internal damping. Thus, pulsating axial forces may also have a stabilizing effect. However, it has been shown within this contribution that internal damping strongly interacts with this effect, narrows the areas of stabilization and may even destroy the beneficial influence of the axial force. As an outlook it would be interesting to investigate also forced vibrations due to unbalance and to extend the shaft model in the sense of a Rayleigh or a Timoshenko shaft.

References

[1] G. Schmidt, Parametererregte Schwingungen, Dt. Verl. d. Wiss., Berlin, 1975.

[2] A. Tondl, *Acta Technica ČSAV* 43 (1998), 109–116.

[3] A. Seyranian, and A. Seyranian, *J. Appl. Math. Mech.* 70 (2006), 754–761.

[4] F. Dohnal, H. Ecker, H. Springer, *Arch. Appl. Mech.* 78 (2008), 935–947.

[5] H. Ecker, and T. Pumhössel, *Proc. IMechE Part C* 226 (2012), 2000–2014.

[6] T. Pumhössel, H. Ecker, and A. Tondl, in: Proc. SIRM 2011, Paper–ID 10, Darmstadt.

[7] H. Ecker, in: K. Gupta (ed), *IUTAM Symposium on Emerging Trends in Rotor Dynamics*, IUTAM Bookseries 25, Springer, Heidelberg, 2011, 361–371.

[8] D. Bartylla, *Mechanism and Machine Theory* 58 (2012), 13–19.

[9] W. Kellenberger, *Ing.–Arch.* 32 (1963), 323–340.

[10] J. Michatz, Das Biegeverhalten einer einfach besetzten unrunden rotierenden Welle unter Berücksichtigung äußerer und innerer Dämpfung, PhD Thesis, TU Berlin, 1970.

[11] J. Wauer, Kontinuumsschwingungen, Teubner, Stuttgart 2008.

Parametric Instability in Second-Order Non-Dispersive Distributed Structural Systems

W.D. Zhu
Department of Mechanical Engineering, University of Maryland, Baltimore County
1000 Hilltop Circle, Baltimore, Maryland 21250, U.S.A.
Email: wzhu@umbc.edu

1. Introduction

Parametric instability in a system is caused by periodically varying coefficients in its governing differential equations. While parametric excitation of lumped-parameter systems has been extensively studied, that of distributed-parameter systems has been traditionally analyzed by applying Floquet theory to their spatially discretized equations. In this work, parametric instability regions of a second-order non-dispersive distributed structural system, which consists of a translating string with a constant tension and a sinusoidally varying velocity, and two boundaries that axially move with a sinusoidal velocity relative to the string, are obtained using the wave solution and the fixed point theory without spatially discretizing the governing partial differential equation. Unlike parametric instability regions of lumped-parameter systems that are classified as principal, secondary, and combination instability regions, the parametric instability regions of distributed structural systems considered here are classified as period-1 and period-*i* (*i* >1) instability regions. Unlike parametric instability in a lumped-parameter system that is characterized by an unbounded displacement, the parametric instability phenomenon discovered here is characterized by a bounded displacement and an unbounded vibratory energy, due to formation of infinitely compressed shock-like waves.

2. Parametric Instability for the Linear Model

The non-dimensional equation that governs the free transverse vibration of the translating string (Fig. 1) is

$$u_{tt}(x,t)+2v(t)u_{xt}(x,t)+\left[v^2(t)-1\right]u_{xx}(x,t)+\dot{v}(t)u_x(x,t)=0,\ x_l(t)<x<x_r(t), \tag{1}$$

where x is the spatial position, t is time, $u(x,t)$ is the transverse displacement at position x at time t, the subscripts denote partial differentiation, the overdot denotes time differentiation, $v(t)=v_0+v_1\sin(\omega t)$, $x_r(t)=-v_{21}\cos(\omega t+\phi_1)/\omega+1$, and $x_l(t)=-v_{22}\cos(\omega t+\phi_2)/\omega$. The translating string has homogeneous boundary conditions and arbitrary initial conditions. Note that the velocities of the right and left boundaries are $v_r(t)=v_{21}\sin(\omega t+\phi_1)$ and $v_l(t)=v_{22}\sin(\omega t+\phi_2)$, respectively. Also note that the translation velocities of the string relative to the two boundaries are assumed to be subcritical, i.e., $|v(t)-v_r(t)|<1$ and $|v(t)-v_l(t)|<1$.

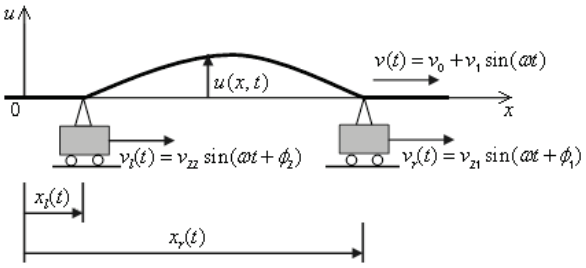

Fig. 1 Schematic of the translating string model

The non-dimensional energy density associated with the transverse vibration of the translating string at the spatial position x at time t is [1]

$$\varepsilon(x,t)=\frac{1}{2}\left[u_t(x,t)+v(t)u_x(x,t)\right]^2+\frac{1}{2}u_x^2(x,t), \tag{2}$$

where the first and second terms on the right-hand side are the kinetic and potential energies associated with the transverse vibration of the string. A control volume at time t is defined as the spatial domain $\left\{x\,|\,x\in\left[x_l(t),x_r(t)\right]\right\}$. The vibratory energy of the translating string in the control volume is

$$E_{cv}(t)=\int_{x_l(t)}^{x_r(t)}\varepsilon(x,t)\,dx. \tag{3}$$

It can be shown following Ref. [2] that the slope ratio of the reflected wave to the incident wave at the right and the left boundaries at time t are $\alpha_r(t)=\dfrac{1+\left[v(t)-v_r(t)\right]}{1-\left[v(t)-v_r(t)\right]}$ and $\alpha_l(t)=\dfrac{1-\left[v(t)-v_l(t)\right]}{1+\left[v(t)-v_l(t)\right]}$, respectively. If the slope of the reflected wave from the right (left) boundary is larger than that of the incident wave, i.e. $\alpha_r(t)>1$ ($\alpha_l(t)>1$), the width of the reflected wave is smaller than that of the incident wave, and the wave is compressed after reflection from the right (left) boundary. The vibratory energy of the translating string increases if an infinitesimal wave is compressed after reflection from a boundary.

Consider an infinitesimal wave in the translating string, which is assumed, without loss of generality, to be initially located at the left boundary at time t_0 and propagate rightward. The series of times when the wave travels to the right boundary and back to the left boundary are denoted by t_n' ($n=0,1,2,\cdots$) and t_n ($n=1,2,3,\cdots$), respectively. The phase of the translation velocity $v(t)=v_0+v_1\sin(\omega t)$ at t_n is denoted by $\varphi_n=Arg(\omega t_n)\in[0,2\pi)$. A period-$i$ fixed point φ_n of the phase function f^i is defined by

$$\varphi_{n+i}=f^i(\varphi_n),\ \varphi_n\neq\varphi_{n+1}\neq\cdots\neq\varphi_{n+i-1}. \tag{4}$$

Instability occurs when φ_n is an attracting period-i ($i\geq 1$) fixed point of function f^i. From the derivation in Ref. [3], $\left|\alpha_l(t_n)\alpha_r(t_n')\alpha_l(t_{n+1})\alpha_r(t_{n+1}')\cdots\alpha_l(t_{n+i-1})\alpha_r(t_{n+i-1}')\right|>1$, which means the same infinitesimal wave is overall compressed for the first time after i ($i\geq 1$) round trips, and will be further compressed after each i round trips. This type of instability is referred to as period-i ($i\geq 1$) parametric instability.

3. Results

There are five non-trivial cases that involve different combinations of string and boundary motions: I) a translating string with a sinusoidally varying velocity and two stationary boundaries; II) a translating string with a sinusoidally varying velocity, a sinusoidally moving boundary, and a stationary boundary; III) a translating string with a sinusoidally varying velocity and two sinusoidally moving boundaries; IV) a stationary string with a sinusoidally moving boundary and a stationary boundary; and V) a stationary string with two sinusoidally moving boundaries.

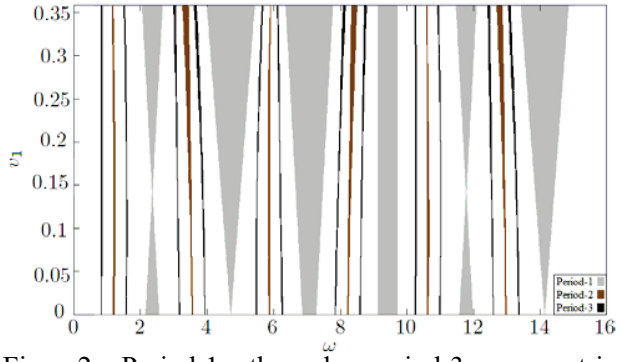

Fig. 2 Period-1 through period-3 parametric instability regions in case III with $v_0=0.5$, $v_{21}=v_{22}=0.1414$, $\phi_1=0.5\pi$, and $\phi_2=1.5\pi$.

Period-1 parametric instability regions are analytically obtained, and period-i ($i>1$) parametric instability regions can be numerically calculated using bifurcation diagrams. Figure 2 shows the parametric instability regions for case III. It is proved using Sharkovsky's theorem that only period-1 parametric instability regions exist in case IV, and no period-i ($i>1$) parametric instability regions can be numerically found in case V.

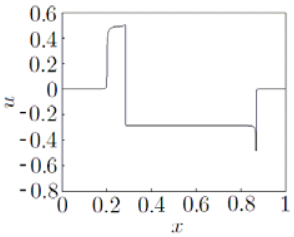

Fig. 3 Wave pattern of the translating string in case III with parameters chosen within period-2 parametric instability region with $k=3$ at $t=48$

Similar to classical resonance, all the period-1 parametric instability regions are centered at the natural frequencies of the translating or stationary strings with an averaged translation velocity and/or an averaged length. For instance, all period-1 parametric instability regions in case III are centered at the natural frequencies of the translating string $k\omega_0=k\pi\left(1-v_0^2\right)$ with an averaged translating velocity $v_0=0.5$ and an averaged unit length as shown in Fig. 2.

If the parameters are chosen to be in the period-i ($i \geq 1$) parametric instability region corresponding to an integer k, an initial smooth wave will be infinitely compressed to k shock-like waves as time approaches infinity. Figure 3 shows the wave pattern of the translating string in case III with parameters chosen with in the period-2 parametric instability region with $k = 3$ at $t = 48$. There are three infinitely compressed shock-like waves in the wave pattern.

The stable and unstable responses of the linear model in case I are compared with those of a corresponding nonlinear model that considers the coupled transverse and longitudinal vibrations of the translating string and an intermediate linear model that includes the effect of the tension change due to axial acceleration of the string on its transverse vibration [4]. The transverse displacement of the translating string at the middle point is calculated from the original linear and nonlinear models and an intermediate linear model [4] using Galerkin's method with parameters chosen within the stable and parametric instability regions of the original linear model, as shown in Fig. 4. The initial displacement in the transverse direction is chosen as a half sine wave and the other initial conditions are zero. The transverse vibratory energies of the translating string from the three models are shown in Fig. 5. They overall grow with time in Figs. 5(b,d,f), with the largest growth rate in Fig. 5(b) and the smallest growth rate in Fig. 5(d), which means that the parametric instability also exists in the nonlinear and intermediate linear models. The transverse displacements of the translating string at the middle point from the three models grow sharper with time for the unstable solution in Figs. 4(b,d,f), and there are no obvious sharpness changes in the transverse displacements for the stable solutions in Fig. 4(a,c,e).

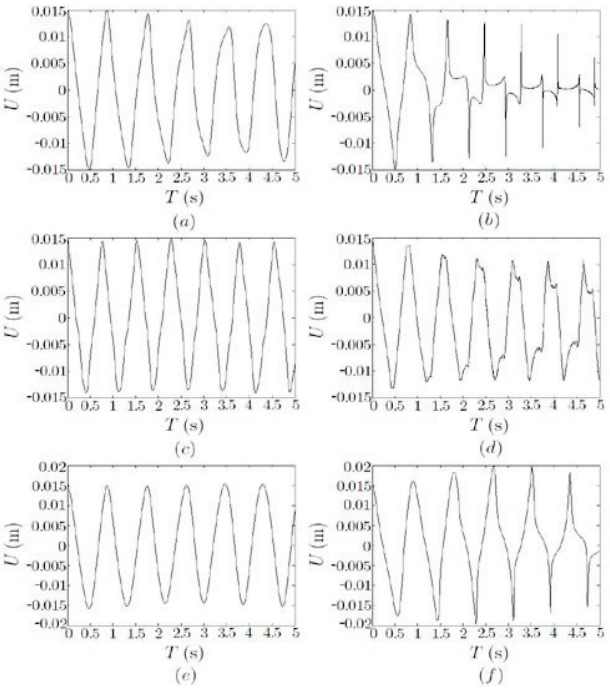

Fig. 4 Transverse displacement of the translating string at the middle point calculated using Galerkin's method from (a,b) the original linear model, (c,d) the nonlinear model, and (e,f) the intermediate linear model for the translation velocity corresponding to the (a,c,e) stable and (b,d,f) unstable solutions

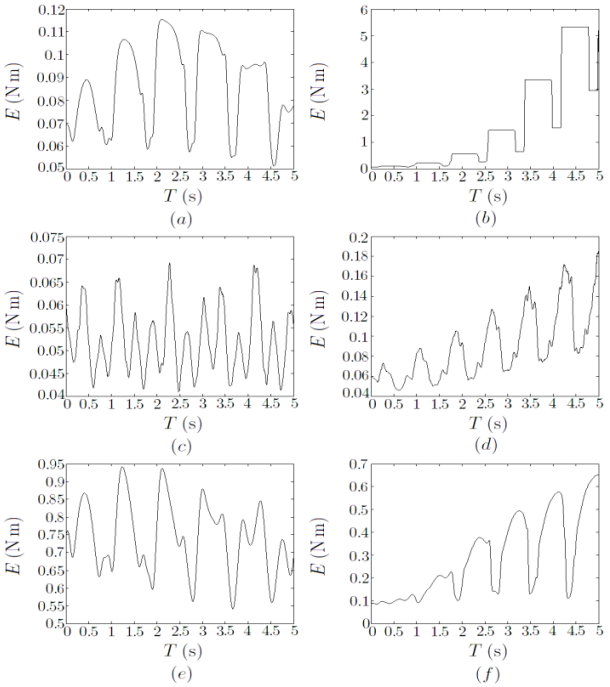

Fig. 5 Transverse vibratory energy of the translating string from (a,b) the original linear model, (c,d) the nonlinear model, and (e,f) the intermediate linear model for the translation velocity corresponding to the (a,c,e) stable and (b,d,f) unstable solutions

References

[1] WD Zhu, J Ni, Energetics and stability of translating media with an arbitrary varying length, *ASME J. Vib. Acoust.*, **122**, 295-304, 2000.

[2] WD Zhu, NA Zheng, Exact response of a translating string with arbitrary varying length under general excitation, *ASME J. Appl. Mech.*, **75**, 031003, 2008.

[3] WD Zhu, XK Song, NA Zheng, Dynamic stability of a translating string with a sinusoidally varying velocity, *ASME J. Appl. Mech.*, **78**, 061021, 2011.

[4] WD Zhu, K Wu, Dynamic stability of a class of second-order distributed structural systems with sinusoidally varying velocities, *ASME J. Appl. Mech.*, in press.